Extensions of Fundamental Flow Physics to Practical MAV Aerodynamics

(Elargissement de la physique fondamentale des écoulements à l'aérodynamique pratique des MAV)

AVT-202 Final Report.

STO TECHNICAL REPORT

TR-AVT-202

Extensions of Fundamental Flow Physics to Practical MAV Aerodynamics

(Elargissement de la physique fondamentale des écoulements à l'aérodynamique pratique des MAV)

AVT-202 Final Report.

The NATO Science and Technology Organization

Science & Technology (S&T) in the NATO context is defined as the selective and rigorous generation and application of state-of-the-art, validated knowledge for defence and security purposes. S&T activities embrace scientific research, technology development, transition, application and field-testing, experimentation and a range of related scientific activities that include systems engineering, operational research and analysis, synthesis, integration and validation of knowledge derived through the scientific method.

In NATO, S&T is addressed using different business models, namely a collaborative business model where NATO provides a forum where NATO Nations and partner Nations elect to use their national resources to define, conduct and promote cooperative research and information exchange, and secondly an in-house delivery business model where S&T activities are conducted in a NATO dedicated executive body, having its own personnel, capabilities and infrastructure.

The mission of the NATO Science & Technology Organization (STO) is to help position the Nations' and NATO's S&T investments as a strategic enabler of the knowledge and technology advantage for the defence and security posture of NATO Nations and partner Nations, by conducting and promoting S&T activities that augment and leverage the capabilities and programmes of the Alliance, of the NATO Nations and the partner Nations, in support of NATO's objectives, and contributing to NATO's ability to enable and influence security and defence related capability development and threat mitigation in NATO Nations and partner Nations, in accordance with NATO policies.

The total spectrum of this collaborative effort is addressed by six Technical Panels who manage a wide range of scientific research activities, a Group specialising in modelling and simulation, plus a Committee dedicated to supporting the information management needs of the organization.

- AVT   Applied Vehicle Technology Panel
- HFM   Human Factors and Medicine Panel
- IST   Information Systems Technology Panel
- NMSG   NATO Modelling and Simulation Group
- SAS   System Analysis and Studies Panel
- SCI   Systems Concepts and Integration Panel
- SET   Sensors and Electronics Technology Panel

These Panels and Group are the power-house of the collaborative model and are made up of national representatives as well as recognised world-class scientists, engineers and information specialists. In addition to providing critical technical oversight, they also provide a communication link to military users and other NATO bodies.

The scientific and technological work is carried out by Technical Teams, created under one or more of these eight bodies, for specific research activities which have a defined duration. These research activities can take a variety of forms, including Task Groups, Workshops, Symposia, Specialists' Meetings, Lecture Series and Technical Courses.

The content of this publication has been reproduced directly from material supplied by STO or the authors.

Table of Contents

List of Figures

AVT-202 Membership List

CO-CHAIRS

Dr. Michael OL
Air Force Research Lab, AFRL/VAAA
2130 8th Street, Building 45
Wright-Patterson AFB, OH 45433-7542
UNITED STATES
Email: michael.ol@us.af.mil

Prof. Holger BABINSKY
University of Cambridge, Engineering Department
Trumpington Street
Cambridge CB2 1PZ
UNITED KINGDOM
Email: hb@eng.cam.ac.uk

MEMBERS

AUSTRALIA

Mr. Jan DROBIK
DSTO
506 Lorimer Street
Fishermans Bend, Victoria 3207
Email: jan.drobik@dsto.defence.gov.au

Dr. Jennifer L. PALMER
DSTO, Air Vehicles Division, GPO Box 4331
Melbourne, Victoria 3001
Email: jennifer.palmer@dsto.defence.gov.au

CANADA

Dr. David RIVAL
Queen's University, McLaughlin Hall
130 Stuart Street
Kingston, Ontario K7L 3N6
Email: d.e.rival@queensu.ca

FRANCE

Dr. Jean-Bernard PAQUET
ONERA
5 Bd. Painlevé
59045 Lille Cedex
Email: jean-bernard.paquet@onera.fr

GERMANY

Dr.-Ing. Rainer HAIN
Universitaet der Bundeswehr Muenchen
Institute of Fluid Mechanics and
   Aerodynamics
Werner-Heisenberg-Weg 39
D-85577 Neubiberg
Email: rainer.hain@unibw.de

Dr. Ing. Robert KONRATH
DLR
Institute für Aerodynamk under
   Stroemungstechnik
Experimentelle Verfahren
Bunsenstrasse 10
D-37073 Goettingen
Email: robert.konrath@dlr.de

Prof. Dr.-Ing. Rolf Ernst RADESPIEL
Technische Universitaet Braunschweig
Institut für Strömungsmechanik
Technische Universität Braunschweig
Hermann-Blenk-Str. 37
D-38108 Braunschweig
Email: r.radespiel@tu-bs.de

ISRAEL

Prof. Gil IOSILEVSKII
Israel Institute of Technology
Aerospace Engineering
Technion City, Haifa 32000
Email: igil@aerodyne.technion.ac.il

TURKEY

M.Sc. Mustafa PERCIN
TU Delft
Delft University of Technology
Faculty of Aerospace Engineering
Aerodynamics Group, Building 64
Kluyverweg 2
2629 HT Delft
Email: m.percin@tudelft.nl

NETHERLANDS

Dr. Ir. Bas VAN OUDHEUSDEN
Delft University of Technology
Dept. of Aerospace Engineering
Kluyverweg 1
2629 HS Delft
Email: b.w.vanoudheusden@tudelft.nl

POLAND

PhD. Dr. Tomasz KOZLOWSKI
Wroclaw University of Technology
Wybrzeze Wyspianskiego 27
50-370 Wroclaw
Email: tomasz.kozlowski@pwr.wroc.pl

Prof. Hernyk KUDELA
Wroclaw University of Technology
Wybrzeze Wyspianskiego 27
50-370 Wroclaw
Email: henryk.kudela@pwr.wroc.pl

Prof. Krzysztof SIBILSKI
Air Force Institute of Technology
Ks Boleslawa 6, P.O. Box 96
01-494 Warsaw
Email: sibilski@hot.pl

TURKEY

Dr. N.L. Oksan CETINER-YILDIRIM
Istanbul Technical University
Faculty of Aeronautics and Astronautics
34469 Maslak, Istanbul
Email: cetiner@itu.edu.tr

Mr. Arif Cem GOZUKARA
Aselsan Inc. MGEO Division
Cankiri yolu 7. km Akyurt
06750 Ankara
Email: cgozukar@mgeo.aselsan.com.tr

Asst. Prof. Dr. Dilek Funda KURTULUS
Middle East Technical University
Aerospace Engineering Department
06531 Ankara
Email: dfunda@ae.metu.edu.tr

Prof. Mehmet SAHIN
Istanbul Technical University
Faculty of Aeronautics and Astronautics
34469 Maslak, Istanbul
Email: msahin@itu.edu.tr

UNITED KINGDOM

Prof. Kwing-So CHOI
University of Nottingham
Faculty of Engineering, University Park
Nottingham NG7 2RD
Email: kwing-so.choi@nottingham.ac.uk

UNITED STATES

Prof. Luis BERNAL
University of Michigan
1320 Beal Avenue
Ann Arbor, MI 48109-2140
Email: lpb@umich.edu

Dr. Kenneth GRANLUND
Universal Technologies Corporation
Air Force Research Lab.
Air Vehicles Directorate
2130 8th Street, Building 45
Wright-Patterson AFB, OH 45433-7542
Email: kenneth.granlund@wpafb.af.mil

Dr. Anya JONES
University of Maryland
Department of Aerospace Engineering
3154 Martin Hall
College Park, MD 20942
Email: arjones@umd.edu

Dr. Matthew MUNSON
US Army Research Laboratory
Autonomous Systems Division
RDRL-VTA (Building 1120B)
Aberdeen Proving Ground, MD 21005
Email: matthew.j.munson6.civ@mail.mil

Dr. Douglas SMITH
Air Force Office of Scientific Research
875 N. Randolph Street
Suite 325, Room 3122
Arlington, VA 22203
Email: douglas.smith.67@us.af.mil

Dr. Gregg ABATE
Air Force Office of Scientific Research (AFOSR)
European Office of Aerospace Research and
  Development (EOARD)
86 Blenheim Crescent
Ruislip HA4 7HB
UNITED KINGDOM
Email: gregg.abate@us.af.mil

CONTRIBUTORS

CANADA

Prof. Dominique POIREL
Royal Military College of Canada
Department of Mechanical Engineering
P.O. Box 17000, Stn Forces
Kingston, Ontario K7K 7B4
Email: poirel-d@rmc.ca

Dr.-Ing. Weixing YUAN
National Research Council of Canada
Institute for Aerospace Research (Uplands, U66)
Ottawa, Ontario K1A 0R6
Email: weixing.yuan@nrc-cnrc.gc.ca

FRANCE

Mr. Olivier MARQUET
ONERA, French Aerospace Laboratory
Chalais Meudon Center
Fundamental and Experimental Aerodynamic
  Department
8, rue des Vertugadins
92190 Meudon
Email: olivier.marquet@onera.fr

GERMANY

Prof. Dr. Andreas DILLMANN
German Aerospace Center
Institute of Aerodynamics and Flow Technology
D-37073 Göttingen
Email: Andreas.Dillmann@dlr.de

M.Sc. Hauke EHLERS
German Aerospace Center
Bunsenstraße 10
D-37073 Göttingen
Email: hauke.ehlers@dlr.de

Prof. Dr. Cameron TROPEA
Technische Universität Darmstadt
Fachgebiet Strömungslehre und Aerodynamik
Petersenstr. 30
D-64287 Darmstadt
Email: ctropea@sla.tu-darmstadt.de

Mr. Alexander WIDMANN
TU Darmstadt
Karolinenplatz 5
D-64289 Darmstadt
Email: awidmann@sla.tu-darmstadt.de

ISRAEL

Dr. Yossef ELIMELECH
Technion – Israel Institute of Technology
Haifa 32000
Email: meitalyossi.elimelech@gmail.com

ITALY

Dr. Flavio NOCA
Hepia – University of Applied Sciences
  Western
Rue de la Prairie 4
1202 – Geneva
SWITZERLAND
Email: flavio.noca@hesge.ch

TURKEY

Mr. Muhittin GOCER
TAI – Turkish Aerospace Industries Inc.
Fethiye Mah.Havacilik Blv.No. 17
06980 Kazan-Ankara
Email: mugocer@tai.com.tr

UNITED KINGDOM

Dr. Richard BOMPHREY
University of Oxford, Department of Zoology
South Parks Road
Oxford OX1 3PS
Email: richard.bomphrey@zoo.ox.ac.uk

Dr. Kevin KNOWLES
Cranfield University
DCMT
Shrivenham, Wiltshire SN6 8LA
Email: K.Knowles@cranfield.ac.uk

Dr. Nathaniel PHILLIPS
University of Oxford
Department of Zoology
The Tinbergen Building
South Parks Road
Oxford OX1 3PS
Email: nathan.phillips@zoo.ox.ac.uk

Mr. Charles PITT FORD
University of Cambridge
Trumpington Street
Cambridge CB2 1PZ
Email: cwp24@cam.ac.uk

UNITED KINGDOM (cont'd)

Mr. Patrick, Robert (Robbie), James STEVENS
University of Cambridge
Engineering Department
Trumpington Street
Cambridge CB2 1PZ
Email: prrjs2@cam.ac.uk

UNITED STATES

Prof. Carlos CESNIK
University of Michigan
Department of Aerospace Engineering
1320 Beal Avenue, 3024 FXB
Ann Arbor, MI 48109-2140
Email: cesnik@umich.edu

Prof. Jeff ELDREDGE
UCLA
48-121A Engineering IV
420 Westwood Plaza
Los Angeles, CA 90095-1597
Email: eldredge@seas.ucla.edu

Dr. Ray GORDNIER
Air Force Research Lab
AFRL/VAAC
Computational Sciences Branch
2210 8th Street, Building 146
Wright-Patterson AFB, OH 45433-7512
Email: raymond.gordnier@wpafb.af.mil

Mr. Adam HART
University of Florida REEF
1350 N. Poquito Road
Shalimar, FL 32579
Email: darock@ufl.edu

Mr. Field MANAR
University of Maryland
College Park, MD 20742
Email: fmanar@umd.edu

Mr. Peter MANCINI
University of Maryland
College Park, MD 20742
Email: petri1123@gmail.com

Mr. Ryan RANDALL
The University of Arizona
Aerospace and Mechanical Engineering
P.O. Box 210119
Tucson, AZ 85721-0119
Email: Ryan18rmr@yahoo.com

Dr. Matthew RINGUETTE
State University of New York at Buffalo
318 Jarvis Hall
Buffalo, NY 14260
Email: ringum@buffalo.edu

Prof. Sergey SHKARAYEV
University of Arizona
Aerospace and Mechanical Engineering
 Department
1130 N. Mountain Avenue
Tucson, AZ 85721-0119
Email: svs@Email.arizona.edu

Mr. Lawrence UKEILEY
University of Florida
REEF Dept. of Mechanical and
 Aerospace Eng.
1350 N. Poquito Road
Shalimar, FL 32579
Email: ukeiley@reef.ufl.edu

Dr. Miguel R. VISBAL
Air Force Research Lab.
Air Vehicles Directorate, AFRL/VAAC
2210 8th Street, Building 146B
Wright-Patterson AFB, OH 45433-7521
Email: miguel.visbal@wpafb.af.mil

AVT PANEL MENTOR

Dr. Siva S. BANDA
US Air Force Research Lab, AFRL/RQ
2130 8th Street
Wright-Patterson AFB, OH 45433
UNITED STATES
Email: siva.banda@us.af.mil

Extensions of Fundamental Flow Physics to Practical MAV Aerodynamics
(STO-TR-AVT-202)

Executive Summary

Low-speed high angle of attack flows result in flow separation, and all flow separation is inherently unsteady. If in addition the rigid body placed in the flow undergoes unsteady imposed kinematics – an acceleration from one relative free-stream velocity to another – the flow separation is mediated by the imposed motion, perhaps organizing into coherent structures of aerodynamic benefit. This is in contrast to steady flows, where separation is mainly seen as being detrimental to aerodynamic performance. In unsteady lift generation some of the structures formed by flow separation, such as the leading edge vortex, have the potential to increase lift well above the steady-state expectations. The present work explores imposed rotations and translations of rigid flat plates, comparing an angle of attack change (smoothed linear pitch ramp) with streamwise acceleration at constant incidence (again smoothed). We examine how motion-rate mediates the flow separation and formation of coherent flowfield structures, especially vortices forming and shed from the plate's leading edge and trailing edge. A rectilinear or translational motion, whether in pitch or surge, is compared to the rotational case, where the plate spins about an axis inboard of its inboard tip. Such rotational motion is notionally representative of a flapping-wing, and comparison between rotation and translation is aimed at elucidating whether rotation offers benefits in leading edge vortex stabilization and resulting aerodynamic performance.

Experiment, computation and analysis are compared, culminating in a proposed two-dimensional lumped vortex model proposed for approximate physics-based accounting for aerodynamic force history. Rotation was indeed found to stabilize the leading edge vortex, at least for inboard spanwise locations; the leading edge vortex sheds after saturation for the translational case. However, no advantage in peak lift coefficient or lift to drag ratio was found in rotation vs. translation. Pitching causes a large force transient, both in rotation and translation, relative to surging. Non-circulatory or apparent-mass effects were found to be well-modeled by arguments from classical unsteady potential flow. For translation, a long time interval (at least $10 – 15$ convective times) is needed for the post-maneuver lift transient to asymptote to the bluff-body reference value. The rotational case reaches a steady lift value sooner (~ 5 convective times) and this steady value is higher than for translation. Thus rotation does offer a lasting advantage in lift (or more properly, normal-force, since leading edge suction is always lost for thin flat plates with separated flow) relative to translation, and this is the benefit of a stable leading edge vortex. We reiterate that no such benefit is evinced during motion transients, whether in surge or pitch.

Elargissement de la physique fondamentale des écoulements à l'aérodynamique pratique des MAV
(STO-TR-AVT-202)

Synthèse

La faible vitesse et l'angle d'incidence élevé provoquent une séparation de l'écoulement, laquelle est intrinsèquement instable, comme toutes les séparations d'écoulement. Si, de surcroît, le corps rigide placé dans l'écoulement subit une cinématique imposée instable – une accélération de la vitesse relative d'écoulement libre – la séparation de l'écoulement est influencée par le mouvement imposé et peut s'organiser en structures cohérentes qui présentent un avantage aérodynamique. Cela s'oppose aux écoulements stables, dans lesquels la séparation est principalement considérée comme nuisible aux performances aérodynamiques. En cas de génération instable de la portance, certaines structures formées par la séparation de l'écoulement, telles que le vortex du bord d'attaque, peuvent augmenter la portance bien au-delà des espérances à l'état stable. Le présent document étudie les rotations et translations imposées de plaques planes rigides, en comparant une modification de l'angle d'incidence (courbe de tangage linéaire lissée) avec une accélération dans le sens de l'écoulement à incidence constante (également lissée). Nous examinons de quelle façon la vitesse du mouvement influence la séparation de l'écoulement et la formation de structures cohérentes de champ d'écoulement, en particulier les vortex qui se forment et sont chassés du bord d'attaque et du bord de fuite de la plaque. Un mouvement rectiligne ou translationnel, en tangage ou en décrochage, est comparé au cas de la rotation, dans lequel la plaque tourne autour d'un axe placé à l'intérieur de son extrémité intérieure. Ce type de mouvement rotationnel est théoriquement représentatif d'une aile battante et la comparaison entre la rotation et la translation vise à déterminer si la rotation offre des avantages pour la stabilisation du vortex du bord d'attaque et la performance aérodynamique qui en découle.

L'expérimentation, le calcul et l'analyse sont comparés, principalement dans un modèle bidimensionnel à vortex localisé, pour un compte rendu approximatif basé sur la physique, en vue de l'historique de la force aérodynamique. En effet, il a été démontré que la rotation stabilise le vortex du bord d'attaque, tout au moins celui placé à l'intérieur dans le sens de l'envergure ; le vortex du bord d'attaque disparaît après saturation dans le cas de la translation. Cependant, par rapport à la translation, la rotation ne présente manifestement aucun avantage pour le coefficient de portance ou la finesse. Le tangage provoque un phénomène transitoire de force élevée, à la fois en rotation et en translation, par rapport au décrochage. Les effets non circulatoires ou liés à la masse apparente se sont avérés bien modélisés par les arguments issus de l'écoulement potentiel instable classique. Concernant la translation, un long intervalle de temps (au moins 10 – 15 temps de convection) est nécessaire pour que la portance transitoire après manœuvre rejoigne l'asymptote de la valeur de référence du corps non profilé. Le cas de rotation atteint une valeur stable de portance plus rapidement (environ 5 temps de convection) et cette valeur stable est supérieure à celle de la translation. Par conséquent, la rotation présente un avantage durable par rapport à la translation du point de vue de la portance (ou, plus exactement, de la force normale, puisque l'aspiration du bord d'attaque est toujours perdue dans le cas des plaques planes de faible épaisseur avec un écoulement séparé) et cela est dû à la stabilité du vortex sur le bord d'attaque. Nous répétons qu'aucun avantage de ce genre ne se manifeste pendant les mouvements transitoires, que ce soit en tangage ou en décrochage.

Small slow-flying objects are likely to be subjected to combination of severe unsteadiness and flow separation. The flight vehicle is likely to find itself at high angle of attack, or to rapidly change angle of attack, or to be influenced by winds, such that angles of attack would be large, and quickly varying. High frequencies and maneuver-amplitudes do not occur for lumbering transport aircraft or even for missiles or maneuvering fighters, where the reduced-frequencies are low because the flight speed is high and convective time (ratio of wing mean aerodynamic chord to flight speed) is fast. The so-called "Micro Air Vehicles", or MAVs, spawned interest in basic questions of unsteadiness and massive separation at high frequency, and for these problems low Reynolds number is concomitant, simply from the scales of fluid density, kinematic viscosity, frequency and amplitude of motion.

We focus on what happens when an abstracted body – a rigid flat plate – accelerates with respect to a fluid. We do not address specific applications or the design of MAVs, or motivating flight modalities in nature. These are extensive and deeply interesting topics, where unsteady aerodynamics is of great relevance. Indeed, the problem of how flapping-wing insects generate high stroke-averaged lift coefficients (see for example [1]) has been the motivation for prior STO AVT Task Groups, such as AVT-149 [2], and continues to inform the question of how lift is connected with wing geometry, flapping kinematics, Reynolds number and so forth. Operation at small Reynolds number seems to necessitate unsteady lift mechanisms to produce acceptably high lift coefficients; see for example the taxonomy in Figure 1-1. However, the present objective is to elucidate a small but expository set of abstract problems, and to connect flowfield phenomena to aerodynamic force history, and perhaps thenceforth to build a reduced-order model that might ultimately be useful for engineers. For problems that are highly unsteady, to what extent does the resulting aerodynamic response significantly differ from the nominal steady values? The present work is concerned with unsteady aerodynamics, where flow separation is massive, and there is non-trivial coupling between flow separation from bluff-body effects (alternatively from deep stall of streamlined shapes) and from the imposed motion. The problem is taken as being identically incompressible, even though applications of dynamic stall such as helicopter rotors are of course strongly influenced by compressibility [12].
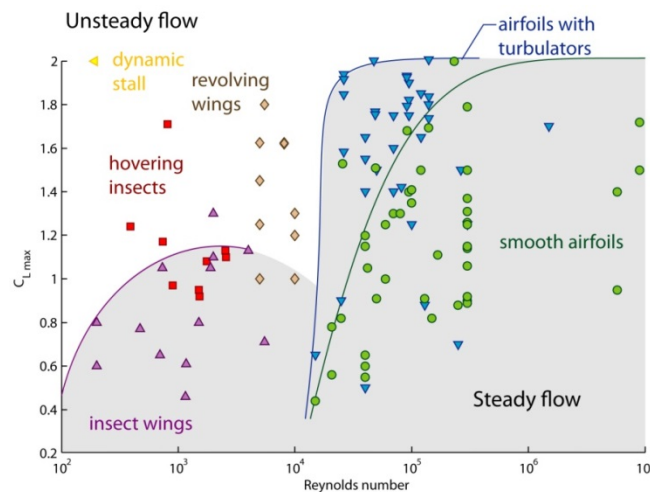
Figure 1-1: Notional Scatter-Plot of Maximum Lift Coefficient vs. Reynolds Number for a Range of Operating Conditions, Citing in Particular the Utility of Unsteady Mechanisms for High-Lift Production at Very Low Re, where Purely Steady Means Result in Unacceptable Paucity of Lift. After Jones [28].

The limit of high frequency and low amplitude has been rationalized over 70 years ago, mainly in the context of aeroelasticity, using potential-flow assumptions [3]. The outcome was Theodorsen's celebrated formula and its various extensions and reformulations. Though such formulas were shown to be valid predictors of lift-history even for some aggressive motions where the underlying assumptions of attached-flow and planar-wake are falsified [4], such pleasant conclusion is not universal [5], especially for large-amplitude motions. We therefore need to understand the impact of flow separation, or more properly, of vortices shed from the plate's leading and trailing edges, and how these cause departure from the predictions of attached-flow theory. This, in essence, is the focus of our Task Group.

Unsteady problems begin with a definition of kinematics. Next, we cover facilities and methods, give a resume of computations and measurements, and finally present an analytical/phenomenological conjecture and its corroboration by the data.

1.1 RESUME OF KINEMATICS

In 2D, a flat plate can pitch about some pivot point, plunge (move normal to the relative free-stream direction) and surge (move parallel to the free-stream direction). Thus there are three degrees of freedom, plus the various kinematic conditions: pitch pivot point, initial incidence, final incidence, reduced frequency, plunge amplitude, and surge amplitude. "Normal hover" [6] is a form of combined pitch/plunge, where the absence of a free-stream confounds the usual definitions of reduced frequency and Reynolds number. Another special case is pure surge in a fluid quiescent in the lab frame, where the plate begins at rest and accelerates through some motion-profile, typically at some fixed incidence angle, reaching a steady free-stream.

3D introduces a bewildering plethora of additional kinematic possibilities. Now the wing has finite span, with inboard and outboard wingtips. Most important is rotation about some fixed point near the inboard tip, typically located some chord-fraction outside the wing. Roll of the wing (in some conventions called "flapping") is not considered here, as we regard it as derivative of 2D plunge. Yaw is a form of rotation, and spanwise translation is irrelevant.

In 3D the wing is always finite-span, and four kinds of motion are possible:
- Rectilinear translation in surge;
- Rectilinear pitch, meaning a pitch about a spanwise-aligned axis, in steady free-stream;
- Rotational surge about a fixed point near the inboard wingtip, with constant incidence angle of the plate; and
- Combination of rotation with pitch, where the rotation is a fixed speed but the incidence angle is ramped up.

The key comparisons are rotation vs. translation, and surge vs. pitch. Mediating the four principal kinds of motion are Reynolds number, reduced frequency and aspect ratio of the plate. A schematic rendition of the four principal cases and associated secondary considerations is given in Figure 1-2. Reduced frequency for transient motions is:

$$K = \frac{\dot{\theta} c}{2 U_\infty}$$

(Eq. 1-1)

where "f" is the frequency, "c" the chord of the plate, and the denominator is twice the relative-free-stream steady speed. "K" is therefore just a convective normalization of the dimensional pitch rate.
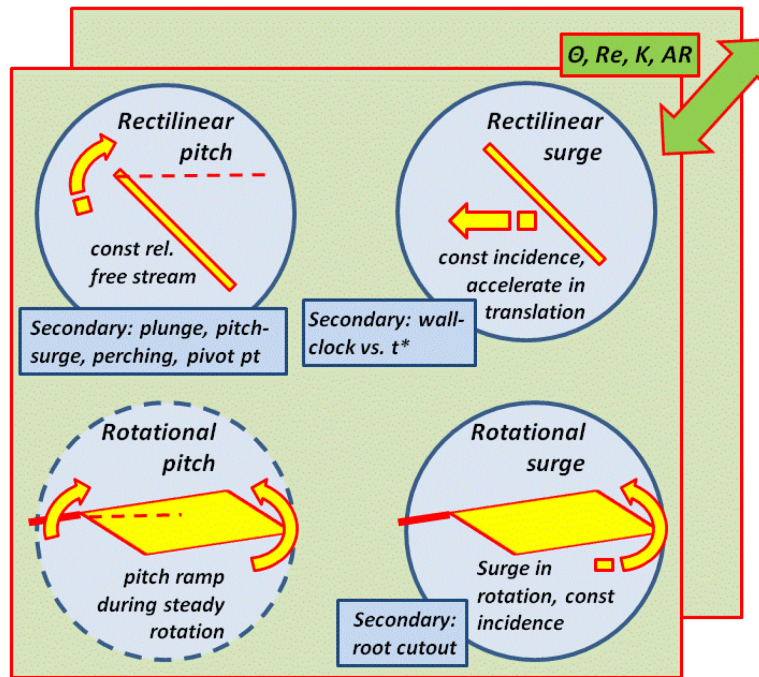
Figure 1-2: Schematic of the Four Prime Test Conditions. Reynolds number, peak incidence angle, reduced frequency, pitch pivot-point, plate aspect ratio and leading edge shape, and rotating-plate root cut-out are additional parameters pursued by some groups. For all four kinds of motion, the "fast case" has the acceleration occurring over one chord (surge from rest to steady towing-speed over one chord, pitch from zero incidence to 45-degrees over one convective-time in a steady free stream), and the "slow case" occurs over 6 chords. Thus there are 8 total principal cases.

Details of kinematics – velocity profiles and time-base – are given in Figure 1-3. Note that for problems without a lab-frame steady free stream, where the test article starts from rest, there are two alternatives to defining the running time-base, either the wall-clock (seconds), or a 'convective time' where the distance travelled by the leading edge of the wing is made dimensionless by chord-length. These are unimportant and almost fungible for the long-term history, but can be important for force transients at high-rate and early time. The incidence-angle history in Figure 1-3 is a linear ramp with smoothed "corners". Smoothing is via a C^∞ rational-function, $\hat{G}(t/T)$, proposed by Eldredge $et\ al.$ [7]:

$$G(t/T) = \ln[(\cosh(A)\cosh(D))/\cosh(B)\cosh(C)],$$

$$A = 2a\left(\frac{2\pi t}{T} + \frac{2-\pi}{2}\right),$$

$$B = 2a\left(\frac{2\pi t}{T} - \frac{2+\pi}{2}\right),\quad\quad\quad\text{(Eq. 1-2)}$$

$$C = 2a\left(\frac{2\pi t}{T} + \frac{2-3\pi}{2}\right),$$

$$D = 2a\left(\frac{2\pi t}{T} - \frac{2+3\pi}{2}\right),$$

$$\hat{G}(t/T) = h_0(1 - 2G(t/T)/max(G))\ .$$
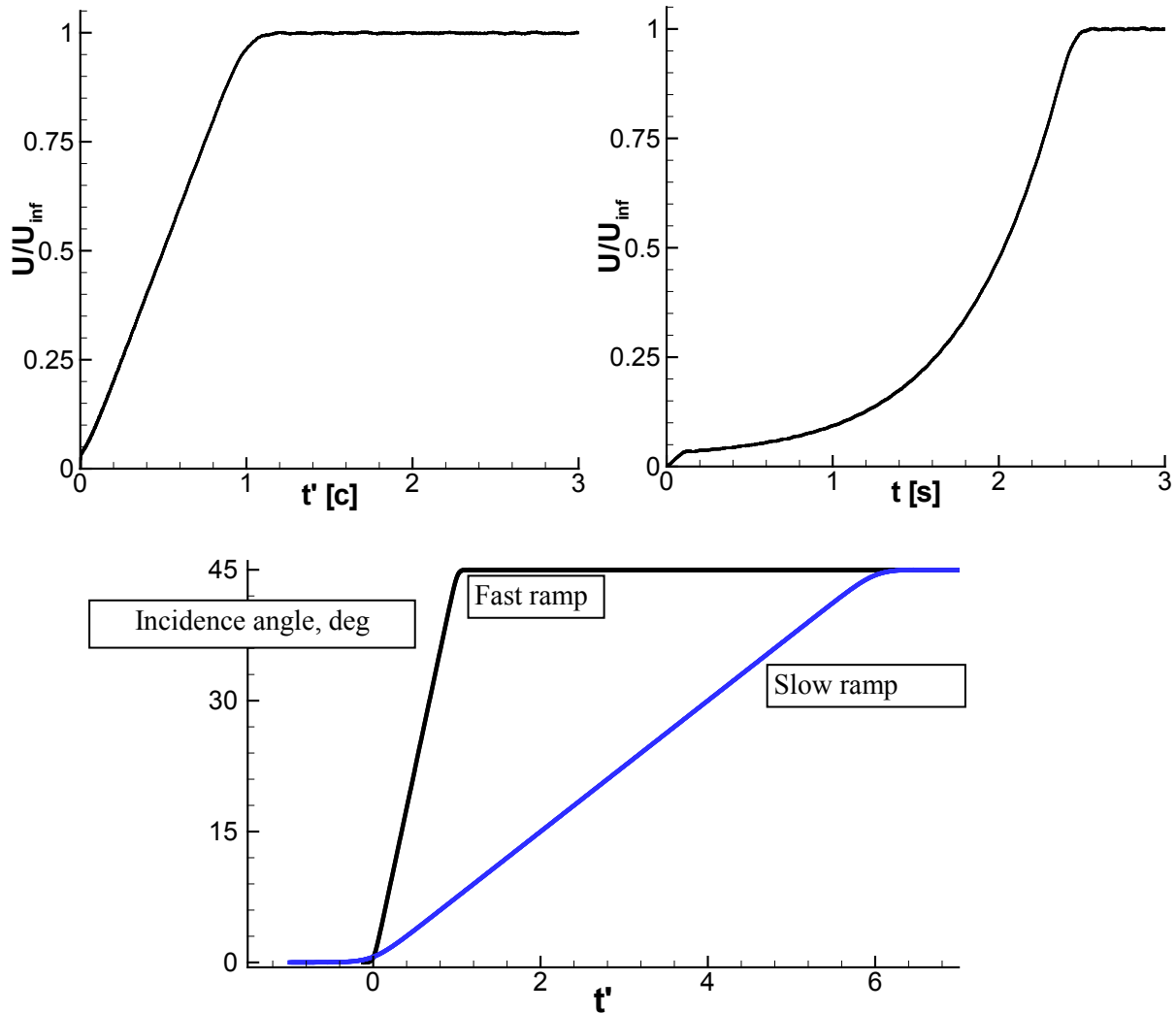
Figure 1-3: Typical Velocity Histories. Top row: Smoothed ramp in surging velocity, passing from initial condition (at rest) to final condition (normalized value of 1); ramp in velocity linear with convective time (left) looks like an exponential when plotted vs. wall-clock time in seconds (right). The distinction between the two causes a difference in force history during the acceleration, which enervates almost immediately upon cessation of acceleration. Bottom row: "Slow" ramp (blue, 6 convective times, or K = π/48) and "fast" ramp (black, 1 convective time, or K = π/8) in pitch, starting from θ = 0° and concluding with θ = 45°. In pitch, there is a constant free-stream, so linear ramps with respect to wall-clock or convective time are equivalent.

The function $G(t/T)$ has four non-dimensional-time parameters (A, B, C and D in Eq. 2), one each at the "corner" of the trapezoidal motion profile. The parameter "a", which controls the amount of smoothing, is a dimensionless acceleration upper bound, typically limited by mechanical acceleration of a laboratory apparatus. The $\hat{G}(t/T)$ function can be applied to transient or periodic motions, the latter looking like a smoothed sawtooth train.

AVT-202 cases are primarily of aspect ratio AR = 2 (rotational motions) and AR = 4 (rectilinear motions), the reasoning being that in rotation there is one "blade" of two, each blade of AR = 2.

Much today is made of PIV post-processing to assess vortex strength and to calculated integrated aerodynamic loads from the flowfield [8]. Our approach does not pursue whole-field velocity/vorticity integration for arriving at aerodynamic force history, but instead to advocate for a phenomenological model, tracking a small number (ideally, just two) discrete vortices. An important recent advance was the vortex-recognition method of Graftieaux [9], enabling:

1) Assessing for whether a given flowfield structure is a credible vortex; and

2) How to define its boundary to calculate circulation by integrating vorticity within this boundary.

We follow this approach to extract LEV and TEV circulation strength evolution, and vortex-core trajectory as a function of plate displacement.

The motions in Figure 1-2 and Figure 1-3 are all transient: they begin from some initial condition, either with no relative motion between the body and the ambient fluid, or with the body in a zero-lift condition (zero incidence for an uncambered plate) in a steady flow. They pass through a transient and arrive again at the same nominal steady-state condition, where relative acceleration between body and fluid ceases, though bluff-body shedding can result in a perpetually unsteady flow. The complementary case, not examined in AVT-202, is that of periodic motion, where the body executes some trajectory that repeats itself with a characteristic frequency. We consider transient motions, as opposed to periodic motions, because lags/transients are obvious in the remaining aerodynamic response after the motion has ceased, and are not inherited in the following period, as they would be in periodic motions. There is explicitly a phase of motion where acceleration is non-zero, followed by a long (ideally infinite) run where the relative free-stream is steady. For the rotating plates, after completing a full revolution the plate enters its own wake, and in that narrow sense the resulting flow remains unsteady. The end-state of all motions is deep-stall, typically at 45 degrees incidence.

1.2 PRINCIPAL SCIENTIFIC QUESTIONS OF THIS STUDY

Our interest includes the following questions:

1) Why do so many disparate geometries, motions and resulting flowfields evince similar aerodynamic force histories? Is there a unifying principle, and perhaps a low-order modeling scheme, accounting for this?

2) What is the budget of circulatory and non-circulatory load-contributions while the plate is accelerating? Can these respective contributions be linearly superimposed, to form the total aerodynamic force history? How much of the lift budget is carried by the LEV, TEV, bound circulation (including pitch-rate effects)?

3) What are the long-term transients (residual unsteadiness in the aerodynamic response and the flowfield) after the motion has completed? That is, to what extent does the accelerating portion of the motion affect vortex history (and loads history)?

4) What are criteria for vortex initiation, saturation, and detachment? Are there multiple vortices at the LE after the initial LEV? Are there multiple vortices at the TE after the starting-vortex has been ejected?

5) How does aerodynamic force production scale with pitch rate, pitch pivot point location and peak incidence angle? Is there a fundamental difference in lift-production between rotation and translation, between pitch and surge?

6) Are 3D structures important in the vortex topology? Do finite-aspect-ratio wings evince fundamentally different integrated aerodynamic load histories than those in 2D? How do tip vortices mediate LEV/

TEV production and bound circulation? More broadly, what sort of spanwise variations are there for low and moderate aspect ratio wings?

7) How does Reynolds number mediate vortex production/evolution, and aerodynamic force history?

1.3 BRIEF REVIEW OF CLASSICAL ANALYTICAL MODELS

Wagner [53] was one of the earliest researchers to study the lift generated by an airfoil starting from rest at a small fixed angle of attack, in this case for impulsive start, where the acceleration in surge is infinitely large, occurring over infinitesimal time. Clearly the application of Wagner's model to AVT-202 cases (all of which have finite acceleration over finite time) requires some discretion. Based on the physical assumption that the velocity at the trailing edge is always finite and by modeling the wake as a flat vortex sheet, Wagner was able to determine the lift as a function of chords travelled. At any point, Wagner assumed that the circulatory lift was produced by a bound circulation in accordance with thin airfoil theory that is in the absence of separation. Non-circulatory lift is just a delta function. Wagner's analysis shows that the effective angle of attack is reduced due to the downwash from the shed vortices in the wake. This in turn delays the build-up of the bound circulation, which leads to further shedding of vortices in the wake and as a result there is a considerable delay in the development of the ultimate steady-state lift. Figure 1-4 (from Wagner [53]) compares the growth of lift with the growth of circulation. Half of the final lift is assumed at once, and the lift then gradually approaches its steady asymptote. The circulation, however, rises steadily from zero.
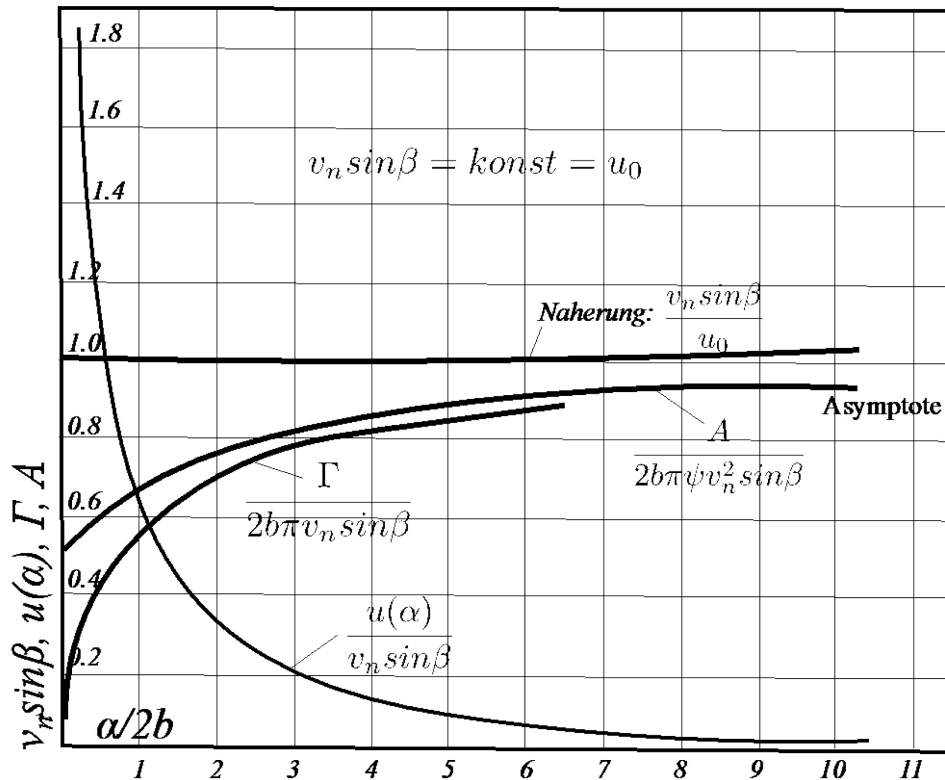
Figure 1-4: Wagner's Lift Prediction (marked 'A', starting at 0.5) and Rendition of Wagner's Bound Circulation Γ Starting from Zero. Note that the "Wagner function" is typically taken to begin from 0.5. [53].

1.4 REDUCED-ORDER MODEL OF VORTEX PHYSICS

One of the chief aims of this Report is to propose and to experimentally corroborate a simple semi-analytical scheme to predict the unsteady lift generated by a flat plate in an unsteady flow in two dimensions. All of the "canonical" cases in this Report are plates of finite aspect ratio, whence a 2D model cannot be physically accurate, especially considering the role of tip vortices for translational cases and radial-effects in LEV stabilization for the rotational cases. Nevertheless, a 2D simplification, for example in a strip-theory sense, is eminently attractive. Accordingly, here we consider a flat plate accelerating from rest at a constant angle of attack, and a flat plate pitching in a steady free-stream. The treatment is inviscid and incompressible.

1.4.1 Non-Circulatory and Circulatory Force Contributions

We postulate that the unsteady force exerted by an object onto the surrounding fluid (and thus the opposite reaction force experienced by the object) is equal to the rate of change of momentum in the surrounding fluid. To quantify this force it is necessary to integrate the momentum across the whole flowfield (stretching to infinity) and then take the time derivative[1]:

$$F = \frac{d}{dt} \iint\limits_{-\infty}^{\infty} \rho\, \boldsymbol{u}(\boldsymbol{x}, t)\, dA$$

where $\boldsymbol{u}$ is the unsteady velocity field, $\boldsymbol{x}$ is the location vector, t is time and A is an area element (*dxdy*). Thus, if it were possible to accurately determine the velocity field everywhere at several instances in time, one could determine the force experienced by an object – e.g., lift and drag. In reality however, there are practical difficulties making this untenable.

An important simplification is possible for situations where the unsteady flow around an object is self-similar. By this we mean a flowfield topology (streamline pattern) that is independent of time, although the magnitude of local velocity may scale with a time-varying free-stream $U_\infty(t)$:

$$\boldsymbol{u}(\boldsymbol{x}, t) = \boldsymbol{U}_\infty(t)\, k(\boldsymbol{x})$$

Here *k(x)* is some function relating the local velocity to the (variable) free stream. Note that *k* is constant in time. Thus, the force experienced by the object can be expressed as:

$$\boldsymbol{F} = \rho \underbrace{\iint\limits_{-\infty}^{\infty} k(\boldsymbol{x}) dA}_{I}\; \underbrace{\frac{dU_\infty(t)}{dt}}_{II}$$

The force is therefore the product of a time-invariant area integral of *k(x)* (Term I) and the acceleration of the free-stream (Term II). Note that the first term (I) has the unit of mass, and is constant throughout the motion. The force is proportional to the acceleration, and hence the term 'virtual mass' or 'added mass'[2].

---

[1] Here, it is implied that the pressure is uniform at the integration boundary (∞). Vector quantities are in bold.

[2] Though other treatments are possible, one could go further and declare any attempt to make the calculation of virtual mass force "more accurate" futile because such an approach tries to more closely approximate the real momentum change of the surrounding fluid. Taken to the extreme, this "virtual mass force" would eventually be equivalent to the total force experienced by the flow (first equation).

An expository case for considering this force contribution is the classical potential flow around an accelerating flat plate at 90° angle of attack (Figure 1-5).
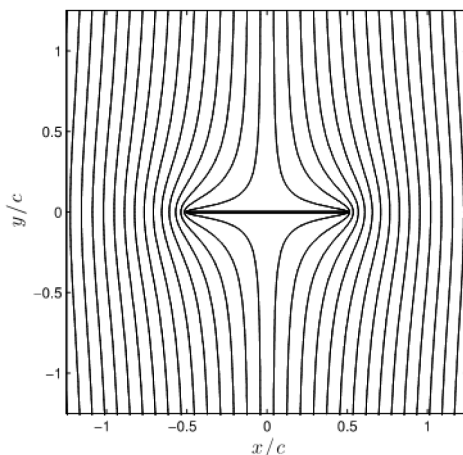
Figure 1-5: Potential Flow Around a Flat Plate at 90° Angle of Attack.

In steady potential flow, the plate experiences identically zero force. However, in unsteady flow the surface pressures on the windward side are increased, while the pressures on the leeward side are decreased (e.g., unsteady Bernoulli equation), giving a net force:

$$F = \frac{\rho c^2 \pi}{4} \dot{V}$$

where c is the chord of the plate and V the plate-normal velocity of the fluid. This force is exactly equivalent to the inertia of a circular cylinder of fluid with diameter c undergoing the same motion as the plate. For a plate accelerating at an angle of attack, only the velocity component normal to the plate contributes to this force (by the principle of superposition and assuming the flow to remain inviscid, i.e., attached).

Realistic flows are not self-similar, and viscous forces are not negligible. We thus postulate that the total unsteady force is the sum of the added mass force and a second circulatory force contribution [3]. We shall persist with the contrivance of inviscid flow to determine the added-mass term by considering the plate-normal velocity at mid-chord and equating the force to the added mass force experienced in potential flow of a flat plate at 90° angle of attack.

We next turn to the circulatory contribution. The simplest model for a circulatory force is to consider the relationship between forces and vortices. The flow shown in Figure 1-6 has a net momentum, thus the generation of a pair of vortices (of equal but opposite strengths) in a quiescent fluid requires a force (by force-momentum equation). According to Lamb [10], the magnitude of this momentum is:

$$J = \rho d \Gamma$$

---

[3] Early on in the motion the flow is quite close to the potential flow model and thus the initial force should be reasonably close to the prediction. A much more rigorous treatment actually shows that even in a complex viscous unsteady flow the added mass term remains that seen for the potential flow around the same object, and the total force is indeed the sum of this force and all circulatory (viscous) components.

where J is the impulse (momentum), d the distance between the vortex centroids, and Γ the vortex circulation. Since force equals the rate of change of momentum, the chain rule of differentiation gives:

$$F = \rho(\dot{d}\Gamma + d\dot{\Gamma})$$

(where *dot* signifies time derivatives). This shows that vortex lift has two contributions, one related to strength of vortices and the growth in distance between them (and this term leads to $L = \rho U\Gamma$ in steady flow), and another related to the growth of circulation. The direction of the force is normal to the line connecting the two vortices.
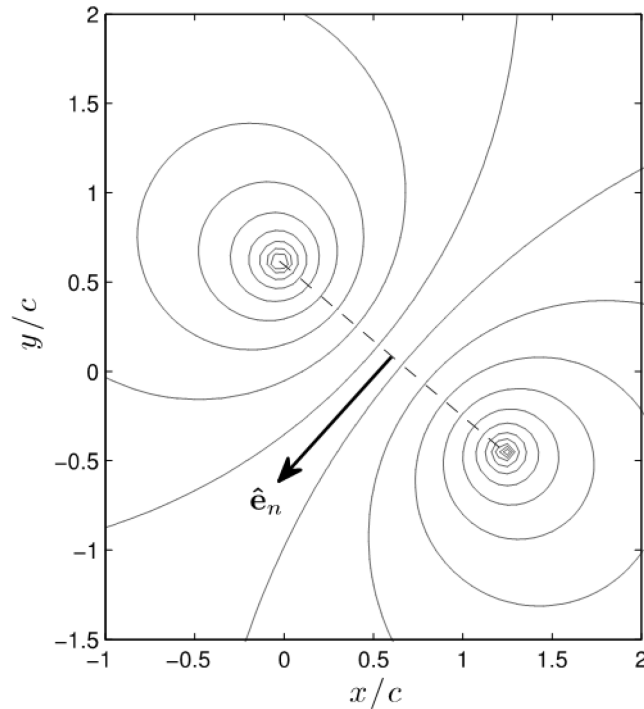
Figure 1-6: Potential Flow Streamlines Around a Stationary Counter-Rotating Vortex Pair. This flow has net momentum produced by the vortex pair, and therefore results in a net force.

Let us consider a flat plate in unsteady flow as being the source of such a force through the generation of a starting vortex (or TEV), and either bound circulation or a LEV associable with the plate. Setting x as the streamwise co-ordinate, lift is the y-component of this force. Knowledge of the strengths and positions of the two vortices (LEV and TEV) allows us to compute this circulatory lift force and to express it in coefficient form (where u_i are the x-components of vortex velocities, and x_i are the x-components of vortex locations):

$$C_{l,circ} = -\frac{2}{U_\infty^2 c}\left[(u_{LEV} - u_{TEV})\Gamma_{LEV} + (x_{LEV} - x_{TEV})\dot{\Gamma}_{LEV}\right]$$

Note that this is non-dimensionalised by a free stream velocity U_∞. Apart from the choice of U_∞ and the direction of the lift force, this result is independent of the coordinate system.

In situations where there is both bound circulation and a LEV, it is suggested that we 'lump together' both vortices by calculating the total circulation and a centroid location (like a centre of gravity). Note that the

position of the centroid can move relative to the plate if the LEV convects with respect to the plate. Thus there are only two vortices in the flow, and these must be of equal and opposite strength according to Kelvin's theorem. In reality, as the LEV changes strength, a vortex sheet is shed from the TE, which may not always merge with the TEV (and even if it does this will take time) and thus the above flow is a relatively crude approximation. However, if we assume (reasonably) that the vortex sheet moves away at U_∞ the first term of the above equation remains correct. Furthermore, it can be argued that because any changes in circulation cause shedding at the trailing edge, an approximation for the distance term in the above equation might be the chord length. Thus we propose to alter the above to:

$$C_{l,circ} = -\frac{2}{U_\infty^2 c}\left[(u_{LEV} - u_{TEV})\Gamma_{LEV} + c\dot{\Gamma}_{LEV}\right]$$

This effectively assumes that the distance between two opposing vortices arising from a change in circulation is equal to the chord length.

Although crude, this model is helpful in understanding the magnitude of circulatory lift generated in an unsteady wing flow, by tracking the LEV and TEV (Figure 1-7). The model illustrates nicely when a *detached* LEV contributes to wing lift:

1) While it continues to strengthen, regardless of its position; and

2) While it moves relative to the TEV.
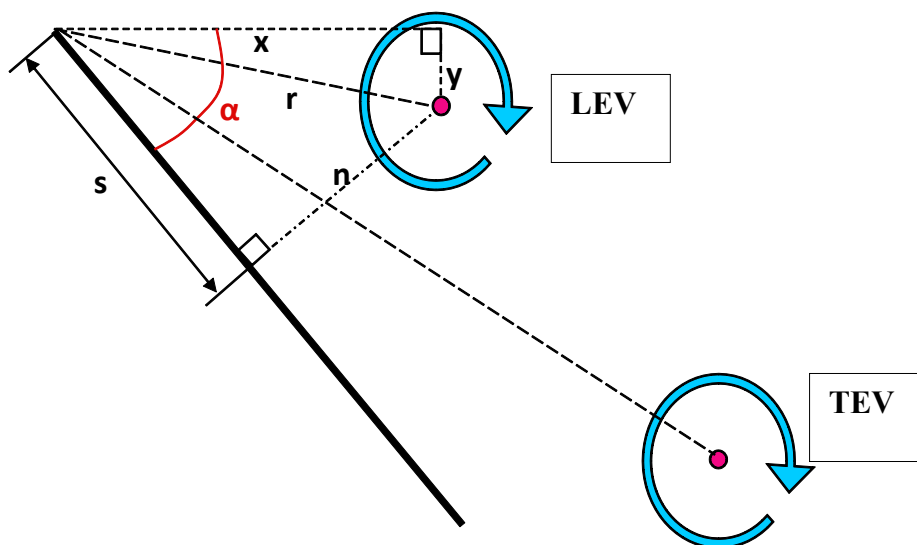
Figure 1-7: Schematic of Leading Edge Vortex (LEV) and Trailing Edge Vortex (TEV) with Respect to the Plate, with Coordinate System with Origin at the Plate's Leading Edge.

Thus, it is not necessary for the LEV to be at a constant position relative to the wing ('*attached*'). As long as it moves away at a slower speed than the TEV (relative to the wing) it contributes to the circulatory force. However, after the LEV is 'shed' it generally stops growing in strength and moves away from the wing at an ever increasing rate, thus reducing its force contribution until it ultimately drifts at free stream velocity, at which point no further force is produced.

With this approach in mind, we proceed to deriving circulatory and non-circulatory lift terms for the surging plate and the pitching plate. As cautionary note, there is no reason why the real viscous flow should be equivalent to the superposition of an accelerating normal flow, a 2-vortex flow and a remaining uniform flow in the direction of the plate. One might compare some PIV flowfields with a flow calculated form this analytical model. In any case, PIV data is necessary to obtain LEV and TEV trajectory history and circulation history.

1.4.2 Analytical Derivations for the Surging Plate

We express the plate-normal velocity as:

$$V = U \sin \alpha$$

The added mass force is:

$$F = \frac{\rho c^2 \pi}{4} \dot{U} \sin \alpha$$

Calculating the component in lift direction:

$$L = F \cos \alpha = \frac{\rho c^2 \pi}{4} \dot{U} \sin \alpha \, \cos \alpha$$

expressed in coefficients this gives:

$$C_{L,non-circ} = \frac{\pi c \, \dot{U}}{4U^2} \sin 2\alpha$$

No force is generated at vanishing angle of attack. The above result shows that the non-circulatory force is perpendicular to the plate. It is generally more common to normalize the force coefficients in the surging case with the eventual free-stream velocity U_∞. This reduces the lift coefficient during the acceleration phase by $\frac{U(t)}{U_\infty}$.

For the circulatory term, we make use of Pitt-Ford's observation [11] that the bound circulation in surging flat plates tends to vanish early on in the motion. Thus we assume that all circulation in the flow is concentrated in two vortices: an LEV (that need not be attached to the plate) and a TEV. The vorticity shed by changing strength of the LEV is assumed to immediately merge with the TEV. In lieu of PIV data on vortex trajectories and circulations, one could conjecture that Γ_{LEV} grows according to the Wagner function to eventually reach some saturated steady-state value (Figure 1-4). This is not far from the real scenario. We use the Wagner function (starting from zero) rather than the Wagner prediction for lift (which starts at a finite lift coefficient half of the ultimate value) because Wagner assumes that the growth of bound circulation starts from zero. There is no real physical justification of this; it is merely convenient to use this curve because it fits the observed growth of circulation reasonably well as will be shown later in this Report.

Agreement can probably be improved. In the above, the Wagner function was calculated by assuming a constant asymptotic Γ_∞ based on the terminal velocity. If we locally adjust the curve by scaling with $U(t)/U_\infty$ during the acceleration phase, then its shape should fit better with the measured data. The exact Wagner function is iterative, but a close explicit formula is:

$$\frac{\Gamma(t)}{\Gamma_\infty} = 0.914 - 0.3151 \exp\left(\frac{-\frac{s}{c}}{0.1824}\right) - 0.5986 \exp\left(\frac{-\frac{s}{c}}{2.0282}\right)$$

Generally, the steady-state circulation of an LEV is unknown, so we use the equivalent to $2\pi\alpha$. This does not mean that the plate at any point achieves the equivalent value of steady-state lift, because we do not assume that the LEV is perfectly attached to the plate.

We also need an estimate of the LEV motion relative to the plate (or the TEV). As shall be shown in later sections, we can estimate the relative drift velocity between the LEV and the TEV to be between 0.3 and 0.5 of the free stream velocity during the early part of the motion (Figure 1-8). This appears to hold even beyond the acceleration phase, although this cannot be correct indefinitely as the relative velocity eventually has to vanish. To be precise, there appears to be an early stage where the LEV is 'attached', i.e., moving more slowly relative to the wing, but we propose to ignore this because the vortex strength at this stage is still small. Thus the simple $\frac{1}{3}U_\infty$ rule might actually work reasonably well to capture the circulatory force.
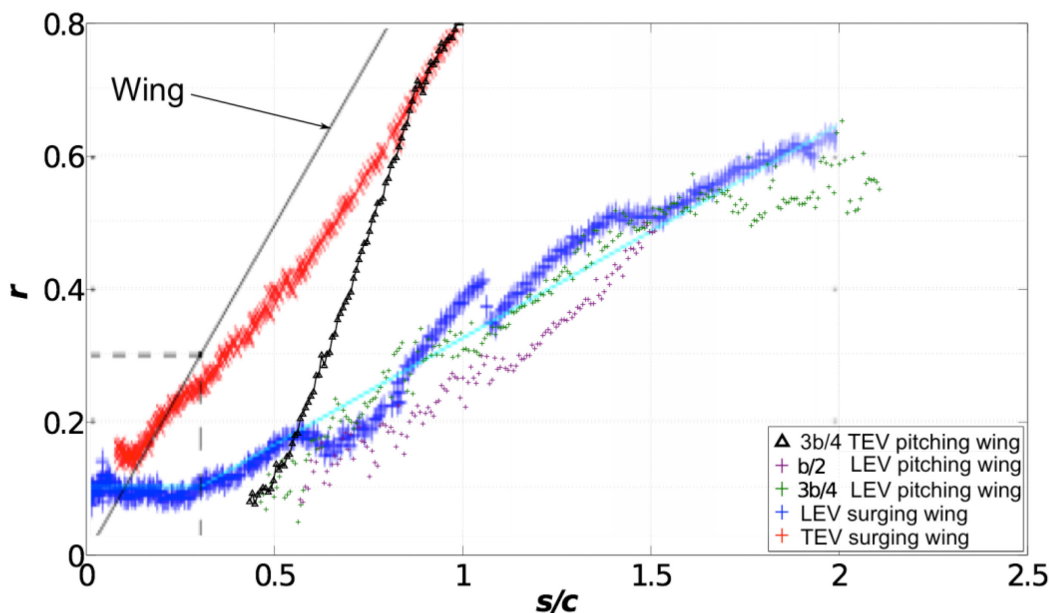
Figure 1-8: Distance of LEV and TEV from the Plate's Leading Edge, Plotted Against Chords-Traveled by the Plate, for the Fast (Once Chord Acceleration) Translational Surging and Pitching Plates.

To summarize, we estimate the unsteady force in the surge case as follows:

1) Add three contributions from virtual mass, vortex growth $\dot{\Gamma}_{LEV}$, and relative LEV/TEV motion.

2) Estimate virtual mass from potential flow result for inclined flat plate. This force occurs during the accelerating portion of the cycle.

3) Estimate the two circulatory contributions by assuming that Γ_{LEV} grows according to the Wagner function with a steady-state value equivalent to $2\pi\alpha$ (most likely Γ_{LEV} is well below this value).

4) Estimate the LEV trajectory by assuming that the distance between the LEV and the TEV grows at 50% of U_∞.

5) Estimate the distance between two vortices used in the $\dot{\Gamma}_{LEV}$ term to equate to chord length c.

6) In each case, non-dimensionalize the result by the asymptotic U_∞, this may require 'down-scaling' some of the equations given earlier during the accelerating portion of the surge cycle.

At large angles of attack (e.g., 45°) we need to be careful about force directions. The vortex lift acts in a direction normal to the line connecting LEV and TEV, while the non-circulatory force acts normal to the plate. The notional history of lift for the surging plate should then follow the schematic in Figure 1-9.
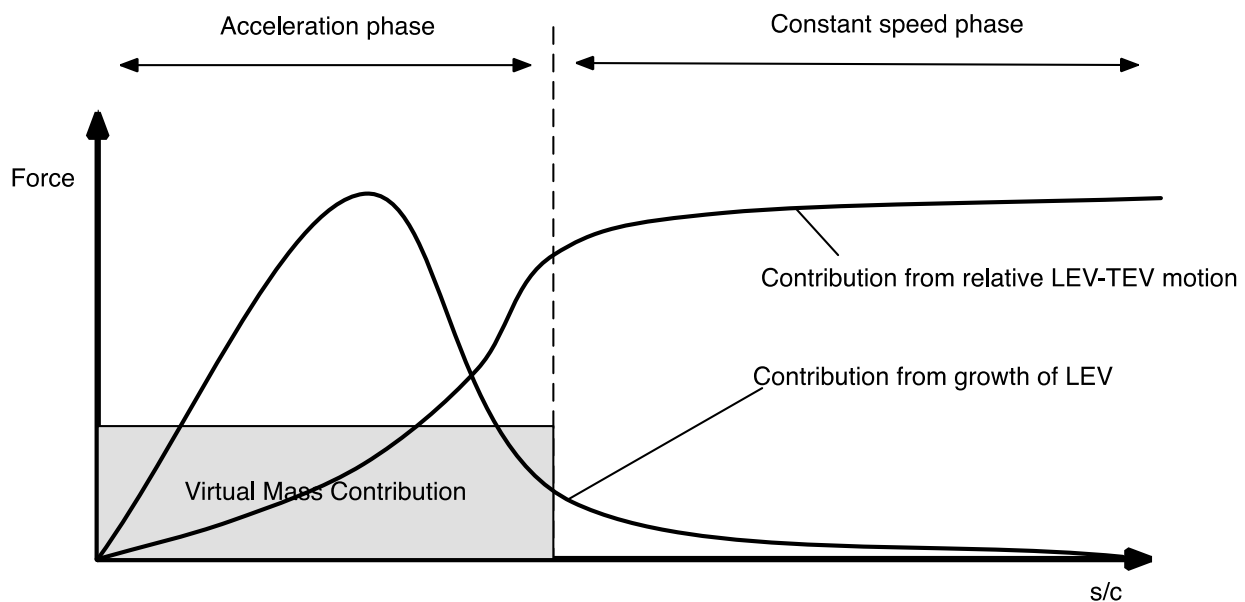
Figure 1-9: Notional Schematic for History of Lift for the Translational Surging Plate, with Contributions During the Phase of Motion where the Plate is Surging (Non-Zero Acceleration) and where the Steady-State Relative Free-Stream Speed has been Attained.

1.4.3   Analytical Derivations for the Pitching Plate

For the pitching plate (Figure 1-10) we again segregate lift into an inertial added mass term, and circulatory contributions. The latter now include a vortex lift term, and an additional contribution due to pitch rate. The latter has the same effect as a bound vortex.
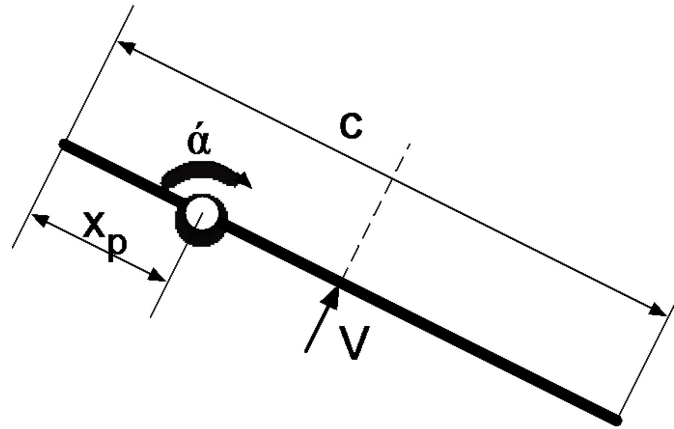
Figure 1-10: Nomenclature for 2D Pitching Plate, with Velocity Normal to the Plate, and Pivot Point Distance from the Leading Edge.

Using the coordinate system in Figure 1-10 we obtain for the normal velocity at the plate's mid-chord:

$$V = \left(\frac{c}{2} - x_p\right)\dot{\alpha}$$

The non-circulatory forces are non-zero only during the smoothing transients of the pitching motion, where the pitch-rate-derivative is non-zero. We can assume the added mass potential flow to be a superposition of a rotation about the mid-chord and a plunge (normal to the plate). The former does not generate a force (but it does generate a moment, which we ignore here). To compute the latter, we once again model the added mass contribution from the equivalent flow of a plate at 90° angle of attack and the mid-chord normal acceleration. Thus the magnitude of the non-circulatory force depends on the hinge location x_p, with rotations about the leading and trailing edges producing spikes of equal opposite magnitudes while rotation about the centre experiences no non-circulatory force. Using the above expression for V and the previously stated equation for the added mass force we obtain for the non-circulatory contribution to lift:

$$C_{L,non-circ} = \frac{\pi c^2}{4U^2}\left(1 - 2\frac{x_p}{c}\right)\ddot{\alpha}$$

Note that the above applies at zero angle of attack. At the end of the pitch (when the second spike appears), the force vector is rotated by α_{end}, thus the second spike is reduced:

$$C_{L,non-circ} = \cos(\alpha_{end})\frac{\pi c^2}{4U^2}\left(1 - 2\frac{x_p}{c}\right)\ddot{\alpha}$$

We next turn to the circulatory contributions. From the pitching motion there is an additional normal velocity V at the mid-chord, which increases the effective angle of attack by approximately V/U_∞. Assuming that this generates additional lift according to $2\pi\alpha$ would give the additional lift contribution (use the result for V derived above; the same result is given by Theodorsen [12]):

$$C_{L,2} = \frac{2\pi}{U_\infty}\left(\frac{c}{2} - x_p\right)\dot{\alpha}$$

However, if we continue to assume that bound circulation due to angle of attack is zero, then the lift contribution due to this additional effective angle of attack should already be included in the vortex lift. We thus propose to ignore this term.

The physical action of pitching the wing does however introduce a real rotation into the fluid. We believe that this is equivalent to a bound circulation (not included in the LEV), and should therefore generate an additional contribution to lift. The existence of this bound circulation can be explained in two ways: either a virtual camber caused by pitch (consider the motion of the TE relative to the LE while the fluid travels along the chord), or an additional circulation due to the plate's rotation (Figure 1-11).
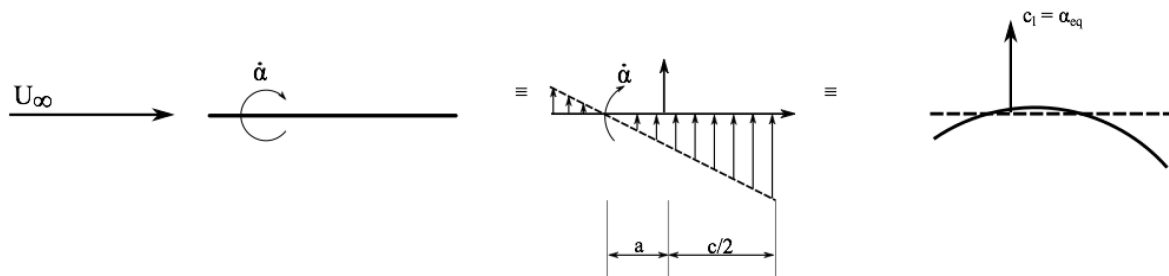
Figure 1-11: Schematic from Classical Unsteady Thin Airfoil Theory, Motivating Quasi-Steady Lift Contribution Due to Pitch; Pitching Produces an Effective Angle of Attack History, or Alternative, an Effective Camber.

Applying unsteady thin airfoil theory [12] to a pitching plate (Figure 1-11) gives the following result for lift coefficient:

$$c_l = 2\pi \left(\alpha + \frac{c\dot{\alpha}}{2U_\infty} \left(\frac{3}{2} - \frac{2x_p}{c} \right) \right)$$

This includes the steady contribution of $2\pi\alpha$ and the above virtual quasi-steady angle of attack. However, after removing both we are left with:

$$c_{l,circ} = \frac{\pi c}{2U_\infty} \dot{\alpha}$$

We can also explain this same result as an additional bound circulation introduced by the speed of rotation, akin to the Magnus effect:

$$\Gamma = \frac{\pi c^2}{4} \dot{\alpha}$$

Then we obtain the above lift contribution by applying $\rho U_\infty \Gamma$. To this we add the circulatory term from LEV and TEV circulation-change and relative displacement, exactly as in the section on the surging plate, except that one must account for the plate's changing incidence-angle during pitch, to isolate the lift component of the vortex-force. The full combination of lift history is schematically presented in Figure 1-12.
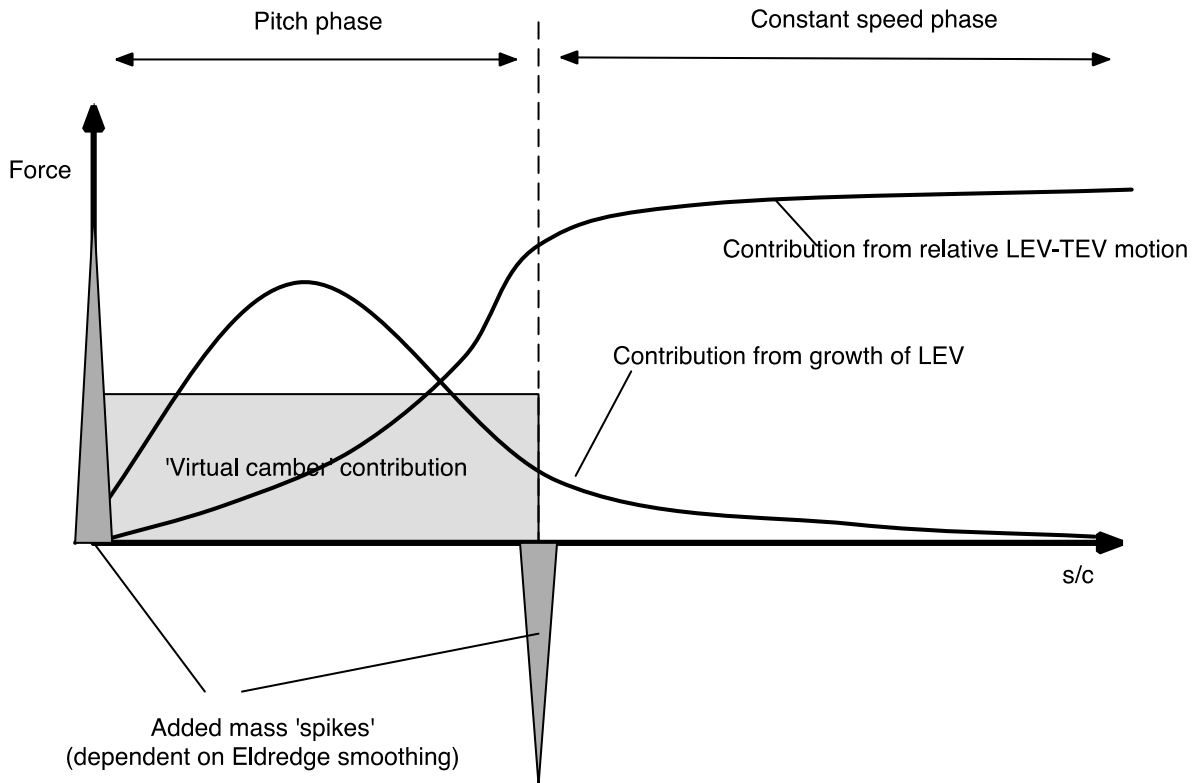
Figure 1-12: Notional Schematic for History of Lift for the Translational Pitching Plate, with Contributions During the Phase of Motion where the Plate is Pitching (Non-Zero Pitch Acceleration is Only During the Smoothing Transients at the Start and End of the Pitching Motion) and After the Final Incidence Angle has been Attained. The relative free-stream speed is assumed to always be constant.

1.5   PARAMETRIC VARIATIONS

The aim behind "canonical cases" is cross-vetting – but the potential parameter space is vast and unwieldy. With not claim of thoroughness, or even of eclectic selection of the most crucial archetypes, we consider the following variations beyond the "canonical":

1) Rectilinear cases were also studied in 2D or nominally in 2D, where the plate spans the test section of a water tunnel. Also, in translation and rotation, different aspect ratios were studied, noting effect of AR on the aerodynamic force coefficient histories, LEV and TEV vortex trajectories and circulation strengths, and spanwise trends therein. For rotational motions, variation of "root cut-out" [13] or the stand-off between the rotational fixed-point and the inboard wingtip could be considered as surrogate for Rossby number, but was not pursued here. The limit of infinite root cut-out in a rotational surge is a rectilinear surge.

2) Variations in Reynolds number, with examination of change in aerodynamic forces and LEV development.

3) Variation of reduced frequency, all the way to infinity (pitch in a zero free stream).

4) Variation of pitch pivot point along the plate's chord.

5) For rectilinear surge we compare linear acceleration profile defined with respect to convective time vs. wall-clock. Further, different smoothing transients are applied to nominally linear ramps defining the acceleration profile. And acceleration profiles can be taken as polynomials of various kind, instead of linear ramps.

6) Plunge resembling pitch.

7) Variations in plate leading edge shape, comparing a square leading edge with sharp corners, to a round leading edge.

8) Variations in peak incidence angle in pitch-ramps, and in the steady incidence angle for a surging-maneuver.

The work described in this Report is meant to be broadly expository, but obviously makes no aspiration to comprehensively cover all pitching/rotating/flapping plate research in the past several years. A good example of work followed by AVT-202, but not reported here, is that of D. Rockwel's group at LeHigh University, which conducted experimental investigations on the flow structure for plates primarily in rotational pitch and rotational surge. Findings for the rotational case include: sensitivity of the leading edge vortex and the overall three-dimensional vortex system to radius of gyration of the plate, which is to say root cut-out; preservation of a highly coherent leading edge vortex to large angles of rotation/travel distance; and preservation of the highly organized structure of the tip vortex-leading edge vortex system on a simultaneously pitching and rotating wing, relative to a purely rotating wing. Meanwhile, for pitching plates in translation, there is an evolution of an "arch vortex", following that originally computed by Visbal [14]. For details, see Refs. [15], [16], [17], [18], [19] and [20].

Chapter 2 – FACILITIES AND METHODS

High rate, high amplitude motions are more readily studied in liquids (water, water/glycerin mixtures and the like) than in air [21]. The ratio of model inertia (the model's physical mass) to fluid-dynamic loads is much lower in liquids than in air, leading to improved signal-to-noise ratio. PIV particle seeding is also easier in the liquid phase [22].

2.1   AFRL

AFRL data were taken in the United States Air Force Research Lab, Aerospace Systems Directorate's water tunnel, by K.O. Granlund and M.V. Ol, and separately by P. Mancini and A. Jones, thus producing two data sets. The tunnel is of free-surface type, with test section 18" wide, 24" high and 96" long. Nominal turbulence intensity (measured by particle image velocimetry and laser-Doppler velocimetry) is 0.4% at 15 – 40 cm/s, and speed range is 3 – 90 cm/s. The tunnel is powered by a 16"-diameter axial impeller pump, flowing water through a vertical perforated distribution pipe into the intake plenum, a settling chamber with 3 screens and 2 honeycombs, and 3.8:1 contraction. The tunnel is fitted with three degree of freedom motion system, consisting of three linear electric servomotors and a proportional-integral-derivative programmable controller. Two motors vertically oriented above the test section actuate pitch and plunge with up to 8" stroke, while a third motor above the aft end of the test section has 48" stroke of fore-aft translation, or surge. All rectilinear motions are possible, other than continuous rotation in pitch (pitch is limited to 0° – 90° or ± 45°). Translational surging motions are via the horizontal motor, with the tunnel shut off, and the two vertical motors set to place the model at 45-degrees incidence. The model mounted horizontally in the test section, with a central support also housing the load cell. Translational pitch uses the same orientation. In the typical translational arrangement, the plate is mounted offset from the load cell by a 2.25" 3D-printed plastic strut Rotational surge uses all three motors, with the model hanging vertically from an arm offset from the load cell, with the load cell reference-center at the point of rotation.

The equipment suite includes:

- PCO Dimax 4Mpix 1279 frame-per-second, 12-bit CMOS camera, for PIV and flow visualization, typically mounted laterally from the test section.

- Photonix DM55 55 mJ/pulse 3 KHz single-cavity Nd:YLF laser, fired asynchronously for PIV, and synchronously for planar laser fluorescence for flow visualization by injection of dye from the plate leading/trailing edges.

- ATI NANO-25 and NANO-17 [23] 6-component load cells, triggered by the motion-rig, mounted in a frame connected to "plunge rods" from the two vertical linear motors.

- Positive-displacement syringe pump for adjustable-flow of dye (food coloring or rhodamine, the latter for planar laser fluorescence).

Photographs of the facility and typical models are shown in Figure 2-1. PIV is of the conventional 2D type, using Lavison's DaVis 8.1 software and the 5 μm Vestosint seeding particles. With a multi-pass, variable window-size method, the first pass used a 48 x 48 pixel window with 1:1 square weighting and 50% overlap, and two further passes used 32 x 32 pixel windows with 1:1 circular weighting and 75% overlap. Post-processing was kept to a minimum by only utilizing a remove-and-replace median filter of 2 standard deviations.

(a)
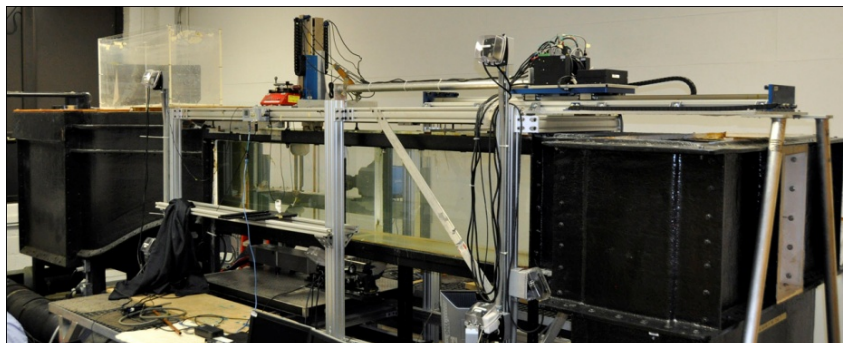
(b)
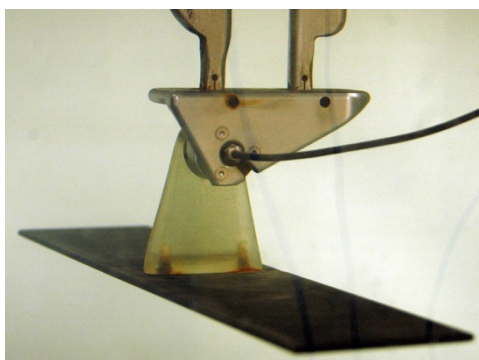
(c)

Figure 2-1: AFRL Water Tunnel. Electric motion-rig, with a horizontal linear motor actuating in the streamwise direction a carriage with two vertical linear motors (a); the latter are responsible for pitch/plunge motions, and the former for surge. Overall view of water tunnel, from intake plenum to test section and exit plenum (b). AR = 4 plate installed for rectilinear motions (c).

Processing/filtering of force-data is discussed in Granlund *et al*. [24], with low-pass filtering ultimately limited by the system natural frequency, typically at ~ 13 Hz (as determined by strike-test of the model) in post-processing, and at 18 Hz in the load-cell's native acquisition system, with sampling at 1 KHz.

For translations, the principal case was an AR = 4 carbon fiber plate with c = 76.2 mm and thickness ~ 3 mm. Due to the length of the test section, maximum translation distance was limited to approximately 14 c for the surge cases. A typical model installation is shown in lower part of Figure 2-1.

2.2   ARL

The U.S. Army Research Lab (ARL) group (K. Kroninger, M. Munson, A. Harrington and B. Cohen) used an oil tank for force/moment data on rotating wings. The hexagonal tank is 63.5 cm across and 76 cm tall) Figure 2-2, filled with mineral oil of 850 kg/m^3 density and 16.8 mPa-s viscosity at room temperature.

(a)   **(b)**   **(c)**
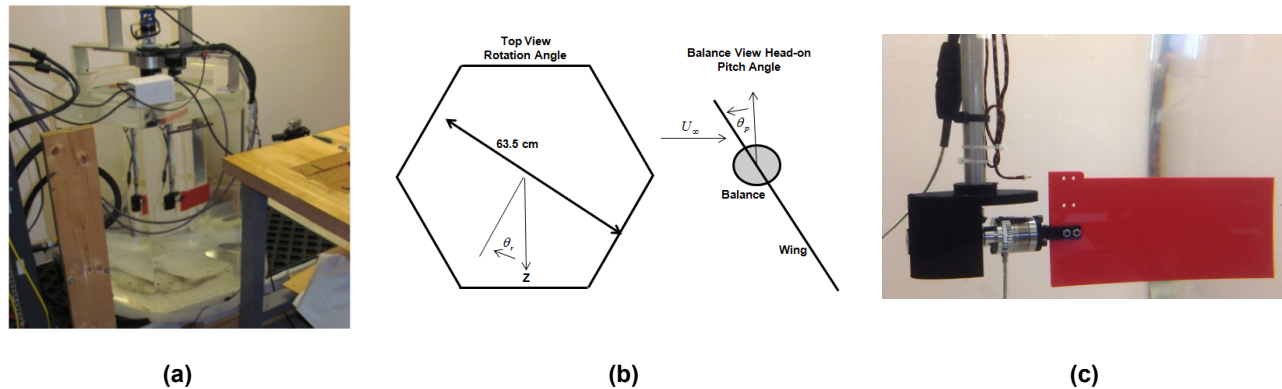
Figure 2-2: The ARL Oil Tank Facility. (a) The hexagonal tank with supporting infrastructure; (b) The definition of the motion coordinate systems for the rotation and pitch degrees of freedom; and (c) The wing model mounted on the wing mid-chord in a vertical orientation.

The model is supported on a six component balance, with the axis of rotation for the wing in the center of the tank. Rotation is controlled by a stepper motor from the top of the tank, with the motion transmitted down the larger of two concentric shafts. The mechanics for the wing pitching motion are mounted in the rotating frame of reference with a second stepper motor controlling the wing pitch through the center shaft. Utilizing micro-stepping, a resolution of 2000 steps per revolution was achieved. Both axes of motion have a gear down ratio from the motor to the axis of rotation, resulting in positioning resolutions of 10,000 and 4000 steps per revolution in the rotation and pitch axes, respectively. From visual inspection, it is estimated that +/-1.5° of alignment accuracy can be achieved, plus another +/1.5° of backlash. The model, depicted in Figure 2-2(c), has AR = 2 (based on the semi-span and area), a rectangular planform, 15.2 cm by 7.6 cm and a thickness of 3.7 mm. It is designed to reside a half chord length from the axis of rotation. The wing tip is about 5/3 chords from the tank wall at the closest points in the rotation, so a small influence from the presence of the wall might be anticipated.

Two sets of wing kinematics were explored. One is rotation at a pitch angle of 45° (Figure 2-2), with a surging start. The acceleration for the surging start is completed in about two chord lengths following the profile of a smoothed quadratic polynomial spline for the commanded acceleration. The second is a pitch-up from a pitch angle of 90° to 45° while already rotating. The pitch-up is completed within the first revolution of the wing over 8 chord lengths of travel. The wing displacement over time is described by the Eldredge smoothing function [7] with a value of 0.05 for the reduced frequency and 11 for the smoothing parameter. The distance travelled is measured at the ¾ span location for both cases and 4π chord lengths equals a revolution.

The forces and moments at the base of the wing are measured with a six component balance, with a range of +/- 500 N in its longitudinal axis (the wing's spanwise axis) and +/- 125 N in the lateral directions. The moment limits in all axes are 3 N-m. The measurement accuracy is described by the manufacturer to be better than 0.01% of the full-scale range for all axes [23]. Voltage supplied to the balance and the analog outputs is routed through a slip ring out of the rotational frame to a signal conditioning unit and ultimately to an Analog-to-Digital Converted (ADC). The angular motions of the rotational and pitch axes are each monitored with an optical quadrature encoder mounted on each motor.

The force and encoder signals were all measured simultaneously with a high-speed ADC, sampled at 51,200 Hz. The high-speed ADC applies a combination of a digital and analog filtering to prevent aliasing. The resulting filtering behavior is a low pass filter with a cut-off frequency that is one half the sample rate (the Nyquist

frequency) [25]. A zeroing process was performed just before and after each data collection run to account for balance drift and the model's weight. The force time histories were further filtered with a discrete truncated approximation of an ideal low pass filter. A 10 Hertz cut-off frequency, applied over a four second range centered around the current time step, was utilized for the convolution of the ideal filter impulse with the force time histories. The difference between the digitally filtered data and the original time history was used to form a moving standard deviation. The moving standard deviation is calculated from 100 ms of data, the period of the 10 Hz cut-off frequency. Error bars representing three standard deviations are plotted with the digitally filtered data reflecting a 99% percent confidence interval assuming a Gaussian distribution of signal noise [25].

2.3   ASELSAN INC.

The Aselsan group (C. Gozukara) computed the translational cases using ANSYS Fluent 15.0 [26], with an unstructured moving mesh composed of two zones; the outer grid surrounds an inner one, moving with the plate without going through a deformation. The outer zone is morphed and regenerated according to the predefined deformation rules to enable the inner zone to move. The mid-span cross-section grid slices are shown in Figure 2-3. Grids for RANS computations have 19426144 and 16767196 tetrahedral elements for translational surge and translational pitch cases, respectively. Slightly smaller grids are used for laminar computations. The domain is 80 c long, 40 c wide and 40 c high for the translational cases, and 60 c long, 40 c wide and 60 c for the pitching cases. The plate has a chord of 60 mm, thickness of 2 mm, and AR = 4. Reynolds number based on chord and terminal velocity is 3600 and 10,000, the former taken as laminar, and the latter run as RANS with a k-ε turbulence model [27]. One chord of travel is divided into 500 equal time steps for all cases. The initial conditions for the translational pitch cases are established by performing steady-state computations with zero angle of incidence.
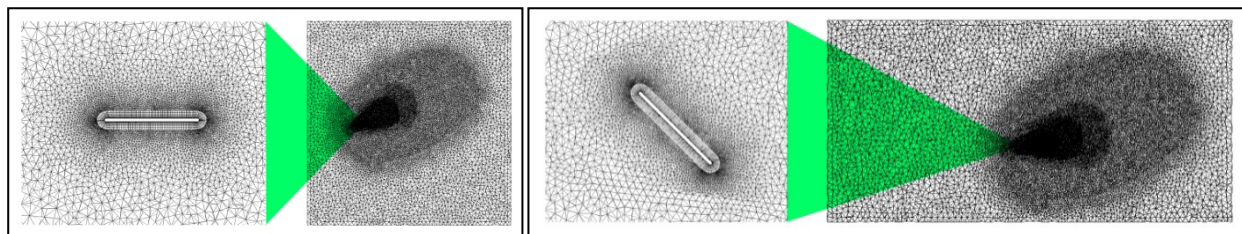
**Figure 2-3: Cross-Sectional View of Unstructured Mesh
for Pitching (Left) and Surging (Right) Translations.**

2.4   CAMBRIDGE UNIVERSITY

The Cambridge University group (R. Stevens and H. Babinsky) performed experiments in the Cambridge Department of Engineering water towing tank (schematic in Figure 2-4). The tank has a 2 m long working section with clear side walls and floor for laser and camera optical access. The operational cross-section is 0.8 m². For an AR = 2 wing, maximum blockage (at α = 45°) is 2.5%. A settling time between experiments of 20 minutes is deemed sufficient to achieve a quiescent fluid as determined by Jones [28]. The computer-controlled carriage on top of the tank can achieve a positional accuracy of +/-0.25%. Velocity is corrected for temperature variations greater than 1°C, giving a maximum error in freestream Reynolds number of O (1.25%).
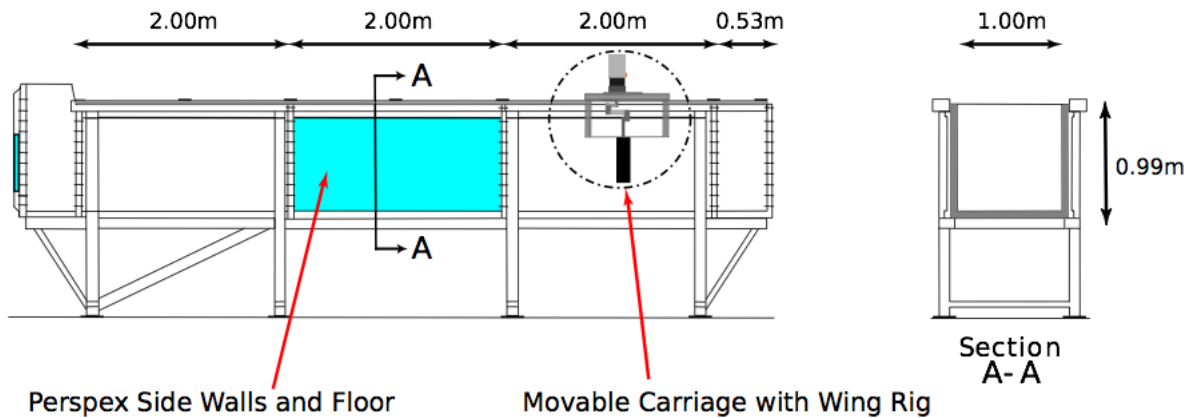
Figure 2-4: Cambridge University Department of Engineering Tow Tank.

The pitching rig (Figure 2-5) is used for both surging and pitching experiments. A skim plate is used to remove the influence of water free-surface effects and to act as a symmetry plane, giving an effective AR of twice the physical AR. Two different wings are used for experiments, one with a physical AR = 4 and one with AR = 2 (giving effective ARs of 8 and 4 respectively). For surging experiments the pitch motor is not activated and is fixed in place at the desired incidence. During pitching the wing incidence is verified using an algorithm based on the pixel illumination intensity of the wing reflection in PIV images and is accurate to within $3 - 4$ pixels, giving a typical measured error over commanded incidence of less than $1 - 2$ %.
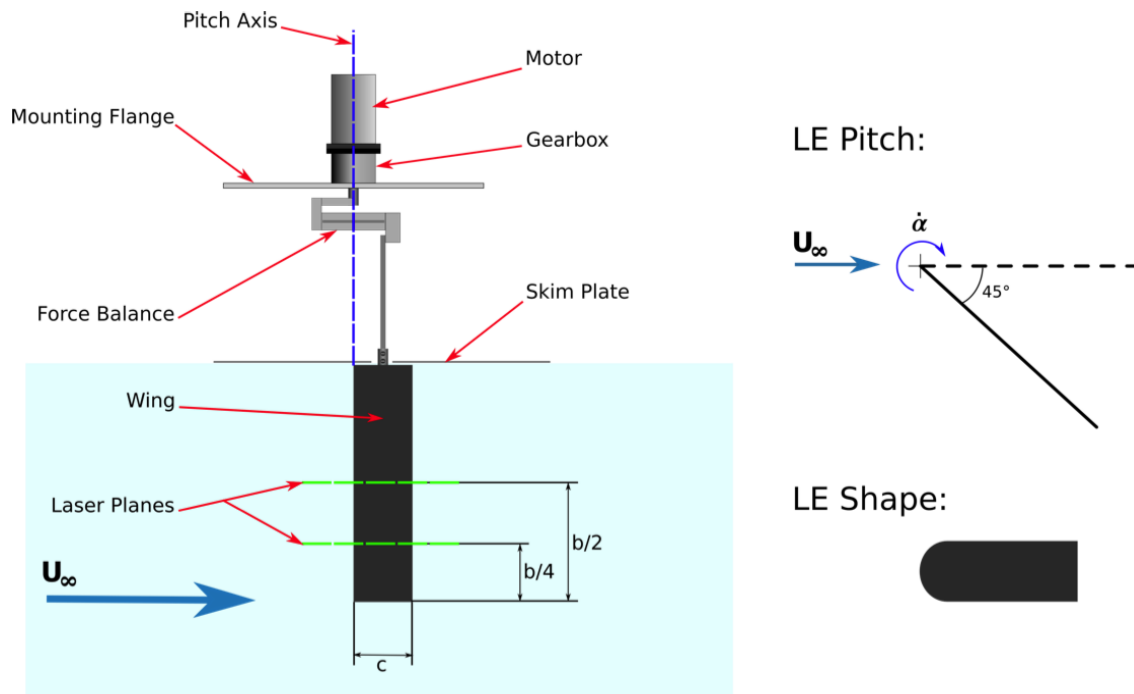
Figure 2-5: Cambridge University Tow Tank, Model Installation Scheme.

Lift and drag are measured with a force balance of the strain gauge load cell type. The two-component balance has a range of +/- 50 N and an accuracy within 0.01 N. Data is averaged over 10 runs, and smoothed using a moving-point average span of 100 data points with the endpoints treated by having progressively smaller span widths. The forces on the wing in air are also obtained and subtracted from the forces in water to remove the inertia force of the wing.

Dye flow visualization is performed using a dye composed of water and milk. Milk improves the stability of dye filaments, retarding diffusion of the filament into the main bulk of the fluid; milk also has the advantage of possessing good reflective properties [29]. A LaVision Flow Master planar PIV system uses TiO_2 particles for seeding, and camera with frame rate capability of more than 5×10^4 Hz, at a resolution of 1024 x 1024 pixels. The field of view is 240 mm x 240 mm. Processing is with two passes of each interrogation window size, with windows decreasing from 32 x 32 to 16 x 16 pixels with Gaussian weighting and a 50% window overlap. Each vector represents an area of 1.6 x 1.6 mm^2 giving 75 vectors per chord length.

The γ_2 vortex detection scheme of Graftieaux *et al*. [9] is employed to identify the position of vortex cores in PIV data (contour centroid method). Using the LEV centre calculated by γ_2 as the epicentre, for each frame, a series of circular contours are defined with increasing radius. The circulation (Γ) around each contour is calculated and plotted with respect to contour radius. A best-fit Lamb-Oseen radial variation in Γ (Eq. 2-1) is applied to the data, whence Γ_{max} can be inferred. The calculated error in Γ from the fit of a free Lamb-Oseen vortex is 0.23%:

$$\Gamma = \Gamma_\infty \left(1 - \exp\left(\frac{-r^2}{r_c^2} \right) \right) \qquad \text{(Eq. 2-1)}$$

r = radius of given contour.

r_c = vortex core radius.

Equation n: Lamb-Oseen Circulation.

2.5   DLR

The German Aerospace Centre (DLR; H. Ehlers and R. Konrath), Institute for Aerodynamics and Flow Technology, performed Tomographic PIV experiments in the TU-Braunschweig wind tunnel, described below. Measurements capture phase-locked recordings (250 image pairs per chordwise position) of the flowfield above the moving wing for the 6 *c* slow pitch case. A schematic of the measurement set-up is shown in Figure 2-6. Providing 400 mJ per pulse, a Nd:YAG laser (BigSky CFR) illuminates small DEHS tracer particles. The laser light volume was directed in a span-wise direction, with cross-section of $h \times t = 50 \times 20$ mm^2. The width of the measurement domain was about 120 mm, starting 0.03 b beyond the wing tip. Flow field data is not available between symmetry plane and $yn \approx 0.125\ b$ in span-wise direction. Four high resolution CMOS cameras (PCO.edge: 2560×2160 pixel, 16-bit) are arranged with two on each side of the test rig (Figure 2-6). A mirror was used to reflect the laser beam back, enhancing the scattered light intensity for the backward facing cameras. Due to the limited thickness of the laser volume, measurements had to be applied successively, scanning the flowfield in a chord-wise direction. The total measurement domain between leading and trailing edge consists of six sub-volumes. Tomo-PIV recordings have been taken for the time instances t* = 3 and 4.

(a)   **(b)**
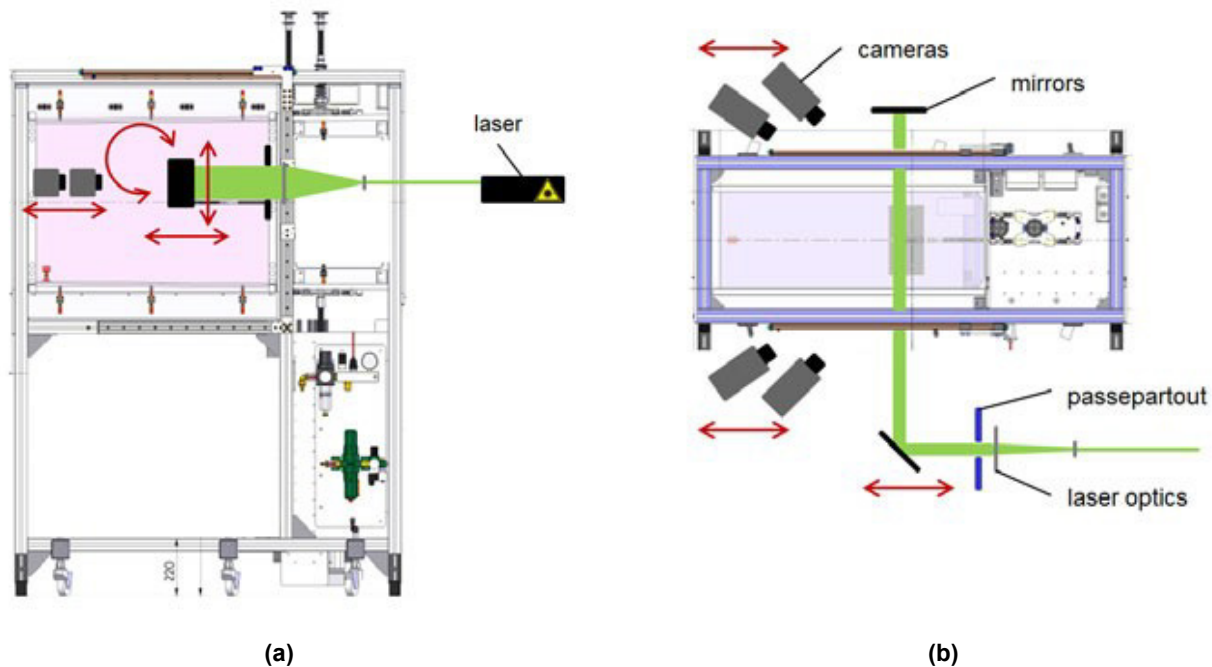
**Figure 2-6: DLR Tomographic-PIV Optics Set-Up in TU-Braunschweig
Wind Tunnel: Side View (a) and Top View (b).**

The data reduction procedure, using in-house software, is divided into three sub-routines: The camera calibration (which includes volume self-calibration), reconstruction of the particle distribution and a 3D cross-correlation routine. The reconstruction of the particle distributions was done using a SMART algorithm with MLOS initialization [30], [31]. The evaluation domain of every volume is represented by a voxel-space of $912 \times 2177 \times 329$ voxel (resolution ≈ 18.2 voxel/mm). The voxel-to-pixel ratio was set to a value of 0.8, to allow an effective processing of the large amount of data. The recovered volume pairs of three-dimensional particle distributions are then processed with a cross-correlation-based displacement estimation algorithm. Just as in established 2-C processing schemes, the 3D algorithm employs a resolution pyramid which starts at a rather coarse grid and stepwise increases resolution while continually updating a predictor field. In the present application, a three level resolution pyramid was used with a final window size of 48^3 voxel (75% overlap), resulting in vector volumes with $75 \times 175 \times 25$ nodes. At this resolution volume deformation was applied twice using a cubic b-spline of order 3.

2.6 FLORIDA STATE UNIVERSITY

The Florida State University group (K. Taira and R. Jantzen) performed numerical simulations of translational pitch and surge using an immersed boundary method on a Cartesian Lagrangian grid [32], at sufficiently low Reynolds numbers so as to enable direct numerical simulation without sub-grid modeling or filtering. The spatial domain was discretized with a non-uniform Cartesian grid, with its spatial convergence verified. For pitching simulations, uniform flow was specified at the inlet and the plate was fixed at zero angle of attack to develop a laminar boundary layer. Once the boundary layer reached a steady-state, the pitching motion was initiated. For the surging simulation, the background flow was accelerated to match the experimental surging profile with the plate fixed on the grid. For the cases presented herein, the Reynolds number has been set to 300 based on the

translation and terminal velocity values for pitching and surging cases, respectively. The numerical solver and computational set-up have been verified and validated extensively, including flows over low-aspect-ratio plates [33] and comparisons with experiment [34]. A typical result, of 3D isometric visualization of vorticity contours for the AR = 4 surging plate, is given in Figure 2-7.
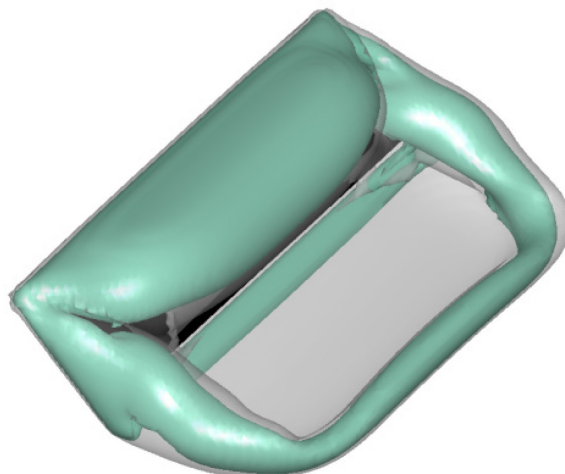
Figure 2-7: Typical Results of Florida State University Immersed Boundary Method Solver, Contour Levels of Vorticity for the "Fast" AR = 4 Plate Surging in Translation.

2.7   ISTANBUL TECHNICAL UNIVERSITY

Experiments by the Istanbul Technical University (ITU) group (O. Cetiner and O. Son) were performed in the close-circuit, free-surface, large-scale water channel located in the Trisonic Laboratories at the Faculty of Aeronautics and Astronautics of Istanbul Technical University. The cross-sectional dimensions of the main test section are 1010 mm × 790 mm. The models are mounted in a vertical cantilevered arrangement in the water channel about their leading edge as the pivot point. The connection rod connects the models to the servo motor from their leading edge to provide a ramp type pitch up motion via a coupling system. The chord length of the models is 10 cm and models have a span of 20, 30 or 40 cm to obtain different aspect ratios. The models are thin rectangular plates ($t = 0.5$ cm) with sharp and round edges and they are manufactured of transparent Plexiglas® to allow laser light to illuminate both the suction and pressure sides. The experiments are conducted at a Reynolds number of 10,000 which corresponds to a flow speed of $U = 0.1$ m/s.

Particle Image Velocimetry (PIV) technique is used to record flowfields around the models and therefore to analyze the vortical structures. The flow is illuminated by a dual cavity Nd:Yag laser (max. 120 mJ/pulse) and the water is seeded with silver coated hollow glass spheres with a mean diameter of 10 μm. Two 10-bit cameras with 1600 × 1200 pixels resolution are positioned underneath the water channel to capture the flow structures around the flat plate and in its near-wake. Two images from the two cameras are stitched before interrogation using two marker points in the illumination plane. Stitched PIV images are then interrogated using a double frame, cross-correlation technique with a window size of 64 × 64 pixels and 50% overlapping in each direction. The final grid resolution of velocity vectors is 3.5 mm × 3.5 mm in the plane of the flow. The resulting measurement plane is represented with approximately 3240 velocity vectors. The experimental set-up is shown in Figure 2-8.
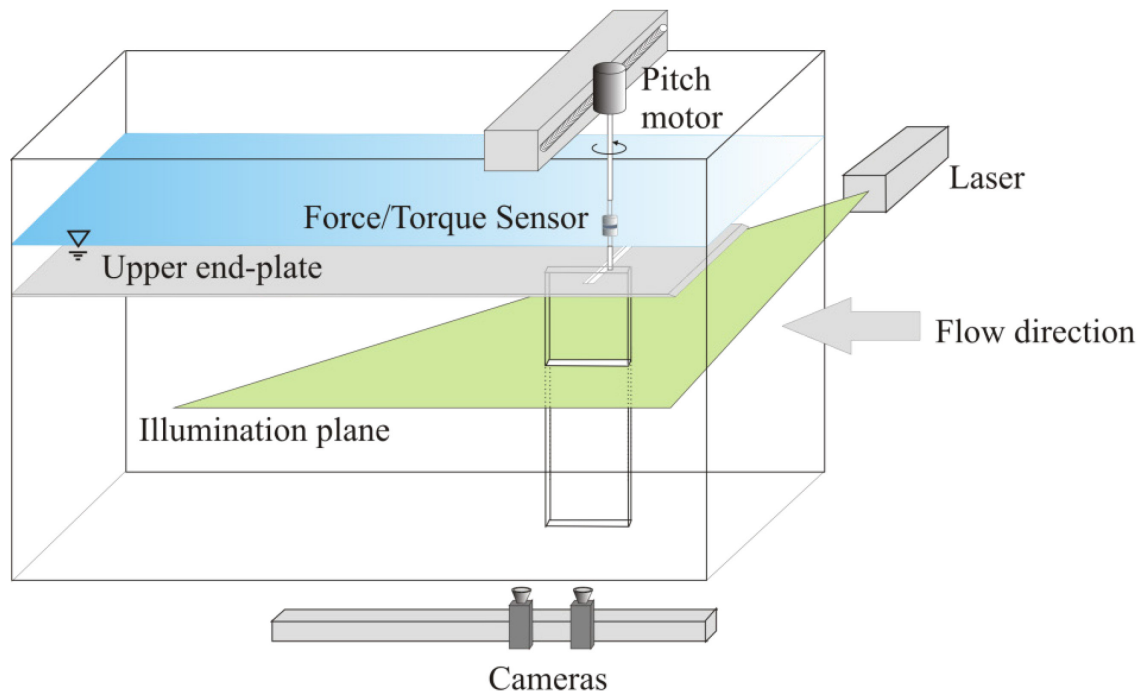
Figure 2-8: ITU Experimental Set-Up.

A six-component ATI NANO-17 IP68 Force/Torque (F/T) sensor [23] is used to measure the forces and moments acting on the model. The sensor is attached on the rod between the model and the pitch servo motor, oriented with its cylindrical z-axis normal to the pitch plane. The pitch-up motions of the airfoil are accomplished with a Kollmorgen/Danaher Motion AKM33E servo motor. The models are subjected to perform two types of motion: fast and slow. The model starts from 0° and reaches to its final angle of attack of 45° in 1 second for the fast motion and 6 seconds for the slow motion corresponding to 1 and 6 convective times respectively. Motor motion profiles are generated by a signal generator Labview VI (Virtual Instrument) for the given amplitude and duration. The same VI triggers both the force data acquisition and the PIV system. The force measurement starts 5 seconds before the beginning of the pitch motion; the synchronization with the PIV system is achieved using a National Instruments PCI-6601 timer device.

2.8 TECHNICAL UNIVERSITY OF BRAUNSCHWEIG

Experiments at the Technical University of Braunschweig (R. Radespiel and R. Wokoeck) were carried out in the LNB wind tunnel (Figure 2-9), a continuous Eiffel type tunnel with room recirculation designed to offer high quality flow with low perturbation. A typical turbulence level of $Tu < 0.1\%$ and a core velocity uniformity of 99% are achieved by a large nozzle contract ratio of 16 and several means of flow treatment and sound and vibration dampening.

(a)   (b)
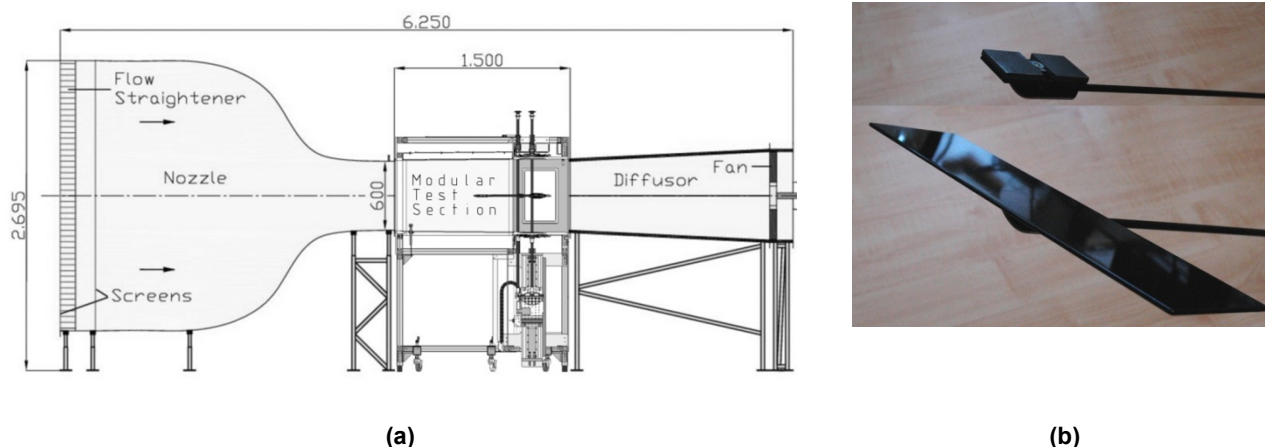
Figure 2-9: Wind Tunnel at TU-Braunschweig (a); Test Article and Inertial Dummy (b).

The dynamic model support (Figure 2-9) is integrated into one of the 0.6 m high, 0.4 m wide and 1.5 m long modular test sections. To meet the required precision of high-speed flapping wing motions, it is driven by two linear direct electric motors, each delivering up to 700 N. The drives are controlled in a real-time closed loop with a 12-bit virtual cam resolution plus smooth interpolation and on the fly correction, with accuracy of $\leq \pm 0.05$ mm in vertical position and $\leq \pm 0.1°$ angles of attack. Whilst the support is capable of carrying out pure plunging motions precisely, any motion containing a rotation portion is accompanied by a small unwanted horizontal translation.

Forces were measured with the 107 mm long and 11.2 mm in diameter six components internal strain gauge balance *W637*. Together with a *Hottinger Baldwin Messtechnik MGCplus* strain amplifier to process the balance signals, an accuracy of 0.015% of full scale is achieved. The full scale for the drag force is ± 7 N and for the normal force is ± 20 N, whilst the pitching moment may range up to ± 0.75 Nm. The force measurements are run through a 10 Hz low pass Bessel-filter to dampen out mechanical vibrations of the model support. The pitch moment is then referred to ¼ chord.

To separate the aerodynamic forces from the inertial forces, the latter are determined in a second measurement run with the wind tunnel off and an inertial dummy replacing the model. The dummy has to have the same mass, centre of mass and inertial moment in reference to the pitching axis as the model, but interacts much less with the air due to its compact, wingless design. Tuning the inertial dummy to the model values is an iterative process carried out with a fine weight balance, a tilting balance and a pendulum. The model was built by DLR in sandwich structure with layers of carbon fiber reinforced plastics around a foam core. The rectangular wing has fully round edges, a chord of 70 mm, a span of 280 mm and a thickness of 2.35 mm. Dummy and model as shown in Figure 2-9(b) both feature a body beneath the wing to cover the balance from wind and share a weight of 72.65 g.

2.9   TECHNICAL UNIVERSITY OF DELFT

The TU-Delft group (M. Percin and B.W. van Oudheusden) experiments were performed in a water tank at the Aerodynamics Laboratory of Delft University of Technology. The octagonal water tank (600 mm of diameter and 600 mm of height) is made of Plexiglas® allowing full optical access (Figure 2-10(a)). A Plexiglas® flat plate test-article has sharp edges, thickness of 3 mm, rectangular planform, length (*c*) of 50 mm, a span length (*b*)

of 100 mm, resulting in an aspect ratio of 2 (Figure 2-10(b)). The wing model was positioned at approximately 5 c distance from the water surface, 7 c distance from the bottom wall and 5 c (wing tip to wall) distance from the side wall. A brushed DC motor with a gearbox (gear ratio of 132:1) connected to the main vertical axis (y axis) of the set-up drove the wing in revolution, while pitch about the wing's leading edge (z axis) was by a waterproof servo motor that was placed in the servo box which also contains the force sensor.

(a)   (b)
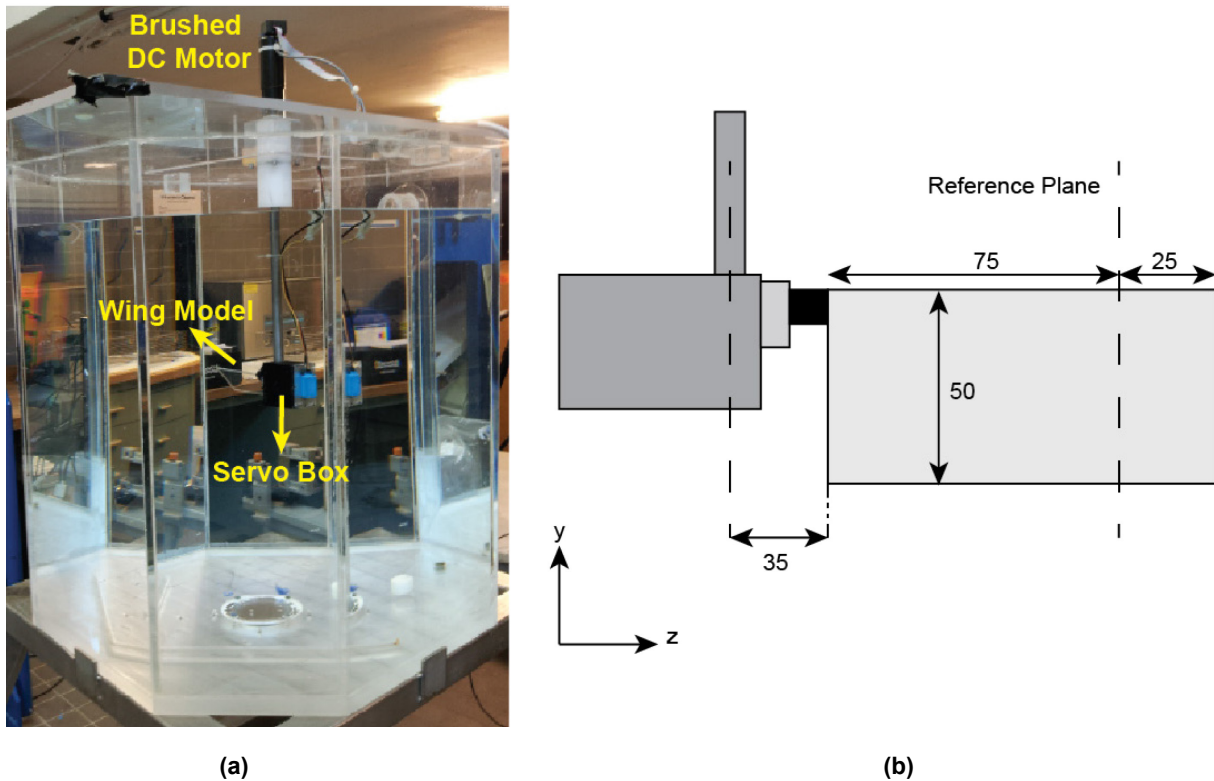
Figure 2-10: (a) Experimental Arrangement in the Water Tank; (b) Dimensions of the Wing Model.

The distance between the root chord and the rotation axis is 35 mm (0.7 c) and the radius of gyration is $r = 90$ mm, resulting in Rossby number of $r/c = 1.8$. The motion (Figure 2-11) is initiated by a constant acceleration from rest to $V_t = 0.2$ m/s (corresponding to the Reynolds number of 10,000 based on c) at an angle of attack (α) of 0° over $\Delta t^* = 2$ ($\Delta s^* = 1$, corresponding to a revolution angle $\Delta \varphi = 25.8°$); this is then followed by a period in which the wing pitches up to $\alpha = 45°$ over $\Delta t^* = 1$ ($\Delta s^* = 1$) at a constant pitch rate, after which the wing continues to revolve at a constant rate at $\alpha = 45°$. On the other hand, in the revolving surge case (Figure 2-10(b)), the wing motion is initiated at $\alpha = 45°$ angle of attack with an acceleration period from rest to $V_t = 0.2$ m/s over $\Delta t^* = 2$ ($\Delta s^* = 1$) after which the wing remains to revolve at a constant angle of attack and constant rate. Note that for sake of comparison between the two cases, the origin for both the non-dimensional elapsed time ($t^* = 0$) and distance travelled ($s^* = 0$) are defined, such that they coincide with the start of the pitch/surge motion, respectively, with the terminal condition being reached at $s^* = 1$.
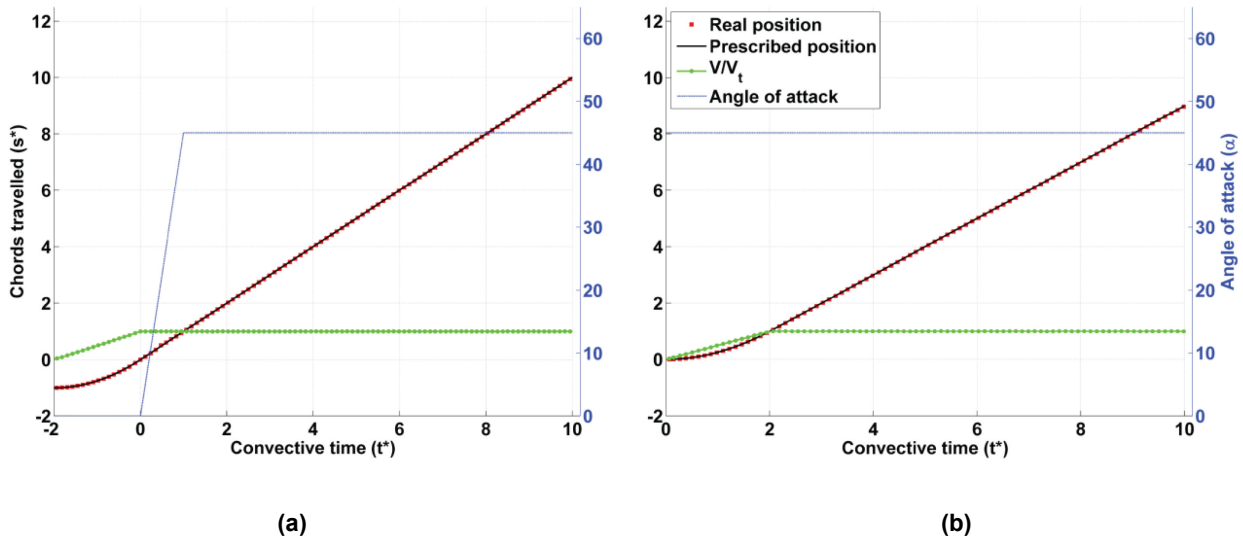
Figure 2-11: Kinematics of the (a) Revolving-Pitching and (b) Revolving-Surging Motions.

Real-time position and rotational velocity information was acquired from the motor encoder at 33 Hz data acquisition frequency to verify the actual motion kinematics. In all experiments, the entire travel distance is 14 c ($s^* = 14$) corresponding to one full rotation. Although the forces were captured for the full motion, flowfield measurements were limited to the first 7 c of travel.

Six components of forces and moments were measured with a water submergible ATI Nano17/IP68 force sensor. Force signals were acquired at 2 kHz data acquisition frequency via in-house developed LabVIEW code that also controls the motors and synchronizes the wing motion with the force data acquisition and the PIV measurements. Ensemble averaging of forces and moments was performed over 20 repetitions of the experiments for the pitching case and 50 repetitions for the surging case. The averaged force and moment data were then filtered to remove electrical noise and mechanical vibrations of the driving system as well as the natural frequency of the test rig (16.6 Hz) in the signal, by means of a Chebyshev Type II low-pass filter with a cut-off frequency of 15 Hz. A forward-backward filtering technique was used in order to prevent time-shift of the data. Lift and drag are normalized by use of the terminal velocity V_t and wing surface area, in order to produce force coefficients (c_L and c_D, respectively). The uncertainty in the reported force values were calculated based on the 15 Hz low-pass filtered signal which results in 0.5% and 1.5% average uncertainties with respect to steady-state mean values in the revolving-surging and revolving-pitching cases, respectively.

Three-dimensional quantitative information of the flow around the outboard section of the wing model was acquired via phase-locked Tomographic PIV [22]. At each run, a double-frame image was captured at a specific phase of the wing motion. Repeated runs were performed with sufficient time intervals to restore quiescent conditions in the water tank. The measurement volume of 90 × 70 × 25 mm³ in size (Figure 2-12(a)) was positioned at two different spanwise locations side by side as shown in Figure 2-12(b). Then, a Kriging regression technique [35] with a correlating length of 2 mm in all directions was used in order to combine the two measurement volumes and to provide a complete visualization of the flowfield. The starting position of the wing was changed based on the desired measurement phase so to have the wing always oriented normal to the measurement volume during image acquisition. For each measurement phase, the experiments were repeated for three times and vector fields are ensemble-averaged in order to improve signal-to-noise ratio.
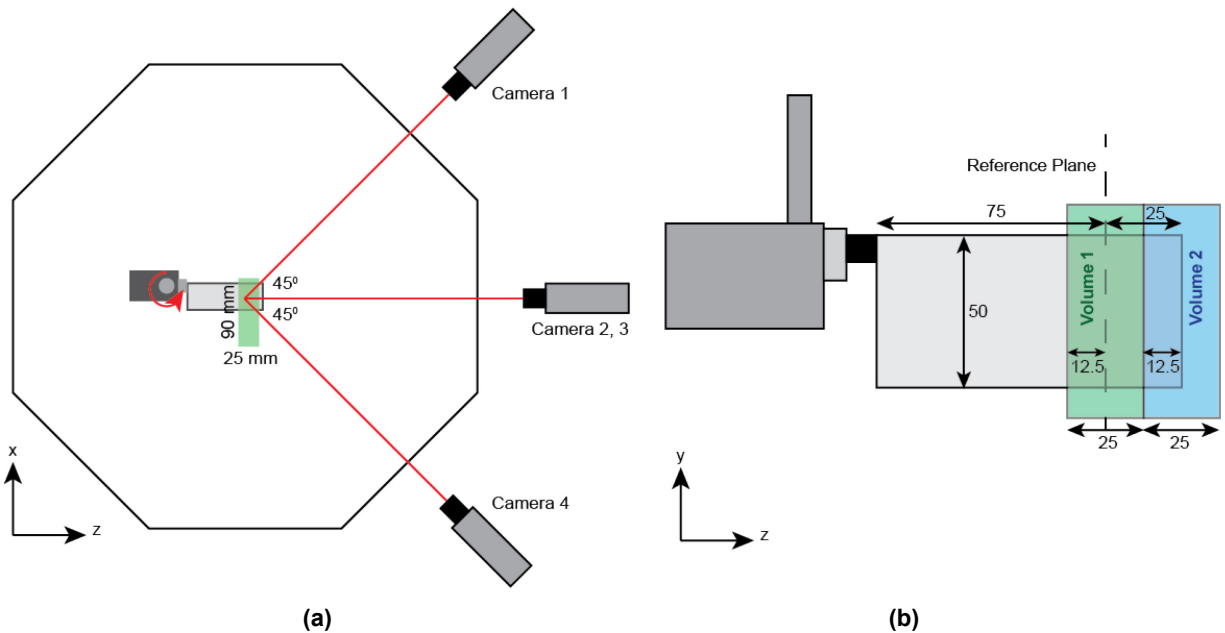
**Figure 2-12: (a) Sketch of the Top View of the Experimental Set-Up With Camera
Arrangement; (b) Wing Model and Measurement Volume Arrangement.**

The volume was illuminated by a double-pulsed Nd:Yag laser at a wavelength of 532 nm. Polyamide spherical particles of 56 μm diameter were employed as tracer particles at a concentration of 0.4 particles/mm^3. The motion of tracer particles was captured by four 12-bit CCD cameras with a resolution of 1376 × 1040 pixels and a pixel pitch of 6.45 μm. Three cameras were arranged along different azimuthal directions in a horizontal plane while the fourth camera was positioned above the mid-camera in a vertical plane (Figure 2-12). Each camera was equipped with a Nikon 60 mm focal objective with numerical aperture f# = 11. Scheimpflug adapters were used on the three off-axis cameras to align the mid-plane of the measurement volume with the focal plane. The digital resolution is 15 pixels/mm and the average particle image density is approximately 0.04 particles per pixel (ppp). Image pre-processing, volume calibration, self-calibration, reconstruction, and three-dimensional cross-correlation based interrogation were performed in LaVision DaVis 8.1.5. The measurement volume was calibrated by scanning a plate with 9 × 10 dots through the volume in depth of 25 mm with steps of 5 mm. In each calibration plane, the relation between the physical coordinates and image coordinates is described by a 3rd-order polynomial fit. Linear interpolation is then used to find corresponding image coordinates at intermediate z locations. Image pre-processing with background intensity removal, particle intensity normalization and a Gaussian smooth with 3 × 3 kernel size was performed in order to improve the volume reconstruction process. Particle images were interrogated using windows of final size 32 × 32 × 32 voxels with an overlap factor of 50%. The resultant vector spacing is 1.0 mm (0.02 c) in each direction, forming a dataset of 87 × 68 × 24 velocity vectors in the measurement volume.

2.10 WROCLAW UNIVERSITY OF TECHNOLOGY

The Wroclaw University of Technology group (H. Kudela and T. Kozlowski) computed the translational-cases (pitch and surge) in 2D, using an in-house vortex-in-cell method for the incompressible Navier-Stokes equations. Casting the Navier-Stokes into stream-function-vorticity form, one obtains a Helmholz equation, which was solved using a viscous splitting algorithm [36], [37], [38]. First, the inviscid equation is solved:

$$\frac{\partial \omega}{\partial t} + u\frac{\partial \omega}{\partial x} + \upsilon\frac{\partial \omega}{\partial y} = 0 \qquad\qquad \text{(Eq. 2-2)}$$

and then, the viscous one (Stokes problem):

$$\frac{\partial \omega}{\partial t} = \nu\Delta\omega, \; \omega(\mathbf{x}, 0) = \omega, \omega|_{\partial\Omega} = \omega_b \qquad\qquad \text{(Eq. 2-3)}$$

From the inviscid equation, the vorticity is constant along characteristics, yielding a system of ordinary differential equations once the domain is discretized over a mesh. The mesh is used to solve the Poisson equation for stream function. Initial vorticity field is replaced by a discrete distribution of vortex particles that are placed in nodes of the grid, with a circulation assigned to each particle. Particles' circulation changes in time due to diffusion.

To simplify mesh definition, the flat-plate with rounded edges was replaced with an ellipse of fineness ratio 50.

2.11   UNIVERSITY OF BUFFALO

The University of Buffalo group (M.J. Ringuette, Z.R. Carr and A.C. DeVoria) experiments were done at the Vortex Dynamics & Bio-Inspired Propulsion Lab at the State University of New York at Buffalo [39], [40]. The facility is a 91 cm × 77 cm × 71 cm glass tank with a 50% by mass glycerin-water mixture; the density and viscosity are 1130.5 kg/m^3 and 5.78 × 10^{-3} Ns/m^2.

The configuration is a rectangular squared-edged flat-plate wing rotating from rest with a 45° incidence. Figure 2-13(a) shows the wing-aligned coordinates. The velocity program, driven by a motion controller, is a symmetric-in-time trapezoid (Figure 2-13(a) inset, green line); the position error is at most 0.03°. Acceleration/ deceleration occur over the first/last 10° of rotation; the total rotation is ϕ_{final} = 120°. For force measurements, the motion is smoothed during acceleration using a hyperbolic tangent curve (purple line) with the same average angular acceleration. While numerous variants were run, the parameter-set closest to the AVT-202 canonical rotational surge case has: AR = 2, t/c = 0.053, root cut-out 0.14 c, Re (based on span) of 10,000; this is for the PIV data set. Forces were taken with root cut-out of 0.30 c, Re 2000 − 10,000. Following Harbig *et al.* [45], we use a span-based Reynolds number, $Re_{span} = U_{tip}b/\nu$. Acceleration occurs over ~ 0.3 c at 75% span (0.25 b inboard of the tip).
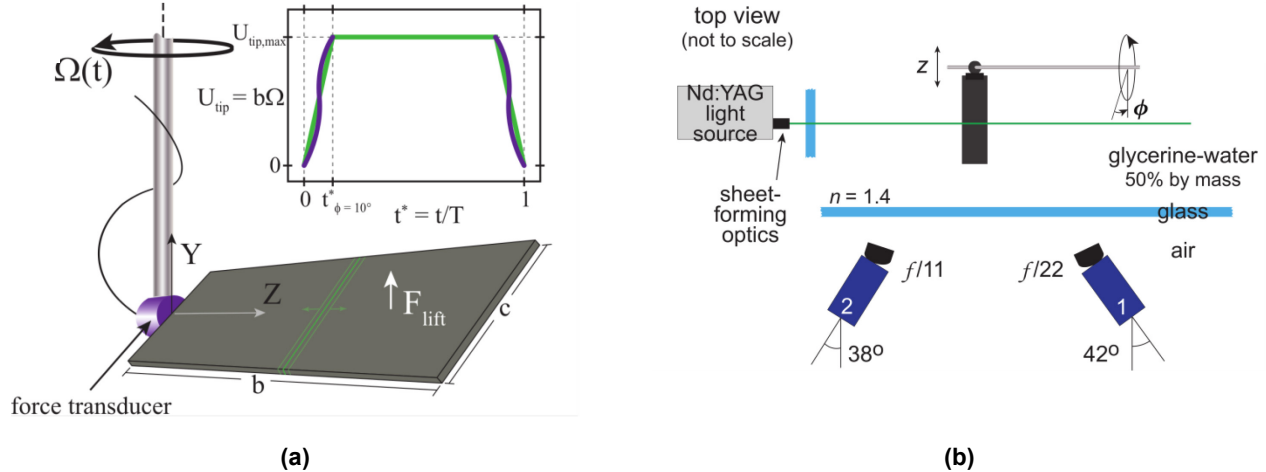
**Figure 2-13: (a) Wing Coordinates, Laser Sheet Orientation,
and Velocity Program; (b) S-DPIV Set-Up Schematic.**

The S-DPIV data are acquired via an approximately symmetrical angular camera arrangement (Figure 2-13(b)). Volumetric velocity fields are reconstructed from phase-locked, phase-averaged S-DPIV in multiple, closely-spaced constant-span planes. The wing is incrementally translated between runs along the span (z-direction), normal to the laser sheet. The out-of-plane spatial resolution is 0.06 c (0.08 c) for AR = 2 (AR = 4), with an in-plane resolution twice as fine. Angular positions are acquired at $\phi = 6°–120°$ with $\Delta\phi = 6°$. The in-plane velocity uncertainty is ~ 0.01 U_{tip}; it is about twice this out-of-plane. For AR = 2 and 4, the final velocity fields are obtained by phase averaging 5 and 7 fields, respectively. The force transducer is a submersible ATI Nano 17-IP68 attached at the wing base (Figure 2-13(a)). The sampling frequency is 1 kHz and 40 runs are averaged for each case. The uncertainty from static tests is 0.63% of the measurement for forces of $O(1)$ N. After averaging, low-pass filtering mitigates noise and mechanical vibrations.

2.12   UNIVERSITY OF CALGARY

The University of Calgary group (D. Rival and J. Kriegseis) performed experiments in a Rolling Hills free-surface water tunnel. Plunging and surging motions for an AR = 4 plate were controlled by a custom hexapod manipulator (see Figure 2-14). The flow was interrogated with three-dimensional particle-tracking velocimetry (3D-PTV). To obtain particle tracks, the tunnel was seeded with neutrally buoyant 100 μm silver-coated, hollow glass spheres with a Stokes number of Stk = 1.2 x 10^{-3}, and illuminated by a High-Intensity Discharge (HID) light source. A lens system (40 and 300 mm converging lenses) collimated the light to provide a measurement volume with a diameter of 100 mm. The plates were painted black to prevent light scattering. Raw images were recorded with four pco.edge sCMOS cameras (chip size 2560 x 2160 pixels, maximal resolution of 2560 x 1280 pixels at 165 frames per second). Direct force measurements were recorded by means of an ATI Gamma [23] six-component force/moment sensor, which was located between the base of the hexapod and the sting holding the plate. The plate had a chord length of $c = 50$ mm, a span of 4 $c = 200$ mm and t/c = 6%. Based on the chord length and free stream velocity U or the final towing speed h(dot) = 0.1 m/s (depending on the case), the Reynolds number was set to Re = 5000. Note that the coordinates' point of origin is placed at the intersection of the leading edge and the tip edge. To identify the influence of initial conditions on vortex formation and orientation, as well as the circulation and overall force history, different plate kinematics were applied to the AR = 4 flat plate.
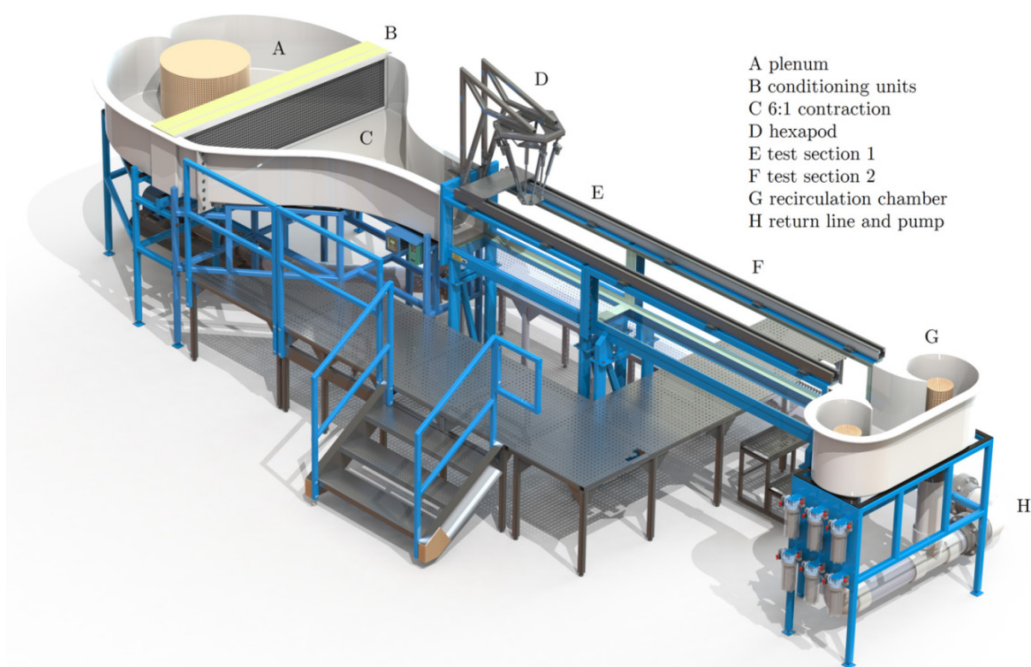
A plenum
B conditioning units
C 6:1 contraction
D hexapod
E test section 1
F test section 2
G recirculation chamber
H return line and pump

Figure 2-14: University of Calgary Free-Surface Water Tunnel and Hexapod Rig.

2.13   UNIVERSITY OF MARYLAND

The Maryland group (A. Jones, P. Mancini and F. Manar) performed experiments in the 7 m x 1.5 m x 1 m tow tank (Figure 2-15) at the University of Maryland, and in the AFRL water tunnel (the latter is discussed above).

(a)   (b)
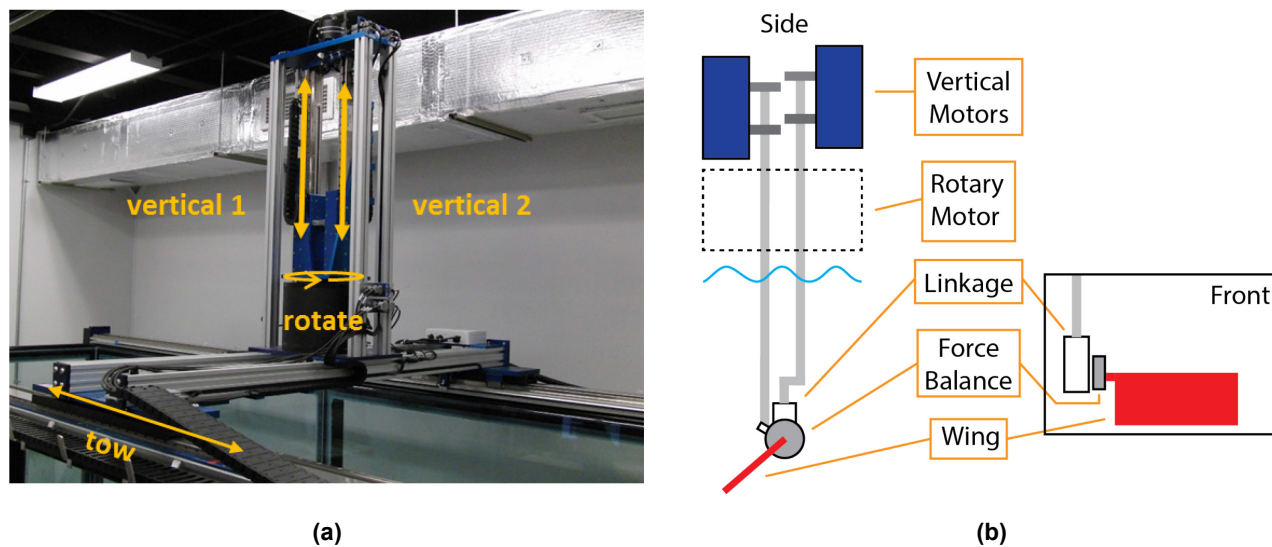
**Figure 2-15: University of Maryland Towing Tank: Photograph of Electric Motors
Atop of Tank (a) and Schematic of Rotating/Pitching Wing Actuation (b).**

The towing tank is equipped with a 4-axis motion control. The motor assembly, shown in Figure 2-15(a), is mounted on the towing carriage, and contains two brushless linear motors, a direct-drive brushless rotary stage, model supports, and a slip ring to transfer power and other signals to/from the equipment on the rotary stage. Vertical plunge (± 49 cm) and pitch (± 90 deg.) are driven by the two linear motors and a custom-designed Hoeken linkage. Continuous rotation is provided by the rotary stage. Carriage translation (7 m) is directly driven by a pair of brushless linear motors. All stages are equipped with optical encoders, and the entire traverse system is controlled using a multi-axis Galil motion controller to within 0.1 mm. Pitch motion is accurate to within 0.1 degrees. After each test, the motion of the fluid was observed to come to a standstill after about 3 minutes. To ensure absolute quiescent conditions, 5 minutes were allowed to pass between each test run.

An ATI Mini40 6-axis force/torque transducer with force resolution of 0.01 N and a torque resolution of 0.0001 Nm was used for direct loads measurement. The sampling rate was 1000 Hz. Each case was run 5 times, starting from different locations in the tank. Starting at a slightly different location served to help average out noise from any bumps in the carriage travel. Results were then averaged. The load cell was fixed to the pitch linkage with a 3D-printed adapter plate. Another 3D-printed adapter is used to fix the wing directly to the force balance; the force balance therefore collected data directly in the wing frame. To isolate only the fluid loads, the contributions from gravity and buoyancy were removed from the measured force. In the surge cases, the average force over the first second was taken as the net gravity and buoyancy force and subtracted from the measurement. For the pitch cases, the tare process is slightly trickier because of the changing direction of gravity in the force balance frame. To remedy this, forces were taken with a static wing at angles of attack ranging from -60 to 60 degrees in 15 degree increments. These static forces were fit with a 3rd-degree polynomial in angle of attack, which was used to tare the gravity and buoyancy forces at any angle of attack. Inertial loads were measured in air and the magnitude of the resulting force was found to be negligible.

The forces were smoothed in time with MATLAB's 'smooth' function using the "lowess" option with a width set to 0.5 chords of travel at the final velocity, which corresponds to 0.25 seconds in real time. The "lowess" option creates a least squares quadratic fit over the smoothing window for each point in the original data set and evaluates the resulting quadratic polynomial at the point in question. This method does a good job of rejecting noise without introducing a phase shift, while still accurately capturing the magnitude of peaks in the data.

For all cases in this facility, the wing was an AR = 2 flat plate with a chord of 100 mm and slightly rounded edges, and thickness of 0.08 inches. For the rotation case, the root cut-out was 0.5 c, and the angular velocity was set to achieve the same velocity as the translating case at 75% of the tip radius from the axis of rotation. Put another way, the radius of 1.875 chords from the axis of rotation was used to compute the Reynolds number and to normalize the forces. The surge cases were run at a fixed incidence of 45 degrees, and the pitch cases were pitched from 0 degrees to 45 degrees.

Both translation and rotation velocity profiles were computed using the "Eldredge function" [7] with a smoothing parameter, a, of 24. The pitch kinematics used the Eldredge function as a position profile. The fast pitching case used a smoothing parameter of 15, and the slow case used 4. For rotational pitch, the wing was set to 0 degrees and then accelerated to the final velocity and moved through 5 chords of travel before beginning the pitch motion.

2.14 UNIVERSITY OF MICHIGAN

The Michigan group (H-T. Yu and L. Bernal) performed experiments in a free-surface water tunnel at the Department of Aerospace Engineering (Figure 2-16). The tests section is 0.6 cm x 0.6 cm x 2 m. The free-stream velocity is controlled using an AC induction motor, which is calibrated as a function of test section water

depth using PIV. The flow speed ranges from 5 cm/s to 40 cm/s and the free stream turbulence intensity is below 1%. The model wings were made of Plexiglas®, c = 2", t = 0.125", for t/c = 0.0625, with all edges rounded. They are immersed in water for a 2-chord span, resulting in physical AR = 2 and effective AR = 4, taking the water surface as a symmetry plane.
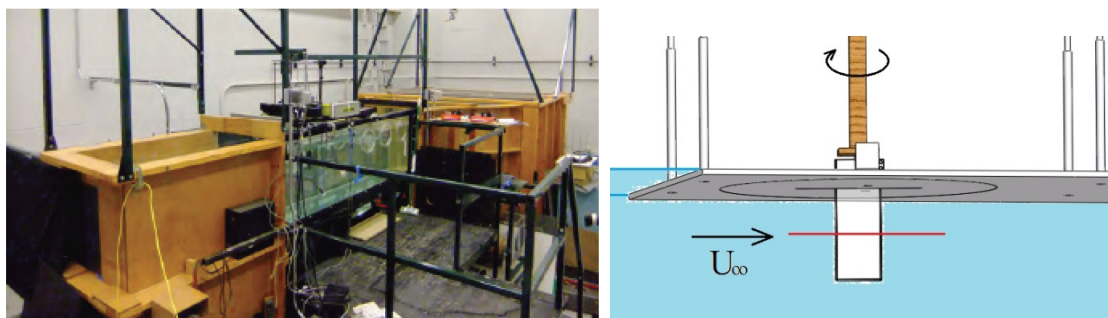
Figure 2-16: University of Michigan, Department of Aerospace Engineering Low-Turbulence Free-Surface Water Tunnel. Left: photograph of facility; Right: schematic of AR = 2 plate suspended vertically underneath a free-surface skimmer plate.

The wing motion is the usual linear pitch ramp from 0° to 45° with Eldredge [7] smoothing at the start and the end of the ramp. Several values of the smoothing parameter were used [41]. A Velmex Rotary Table model B4832TS and stepper motor RK266-03 are used for the wing motion. The kinematics is discretized with 13 points at every smoothed region. For all measurements the motion is repeated 60 times, and phase-averaged. For details, see Yu *et al*. [42] and Yu and Bernal [43].

Forces are measured via an ATI Nano-43 load cell [23]. The sensor center is on the pitch axis and the sensor axes are aligned with the chord direction, plate normal direction and span direction, respectively. The sensor's maximum calibrated load is 18 N, and the resolution is 1/256 N, in all three axes. Both the force sensor and the rotary table are located above the water surface. The wings are attached to the tool side of the sensor with an aluminum adapter designed to minimize the mass of the model. Data processing includes low-pass filter and tare. The low-pass filter is a zero-phase first-order two-pass Butterworth, with cut-off frequency was determined by Fourier analysis of the motion acceleration to retain 90% of motion spectral content. A dynamic tare consisted of repeating the exact same motion in both water and air, and subtracting the results. No static calibration was needed because of the small mass of the model and the excellent alignment of the span axis with the vertical direction.

Flow visualization was conducted using a dye rake (7 probes with 1" spacing), two syringe pumps, and two different color dyes (i.e., blue and red). The injection rake was placed at 50 % of wing span. Since the density of the dyes (ESCO Foods) is 1012 kg/m^3, they were mixed with alcohol to match the water density, 998 kg/m^3. Images were recorded using Nikon D3100 camera at a frame rate of 30 Hz.

Conventional 2D PIV and lens-shifted Stereo PIV were used. The lens-shifted Stereo PIV system was developed specifically for this research [41]. In a typical test, the magnification was 13 pix/mm and the particle displacement between images approximately 8 pix. PIV images were processed using in-house developed MATLAB software, which uses a cross-correlation algorithm to determine the particle displacement with sub-pixel resolution, and a two-pass algorithm.

Chapter 3 – THE CANONICAL CASES

3.1 AERODYNAMIC FORCE HISTORIES

We begin with a plot of lift coefficient histories for the eight cases, compared side-by-side as translation and rotation, plotted with the same time-base and axes definitions. The "fast" cases are plotted in two ranges of abscissa: one to emphasize the response when acceleration is non-zero, and a broader range (15 chords-traveled) to show long-term settling. The "slow" cases are all plotted with respect to 5 chords traveled. To reiterate, the rotations are with an AR = 2 plate with (primarily) 0.5 c root cut-out, while translations are with an AR = 4 plate. "Fast" pitch or surge has the acceleratory part occurring in a ramp linear with wall-clock time over 1 c of travel, while the "slow" cases do so over 6 c. The linear ramp is smoothed at its endpoints. Pitch motions begin with the plate at zero incidence and conclude with the plate at 45 degrees. Surge motions hold the plate at 45 degrees. Lift data are presented in two sequences; the first zooms in to early-time, emphasizing loads-history during the accelerated portion of the motion, and immediately thereafter. The second covers the entire recording-time, showing the long relaxation-transients after cessation of acceleration, in going towards the "steady-state" (or bluff-body shedding) response.

We first note the perhaps surprisingly good agreement between the various data sets, for each respective case. Occasionally there is an outlier, likely due to balance signal-to-noise reasons, tare-procedure and so forth (repeating a litany of possible experimental foibles is of nugatory value); often multiple curves mutually align, with one deviating, especially during the accelerated portion of the motion, but then later coming into mutual consonance. Figure 3-1 (translational case, left-hand side) is a typical case. This multi-way validation is encouraging, for it unifies the various data sets despite rather stark differences in types of model installation, blockage, Reynolds number and so forth. In particular, in some cases the plate is suspended vertically in a water tunnel or tow tank, with the load-cell atop of the water line, and the "tip" near the load-cell either piercing the free-surface or terminated with a splitter plate. In other cases the plate is mounted horizontally in the test section, supported by a sting aft of the plate, or midway along its pressure-side. The different kinds of blockage and physical obtrusions appear to not have any discernible major effect.
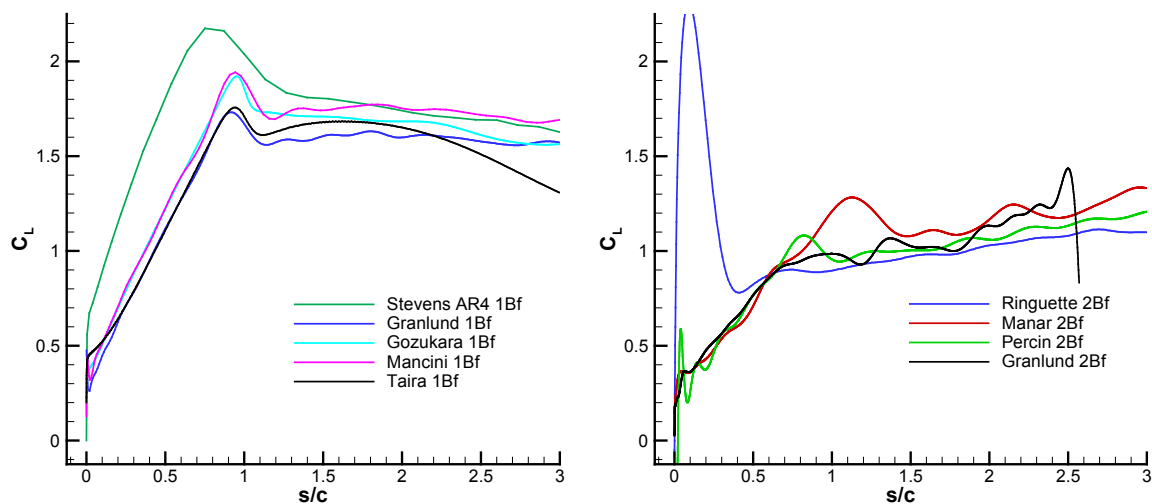
Figure 3-1: CL for the Fast Surging Cases. Translational (left) and rotational (right). Time-history through 5 chords of motion is shown. Note that data by Ringuette (right) is for a faster acceleration.

Next, we note the similarity in lift history reading across the row of each figure in this section – that is, comparing the translational and the rotational case. Members of each row are mutually more similar, than those of other figures. More precisely, translational pitch and rotational pitch resemble each other more, than do say translational pitch and translational surge. While the quantitative magnitude of force coefficients for rotation, and hence quantitative comparison with translation, depends on the choice of spanwise reference station in the defining an aerodynamic coefficient, the qualitative trends are unmistakable.
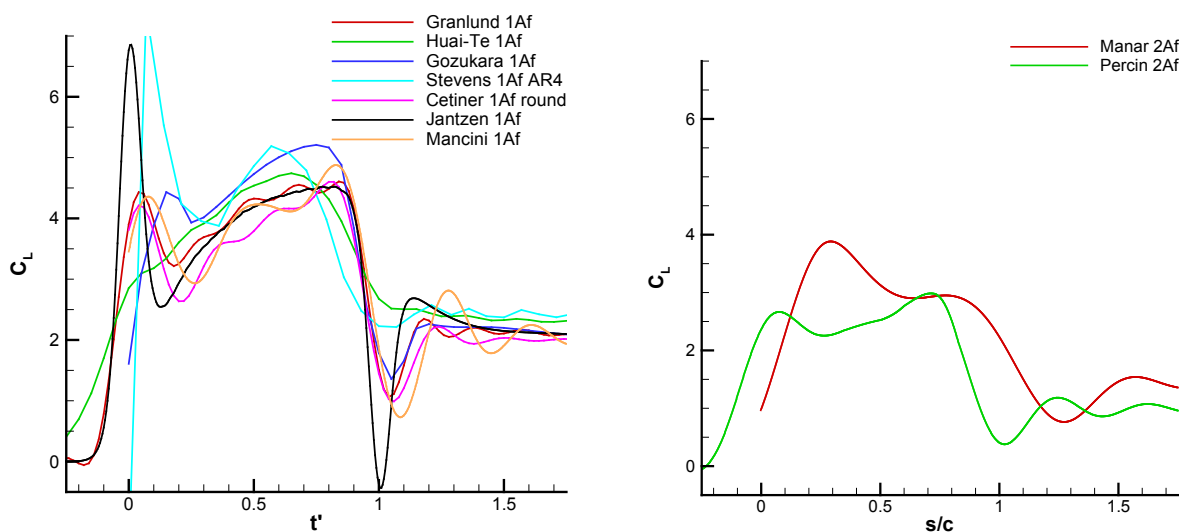
Figure 3-2: CL for the Fast Pitching Cases (LE Pivot). Translational (left) and rotational (right).
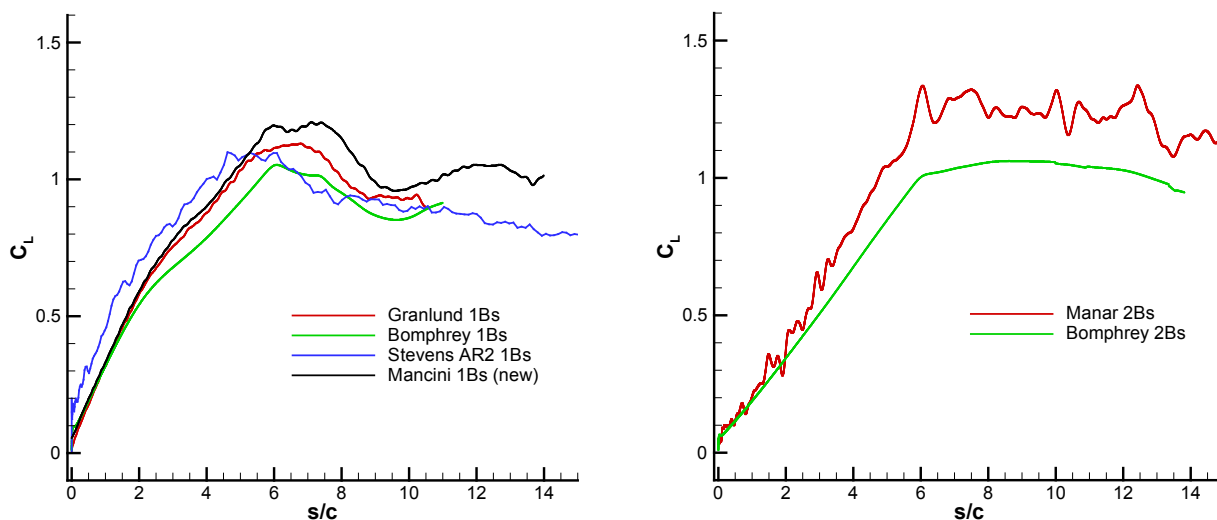
Figure 3-3: CL for the Slow Surging Cases. Translational (left) and rotational (right).
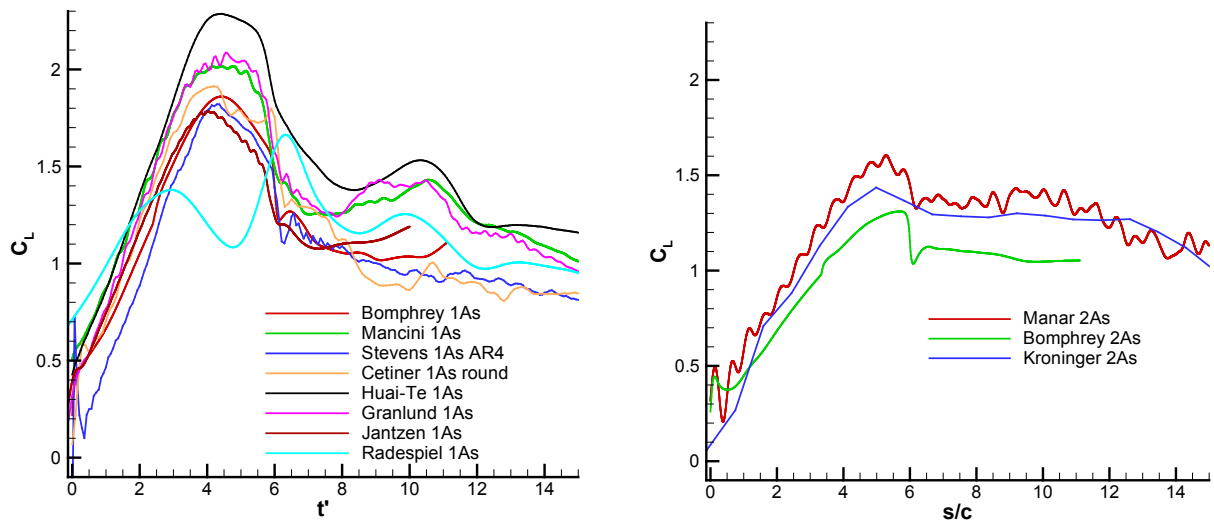
Figure 3-4: CL for the Slow Pitching Cases (LE Pivot). Translational (left) and rotational (right).
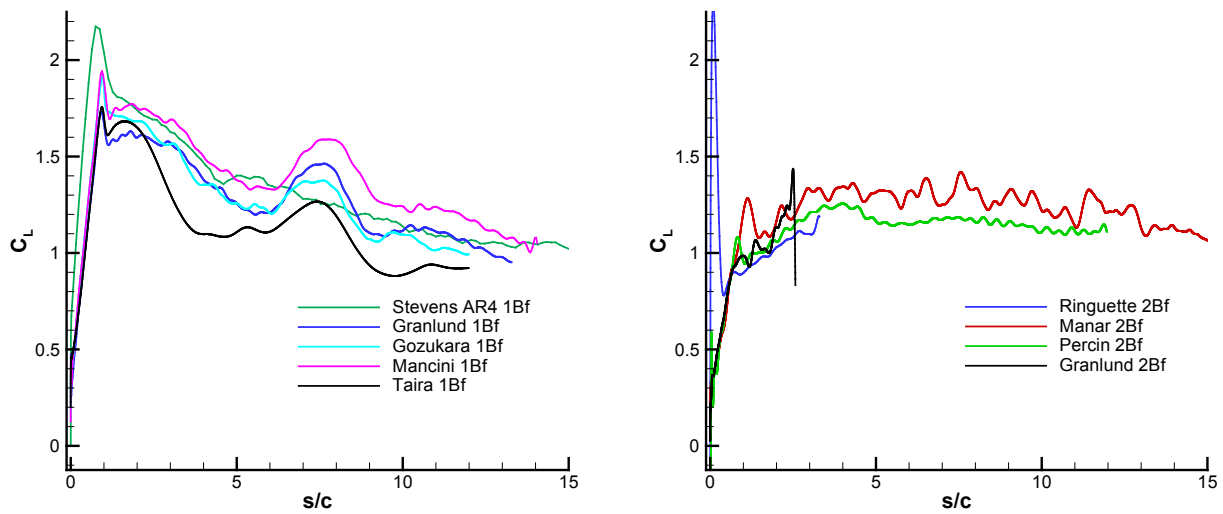
Figure 3-5: Long-Term History of CL for Fast Surging Cases. Translation (left) and rotation (right).
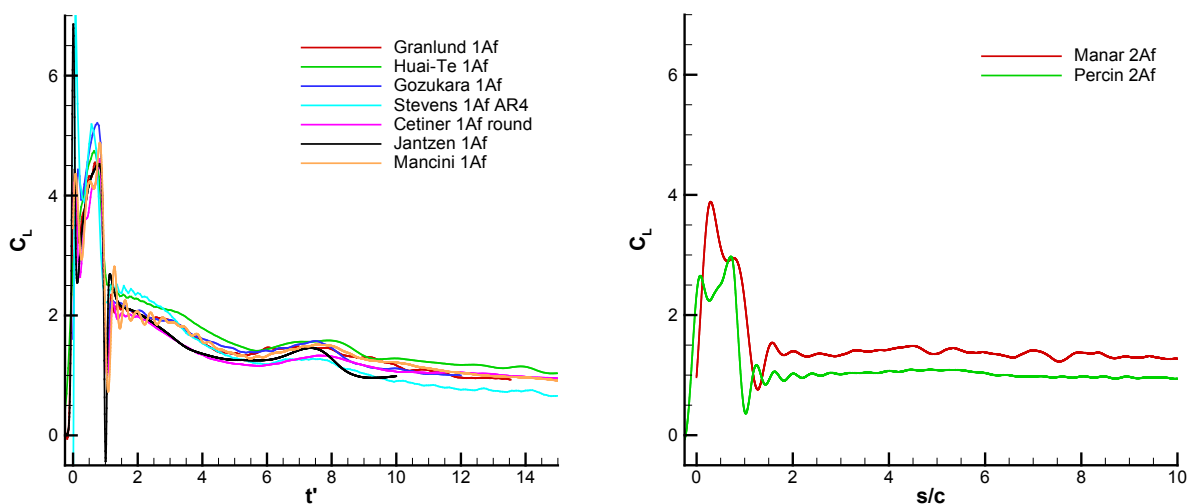
Figure 3-6: Long-Term History of CL for Fast Pitching Cases. Translation (left) and Rotation (right).

The long-term trend in all translational cases is evidently that it takes at least 15 chords-traveled for the effects of acceleration to completely dissipate, and for the lift history to asymptote to the "bluff body shedding" or quasi-steady-state. This is true whether the acceleration was "fast" (1 c) or "slow" (6 c). The rotational cases are different: there the lift response reaches a more or less constant value after 5 c of travel, or less. Instead of a long and slow relaxation, there may be a rise in lift after the accelerated portion of the motion is over, followed by a long steady period. In some cases, the wing revolves through its own way, and depending on the blockage of the installation (distance between wing tips and walls of the tank [44]), lift history declines slightly after a full revolution has been completed.

We next turn to the drag histories, this time for all 8 cases plotted across 15 convective times, again with translation on the left-hand side, and rotation on the right-hand side.
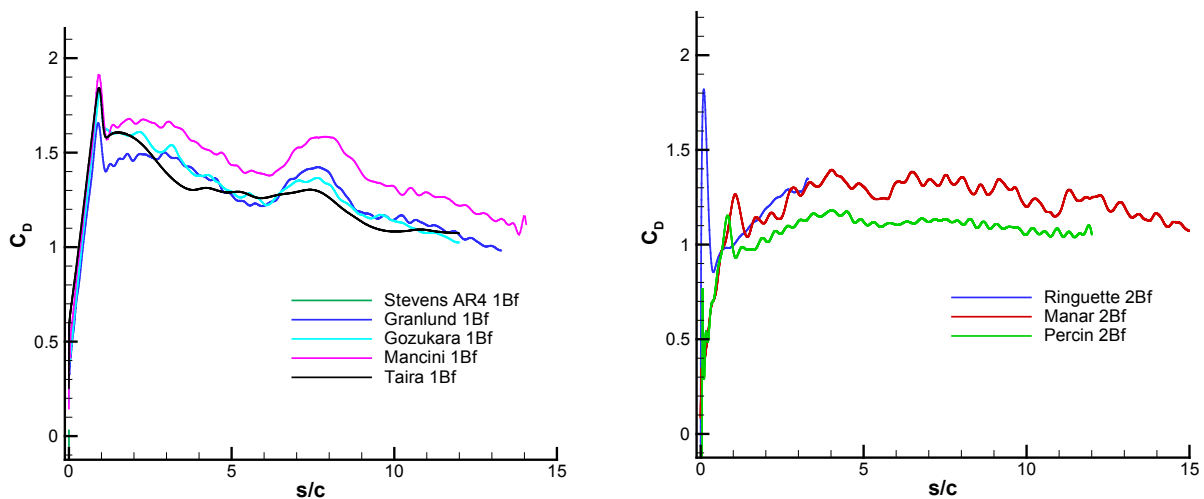
Figure 3-7: CD for the Fast Surging Cases. Translational (left) and rotational (right).
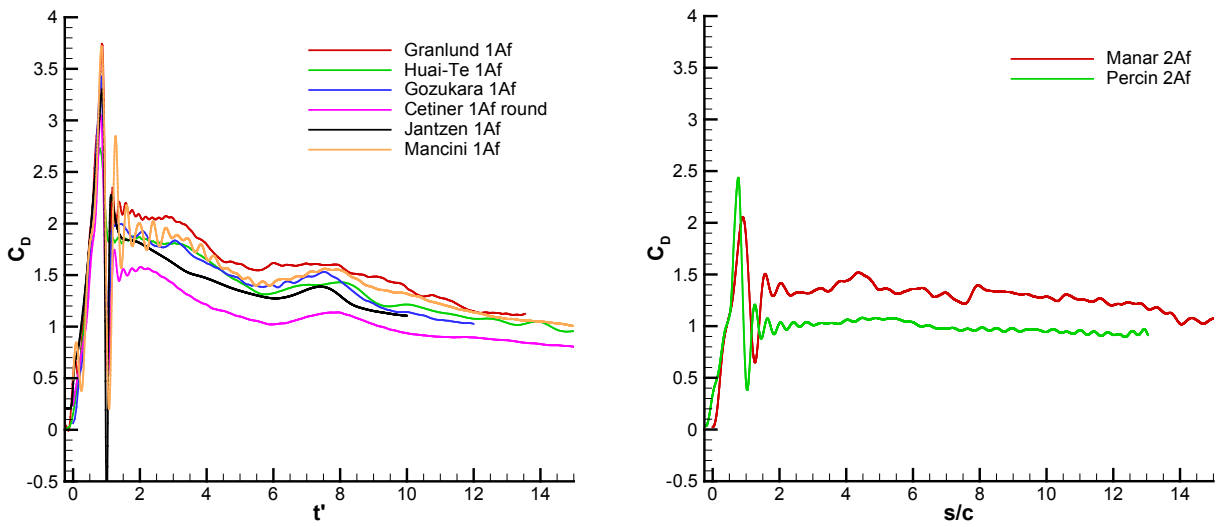
Figure 3-8: CD for the Fast Pitching Cases. Translational (left) and rotational (right).
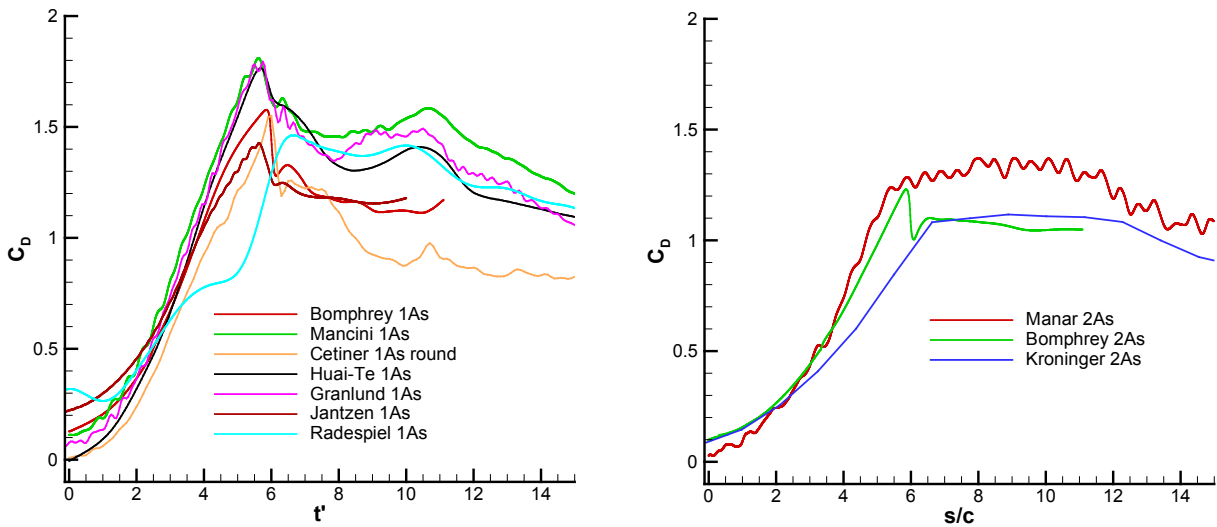
Figure 3-9: CD for the Slow Pitching Cases. Translational (left) and rotational (right).
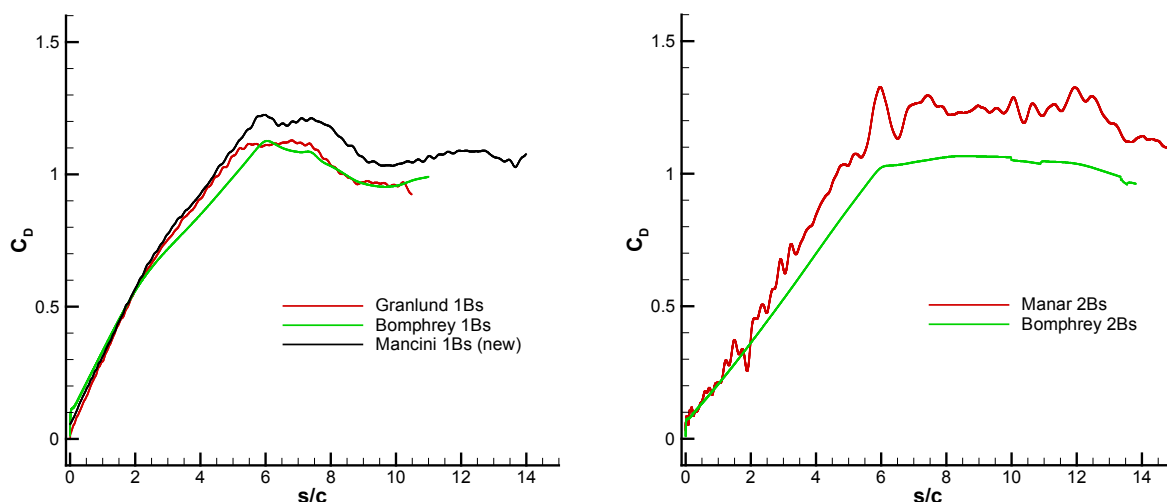
Figure 3-10: CD for the Slow Surging Cases. Translational (left) and rotational (right).

Importantly, for the surging cases (rotational or translational, fast or slow), the lift and drag histories resemble each other very closely. This is not surprising, as the net aerodynamic force is essentially plate-normal, and the plate is at 45 degrees incidence. For the pitching cases the situation is rather different; lift tends to be larger than pitch during the accelerated portion of the motion, or in other words, L/D > 1. Thus pitch has a double aerodynamic benefit over surge: it produces a net larger force, and a net higher L/D.

3.2 LEADING EDGE AND TRAILING EDGE VORTEX STRENGTHS AND TRAJECTORIES

Figure 3-11 shows the LEV circulations measured by a variety of groups for the fast pitch and surge cases. Before discussing this result in detail the following should be noted:

- The methods of determination of vortex strengths vary widely between groups and are subject to considerable error. In the slow case the LEV is not very distinct and this has made it impossible to distinguish any trends in circulation growth.

- Sometimes, neighboring secondary vortices become included in the calculation of LEV strength – this can cause sudden steps in the circulation distribution.

- The circulation data is non-dimensionalised by a Γ_∞ which is equivalent to $c_L = 2\pi\alpha$, with $\alpha = 45°$. Thus, the non-dimensional circulation shows how the LEV strength compares to an assumed steady-state thin airfoil theory bound circulation.

- The data are compared to a Wagner function which also asymptotes at a non-dimensional circulation of unity.
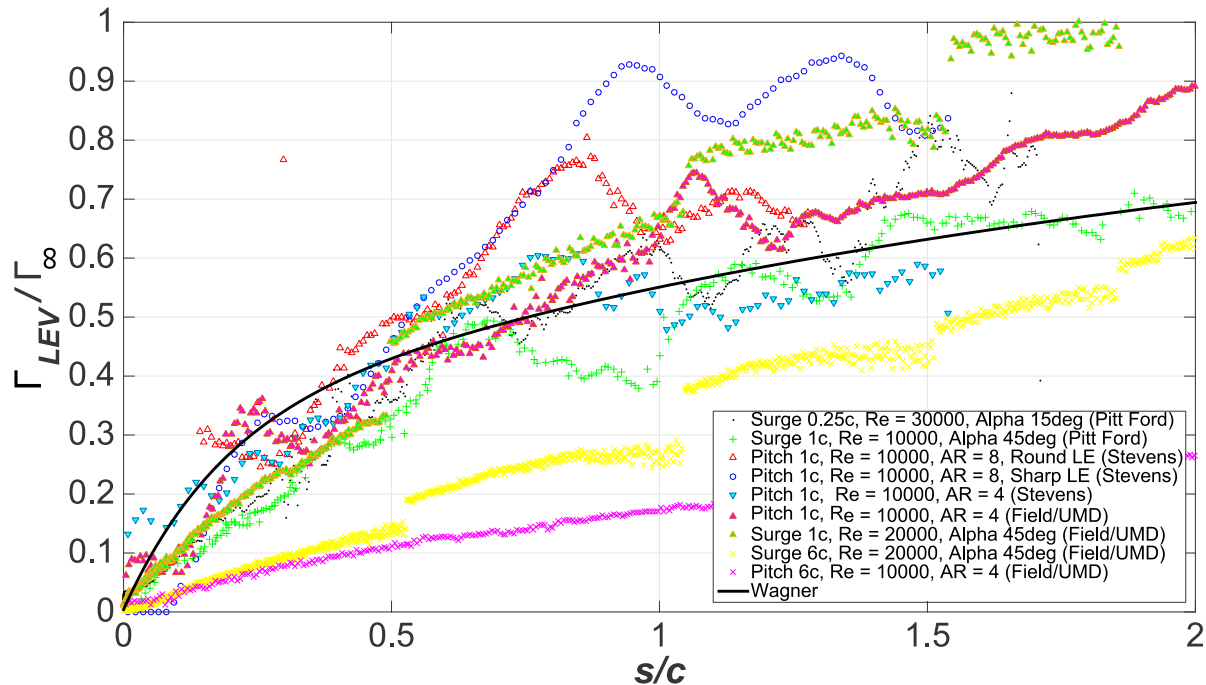
Figure 3-11: Collection of Normalized LEV Circulation Histories from Various AVT-202 Contributors, for Translational Pitch and Surge Cases; Compared with Wagner's Theoretical Curve [53].

The difficulties in vortex strength determination are clearly reflected in the data. Overall the scatter between different groups is far larger than the differences between different cases. Also, the scatter becomes noticeably larger with time. This is a reflection of the break-up of the initially coherent LEV and the appearance of secondary vortices. Nevertheless, ignoring some obvious outliers, there are some clear trends.

Somewhat surprisingly, there are no obvious differences between pitch and surge. As a rough approximation all data follows the Wagner function reasonably well. During the early part of the motion the Wagner function slightly over-predicts vortex strength. This can be interpreted as a reflection of the fact that during this part of the motion the wing is not yet at either the final velocity or angle of attack. Thus one might expect that the equivalent 'asymptotic Wagner value' to be lower.

To account for the reduced strength of the vortices early in the cycle, Figure 3-12 shows the data for the fast pitch and surge cases with a Wagner function that has been modified for $s/c < 1$ by the equivalent angle of attack or free stream velocity (or, in other words, by multiplying the original Wagner function with a linear ramp). It is debatable whether this fit is better than the original unmodified Wagner function, although the actual shape of the vortex growth is somewhat better reflected. Either way, given the large amount of scatter in the experimentally determined LEV circulations it is proposed to adopt the Wagner function (modified or unmodified) for the low-order model calculations. This is certainly the only viable route for the calculation of the vortex growth term as the experimentally data are too noisy to allow a meaningful calculation of $\dot{\Gamma}$.
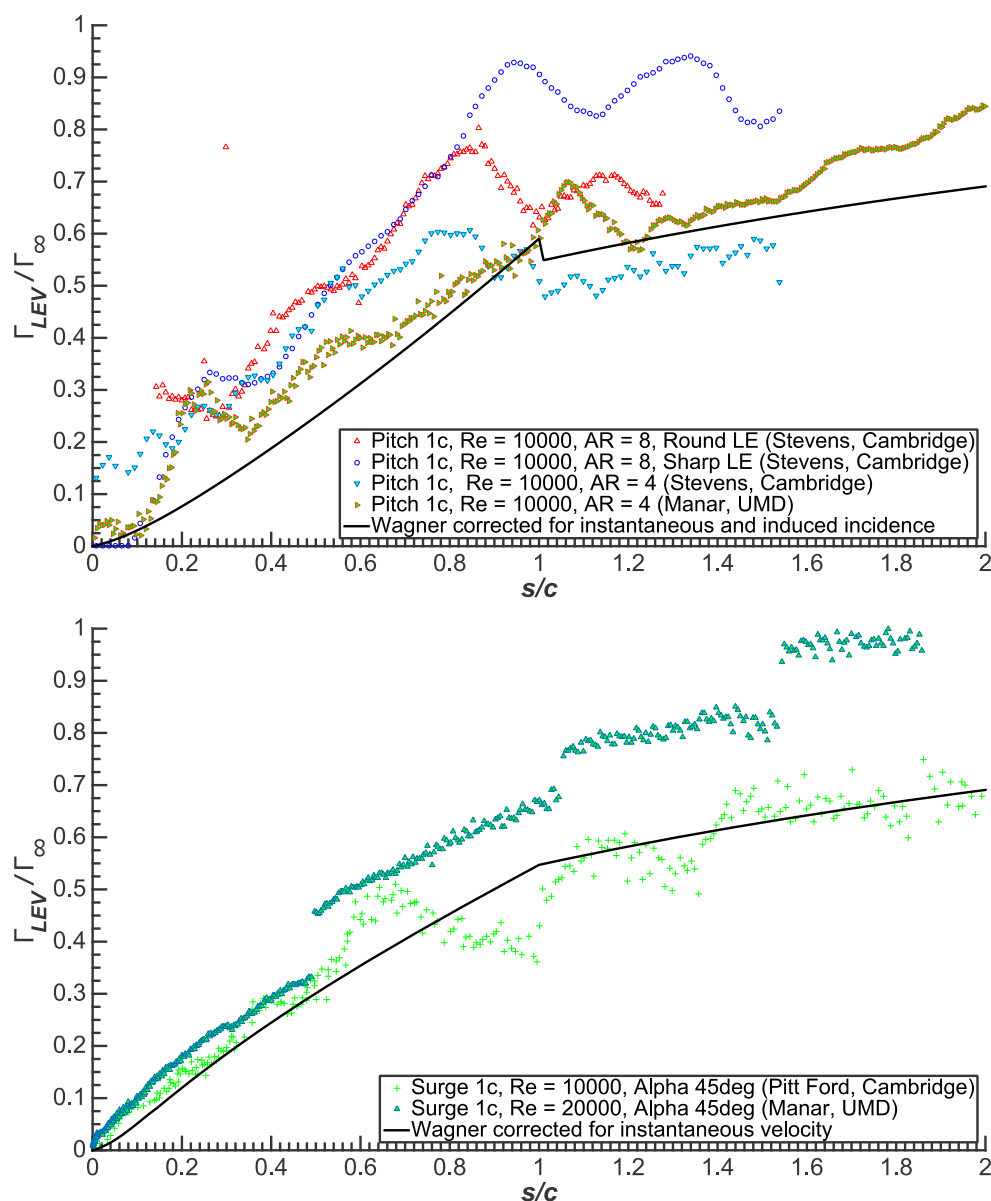
Figure 3-12: Normalized LEV Circulation Compared to 'Modified' Wagner Function for Pitch (Top) and Surge (Bottom). Note the small kink in 'Wagner' circulation in the pitch case as a result of the induced angle of attack during the pitching motion.

Similar difficulties with the vortex detection schemes affected the determination of vortex trajectories. Figure 3-13 shows the distance (in chord-lengths) between the detected LEV center and the plate leading edge for the fast pitch case through the first three chord lengths of motion. Given the measurement difficulties it is impressive how well the various datasets collapse. Overall the relative speed between the LEV and the plate is approximately $\frac{1}{3}U_\infty$.
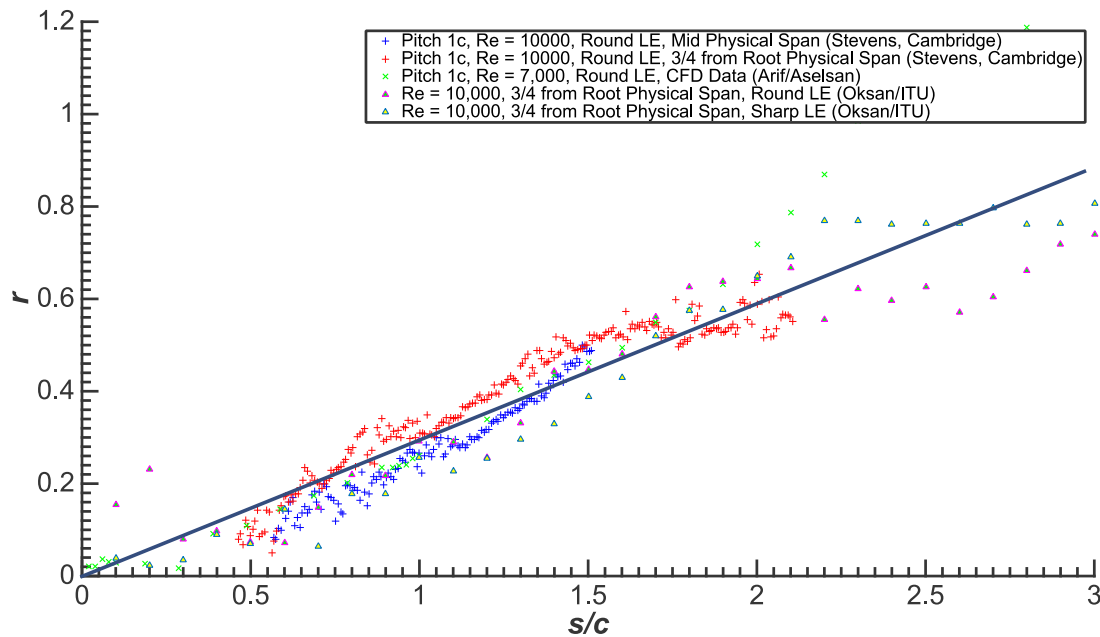
Figure 3-13: LEV Distance from Plate Leading Edge for the Fast Translational Pitch Case.

Figure 3-14 compares leading and trailing edge vortex trajectory data for the translational pitch and surge cases, as measured in the Cambridge University towing tank. The LEV trajectory is again very similar and follows the same trend (of $\frac{1}{3}U_\infty$) while there are clear differences in the TEV behavior. It appears that the TEV formation is delayed in the pitch case: it cannot be detected until the wing has travelled almost half a chord length. Thereafter the TEV moves away from the wing faster than in the surge case (although it has to be kept in mind that the surging wing has not yet reached full speed at this point). Ultimately however, both TEV trends converge onto the same line which suggests that the TEV reaches something around 80% of U_∞ by the end of the acceleration period. Thus, it can be suggested that a good model for the *relative* velocity between the TEV and the LEV during the unsteady part of the motion is 50% of U_∞ for the pitching wing and 0.3 U_∞ for the surging wing. Thereafter 0.3 U_∞ appears to fit both cases reasonably well.
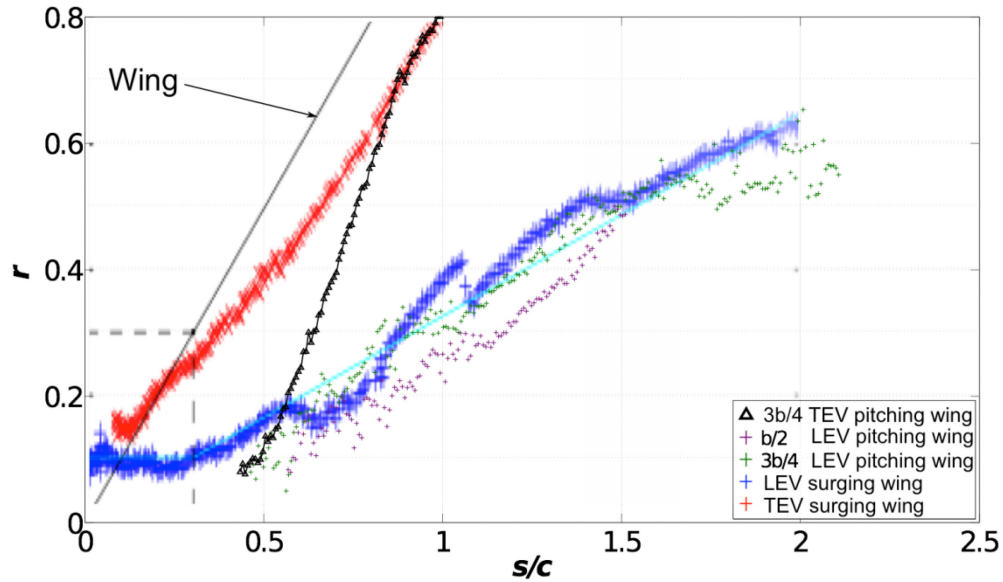
**Figure 3-14: LEV and TEV Distance from Leading Edge for Fast Translational
Surge and Pitch Case (Data from Cambridge University Group). 'Wing'
indicates the trajectory of an object moving away at U_∞.**

3.3   EVOLUTION OF VELOCITY AND VORTICITY FIELDS

Because a low-order model is used to estimate aerodynamic loads, and not a whole flowfield integration [8], velocity field data is more for illustrative purposes, than for quantitative calculation. The idea is to qualitatively relate LEV, TEV and tip vortex development to the history of lift and drag. In some cases we compare qualitative and quantitative visualization; that is, dye concentration vs. measured or computed vorticity.

3.3.1   Translational Pitch and Surge

LEV and Tip Vortex (TV) development during pitching is given in Figure 3-15(a), (c), (e) and (g); the left-half of the page is for the fast case, and the right-half is for the slow case.
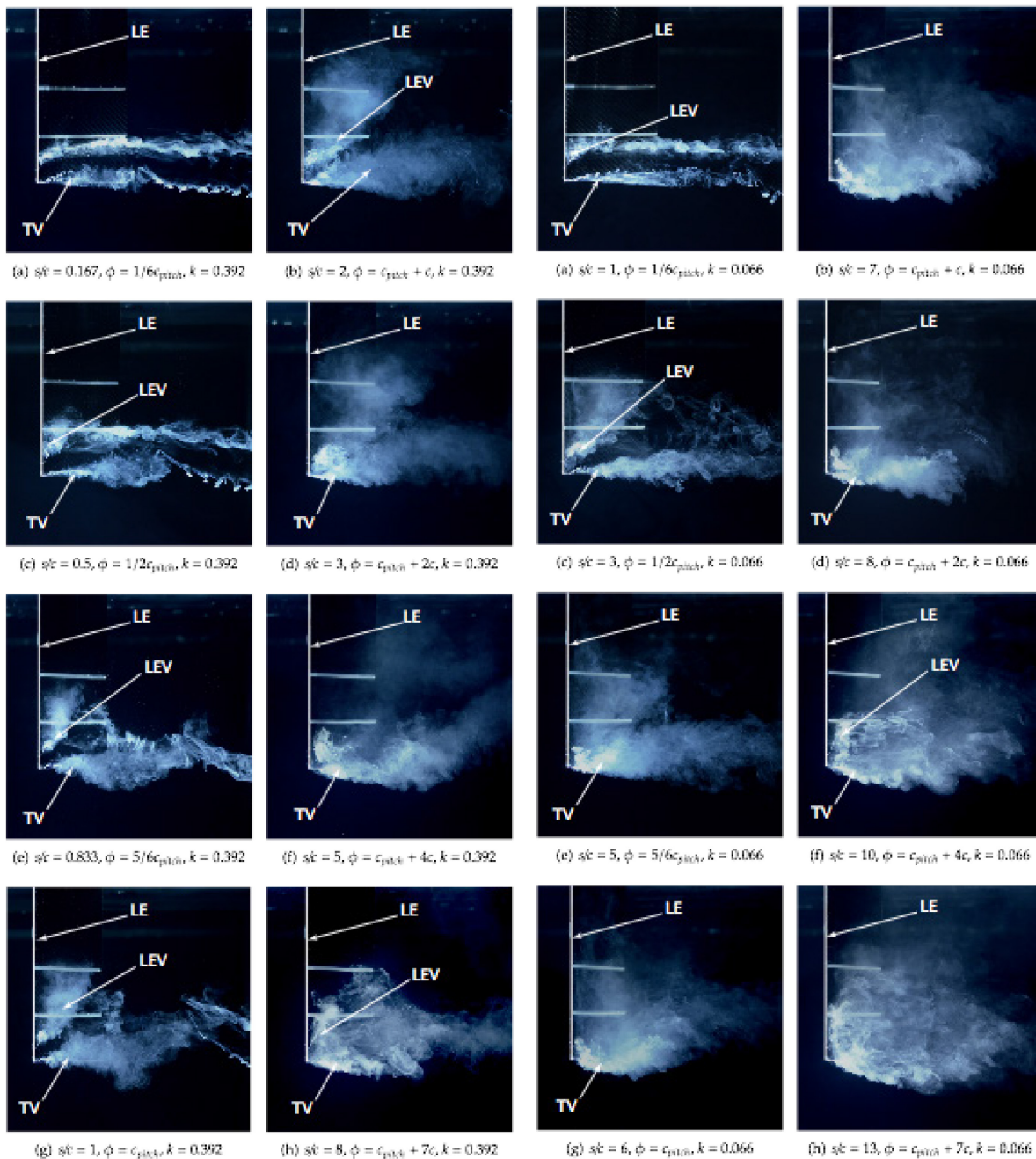
Figure 3-15: Case 1a, Translational Pitch, LEV/TV Interaction Flow Visualization; Eight Images on Left are for the Fast Case (1 chord pitch), and Eight Images on the Right are for the Slow Case (6 chords pitch). Instances of chords-traveled as marked, progressing sequentially for the fast case down the first column of the figure, then the second column; and for the slow case down the third column of the figure, and then down the fourth column.

We first consider the pitching fast-case. Initially, the flow is attached with little discernible tip influence at s/c = 0.167. By s/c = 0.5 a clear and distinct LEV and TV are beginning to form, but with no obvious interaction.

As the incidence angle increases (s/c = 0.833 and s/c = 1) the TV grows concurrently with the LEV. The angle between the distinct LEV and TV from the LE and tip apex is approximately 45°. The downwash from each vortex will superimpose here, and this mechanism may point towards a physical reason as to why the LEV remains more coherent closer to the wing tip. During the translation part of the motion (Figure 3-15(b), (d), (f) and (h)), the dye disperses as the LEV and TV grow. By s/c = 5, the dye from the LE is fully entrained into the tip vortex and by s/c = 8 we see the beginning of the reformation of an LEV type structure in the outer span region of the wing, albeit a much less defined structure than that which manifested while pitching occurs.

Turning to the slow pitching case (right-hand side of Figure 3-15), initially the flow evinces small and well-defined TV and LEV. By s/c = 3, the TV has developed but remains coherent, whereas the LEV is weak and only has a coherent form close to the tip. At s/c = 5 the LEV has dispersed, and by s/c = 6, the tip vortex is the dominant structure. After cessation of pitching motion, the flow is largely separated, with the exception of the reformation of a small LEV-type structure at s/c = 10. Comparing again with the lift coefficient history, we gain some physical insight and propose that the presence of a weak LEV/weak circulatory flow is intrinsically linked to an increase in streamline curvature, and is therefore responsible for an increase in the force.

We now turn to an alternative presentation of the fast pitching case, as an isometric view of sectional visualizations. Fluorescent rhodamine dye injection illuminated by a planar light sheet is compared with black and white rendition of computed vorticity contours in Figure 3-16. Evidently a "suitable" value of normalized out-of-plane vorticity value renders the quantitative vorticity information looking very similar to the qualitative dye-concentration information.
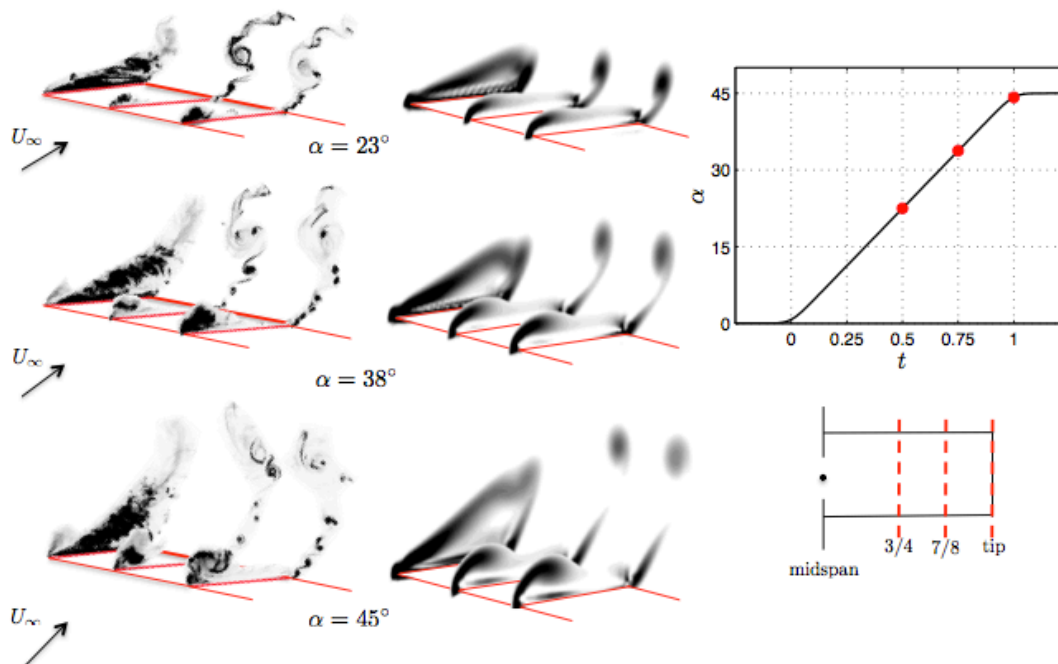
Figure 3-16: Juxtaposition of Flow Visualization by Planar Laser Illumination of Fluorescent Dye in a Water Tunnel at Re = 20,000 (Left Column) and Black and White Rendition of Spanwise Vorticity Contours from Direct Numerical Simulation at Re = 300 (Middle Column) for the Fast Translational Pitching Case. Instances of flow evolution along the motion-history as marked, visualized at the 3/4 span, 7/8 span and tip locations.

Figure 3-17 compares the fast pitch, fast surge, slow pitch and slow surge at instances of chords-traveled of 0.5, 1.0, 1.5, 2.5, 3.0, 5.5 and 8.0. These are 2D PIV images at the ¾-span location. Evidently, the fast cases evince a more compact and more coherent LEV. The fast pitch and fast surge have similar LEV developments. Their respective TEVs differ in that the pitching-case has fully-developed free-stream speed at all times, whence the TEV convects rapidly from the plate's TE, whereas in the surging case the plate accelerates away from its TEV in accordance with its surge history; that is, the TEV is essentially stationary in the lab-frame. The slow pitching case has a delayed LEV development, with a reasonably coherent LEV present even at s/c = 3, whereas in both fast cases the LEV has lifted off and evidently saturated. However, at s/c = 5.5 in the fast cases a second LEV appears to be forming, whereas in the slow pitch the initial LEV still lingers more or less. Unfortunately only a limited data set is available for the slow surge (fourth column of Figure 3-17). At s/c = 1.0, the overall flow topology of the slow surge much resembles that of the fast surge, albeit the LEV strength is evidently reduced for the slow case. The comparability persists through s/c = 2.5, which is the last frame for the slow surging case for which data are available. In short, the outlier in terms of gross flowfield features is the slow pitching case.

| *Fast Pitch* | *Fast Surge* | *Slow Pitch* | *Slow Surge* |

s/c = 3.0

s/c = 5.5

s/c = 8.0
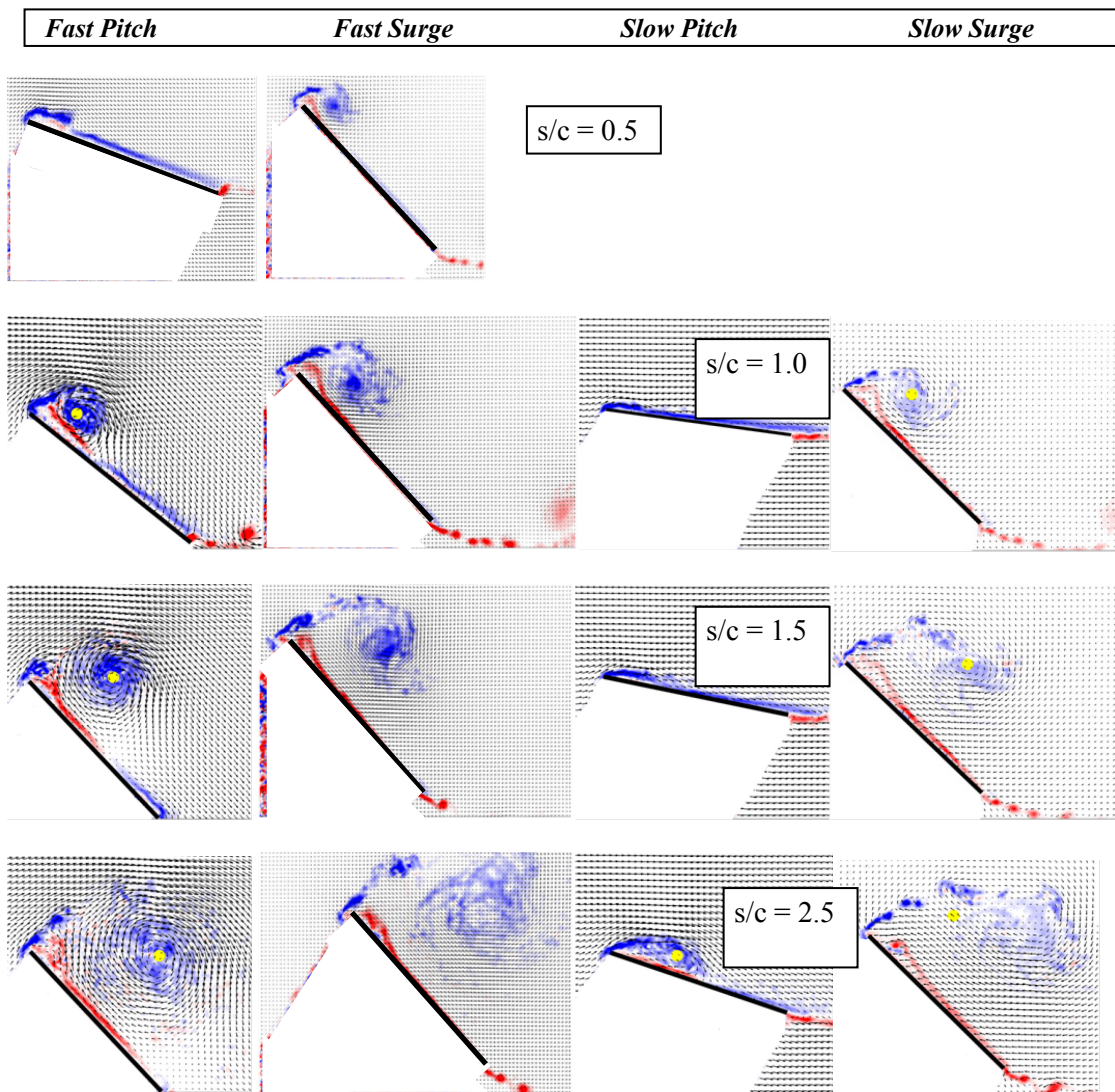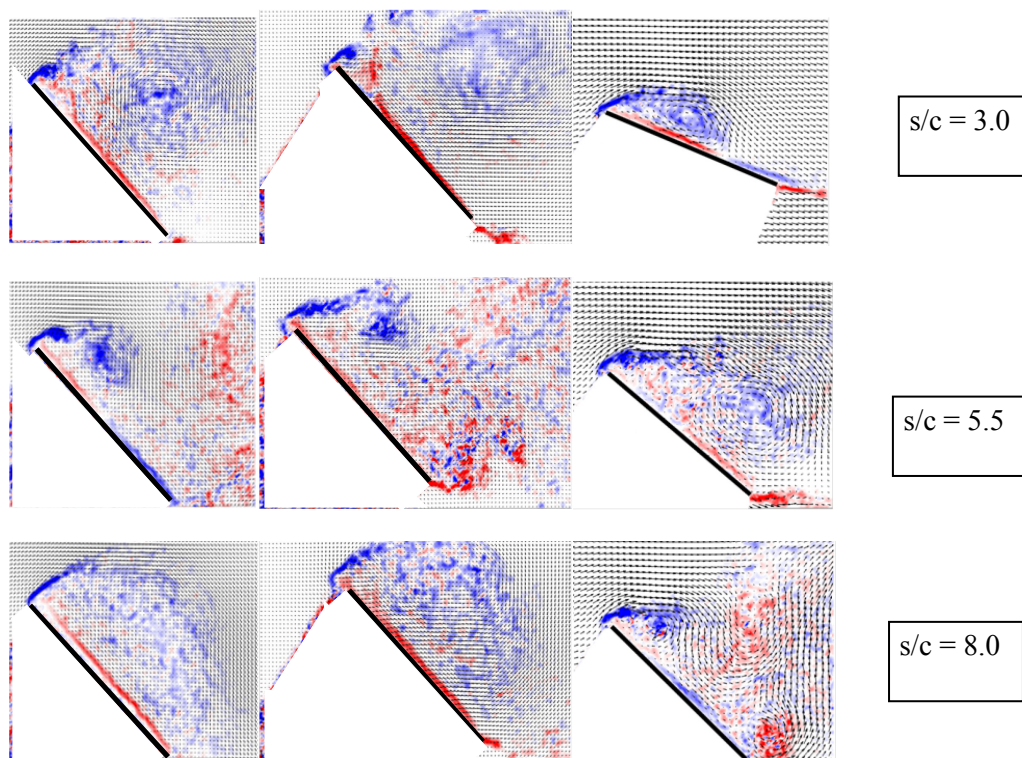
Figure 3-17: Frame-by-Frame Comparison of the Four Translational Cases, AR = 4 Plate, ¾-Span Location, with PIV-Derived Vorticity and Velocity; Time-Instance as Marked in Each Row.

3.3.2   Rotational Surge

Figure 3-18 follows the rubric of Figure 3-17 in rending sectional flowfield ensemble-averaged PIV results for the slow and fast rotational surge cases. In Figure 3-18, snapshots are arranged by azimuthal angle traversed by the plate, with conversion given from this angle to an "equivalent" arc-length. This length is normalized by chord, taken at the 15c/8 location spanwise along the plate, from the point of rotation. The reason for 15c/8 is that with 0.5 c root cut-out (that is, distance between the point of rotation and the inboard wingtip of 0.5 c), a distance of 15c/8 from the point of rotation is at 75% of the distance to the outboard wingtip [13].

Fast surge (50%)	Fast Surge (80%)	Slow surge (50%)	Slow Surge (80%)

$\varphi = 10°$
$s/c = 0.33$

$\varphi = 20°$
$s/c = 0.65$

$\varphi = 30°$
$s/c \sim 1$

$\varphi = 60°$
$s/c \sim 2$

$\varphi = 90°$
$s/c \sim 3$

φ = 180°
s/c ~ 6
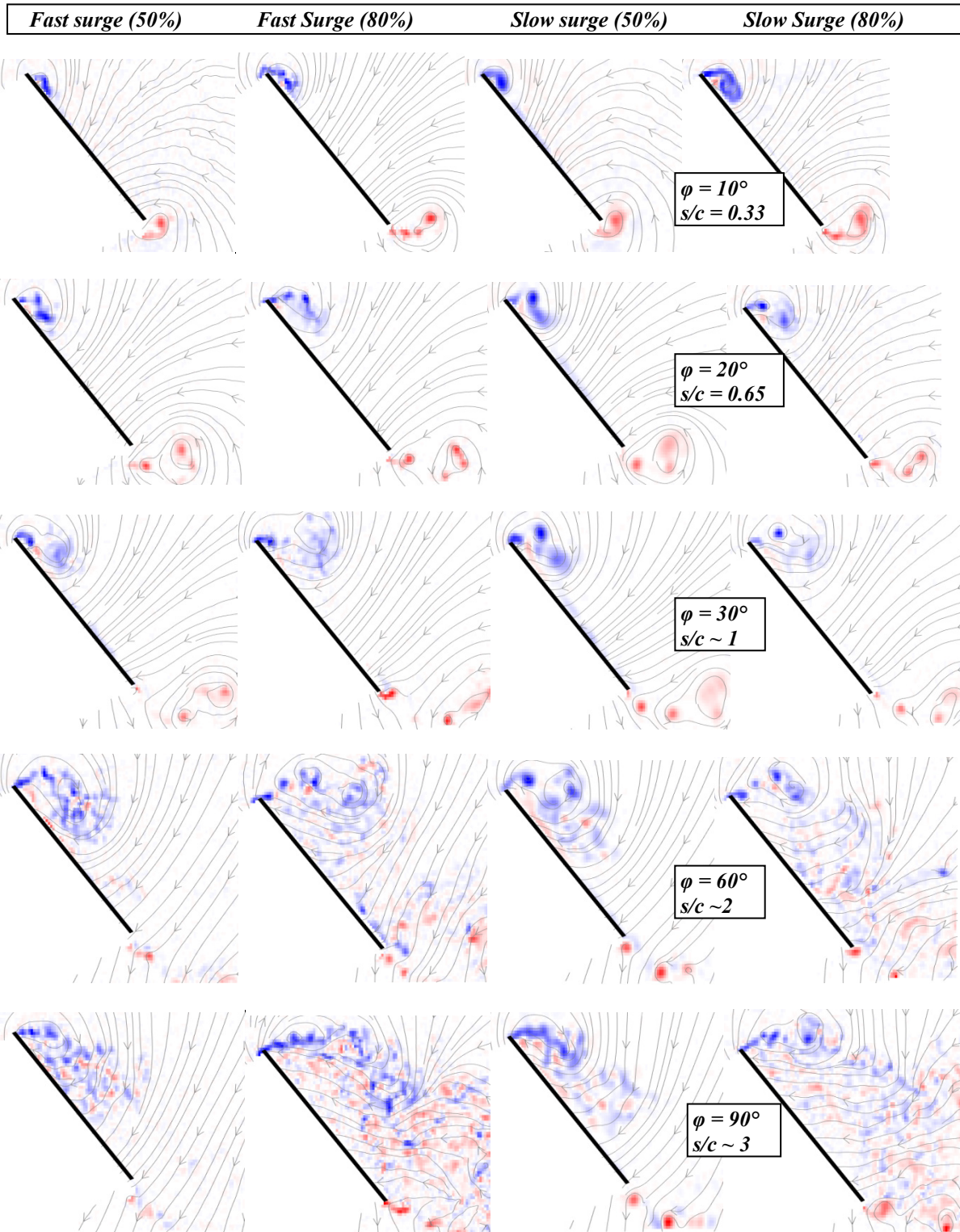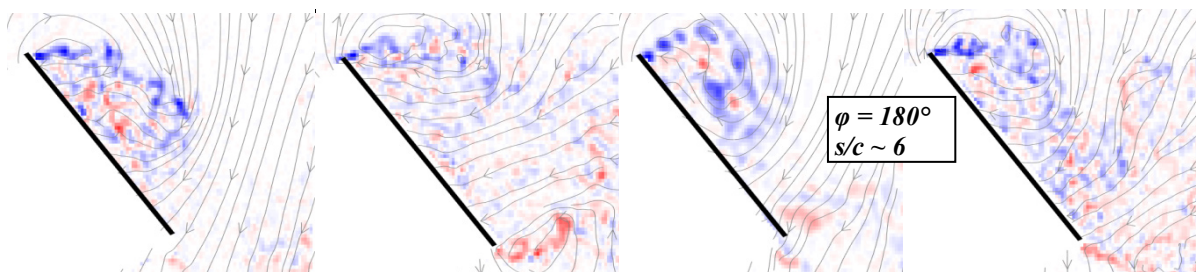
Figure 3-18: Tableau (Phase-Averaged PIV Vorticity Contours and Projected Streamlines, University of Maryland Group) of Rotational Surge Cases. Columns, left to right: Fast surge, 50% spanwise location (which is to say, at the midspan); Fast surge, 80%; Slow surge, 50%; and finally Slow surge, 80% spanwise location. Rows, top to bottom, are by degrees of azimuthal rotation at the snapshot, starting from rest: 10, 20, 30, 60, 90 and 180. This is equivalent to chord-normalized distance traveled (compare to Figure 3-17) of s/c = 0.33, 0.65, 1, 2, 3 and 6, respectively.

Two spanwise locations are given: 50% (the midspan) and 80% (that is, near the outboard tip). For all 50% images, whether the motion is "fast" or "slow", one sees in the aggregate a coherent LEV. Its constituent parts are not of one simply-connected, single-signed agglomeration of vorticity, evidently owing to vortex breakdown [47], but a vortex is nonetheless discernable without excessive recourse to poetic license. At the 80% spanwise location this is not the case. However emanates the leading edge shear layer, it does not appear to curve around towards the suction-side of the plate, and by s/c ~ 6 there is dead-water region on the plate's suction-side. Evidently, if there is stable LEV, it has curved around into the streamwise direction and has lifted off of the plate's suction side. More of this is discussed in 3D in the section on incidence-angle variations.

3.3.3   Rotational Pitch

Flowfield data on rotational pitch are not available from amongst the research-groups mentioned in the previous chapter. The reader is referred to Bross and Rockwell [15] for comparison of 3D PIV-derived flowfield measurements between rotational surge and rotational pitch.

3.4   APPLICATION OF THE LOW-ORDER MODEL

Having surveyed the measured/computed aerodynamic force history, vortex trajectories and the flowfield evolution, we now combine all three conceptual modalities to compare the modeled lift history for the translational cases with the measured/computed, where the model is predicated on:

1) Simple models of the vortex growth and motion (as discussed earlier); and

2) The assumption that in early-time the flow is acceptably two dimensional.

Thus, we have not applied the model to any of the rotational cases, although it remains to be seen whether a suitable 'strip-theory like' approach can yield some success.

3.4.1   Fast Surge Case

First we concentrate on the surging wing. In line with the observations discussed earlier we make the following assumptions:

1) The LEV grows as predicted by a Wagner function, albeit moderated during the acceleration phase by the instantaneous velocity $(t)/u_\infty$.

2) The relative motion between the LEV and the TEV is set to $0.3\,U_\infty$.

3) The distance between any newly formed additional LEV circulation and its TEV counterpart is one chord length (to be used in the 'vortex chord term').

Finally, the sum of all force contributions is smoothed to approximate typical experimental filtering of force data (although the level of numerical smoothing is still relatively small).

Figure 3-19 shows the result of the model and its individual contributions, compared to a notional experimental dataset; both are from the Cambridge group. The overall curve displays the familiar initial peak with a relatively quick return to some sort of steady-state value after the acceleration period. Further insight is gained by studying the individual force contributions. The main contributors to the initial force peak are the added mass and vortex growth terms. Thus we can see that for this motion the LEV growth is indeed a dominant factor in the lift generation, albeit enhanced by the non-circulatory term. Later on in the cycle the 'vortex motion' term dominates, thus taking the role of some sort of 'bound' circulation produced by the wing (although the LEV drifts away from the wing it nevertheless contributes a fair amount of lift). Interestingly, the decaying vortex 'vortex growth' term added to the asymptotically growing 'vortex motion' term gives an almost constant overall force in the post-acceleration phase. Throughout, the 'vortex-motion' term closely resembles the modified Wagner function (as it should since the relative velocity is assumed to be constant throughout) and thus the effect of the initial 'moderation' during the acceleration phase is seen clearly. It turns out that the exact kinematics during the acceleration phase have a significant impact, because the 'vortex growth' term depends strongly on the shape of the circulation growth curve. This is illustrated by an alternative application of the model from the Maryland group for the same test case, as shown in Figure 3-20.
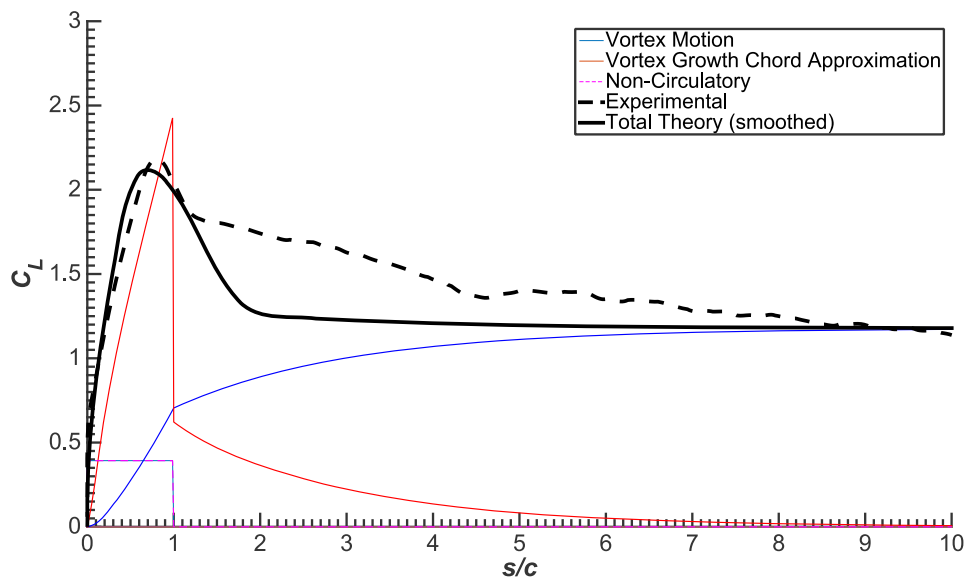
Figure 3-19: Low-Order Model Prediction for the Fast Surge Case (Data from University of Cambridge Group).
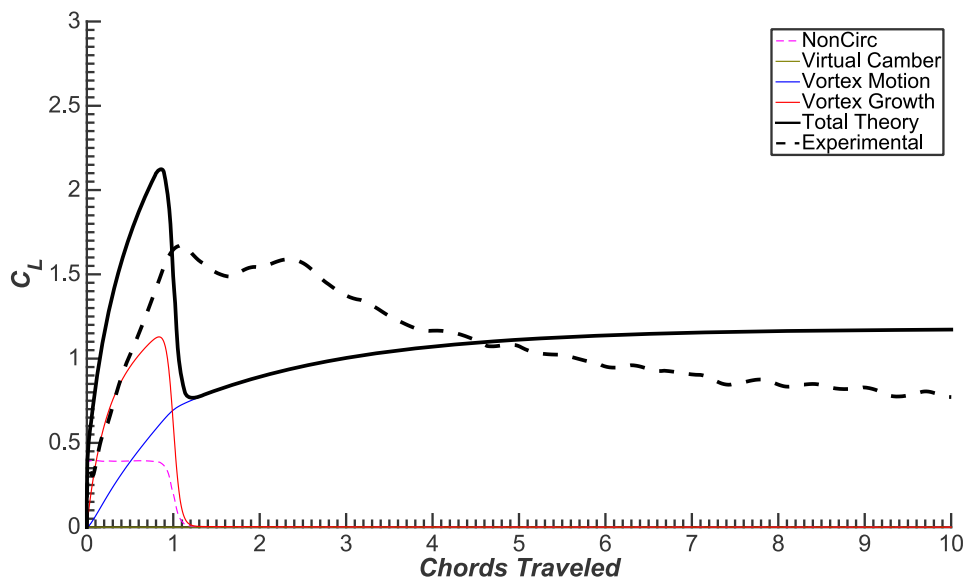
Figure 3-20: Variation on Figure 3-19, from the University of Maryland Group.

In Figure 3-20, a slightly different 'moderation' is applied to the Wagner function, and the resulting 'vortex growth' term has a rather different shape and magnitude, fitting less well with the experimental data. Note that there is a slightly non-standard implementation of the 'vortex growth' term, which also introduces some discrepancies during the constant-speed part of the motion.

Another sensitivity of the model is the relative LEV-TEV velocity. Figure 3-21 compares model predictions for two different relative velocities, $0.3\,U_\infty$ and $0.5\,U_\infty$. There is a considerable difference in the 'steady-state' portion of the model prediction.
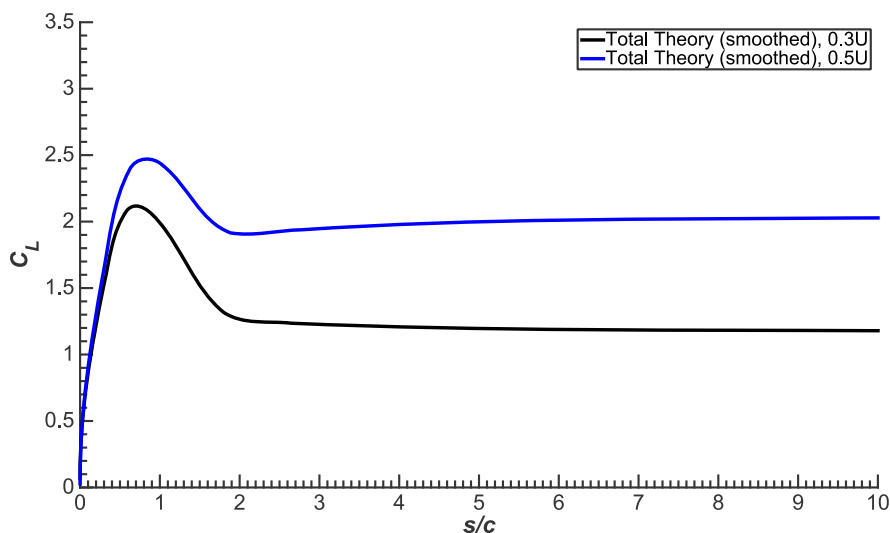
Figure 3-21: Low-Order Model Prediction for Lift Coefficient, for the Fast Surging Case with Two Different Relative LEV-TEV Velocities (All Other Parameters are Unchanged).

Returning to the original model prediction, Figure 3-22 compares the result for the fast surge case to all available datasets. Overall, the agreement is not too bad and the main features of the force history are well captured. The discrepancies during the acceleration period are almost certainly a result of subtly differing kinematics, which, as we have seen, can have a significant impact on the details of the force history at that time.
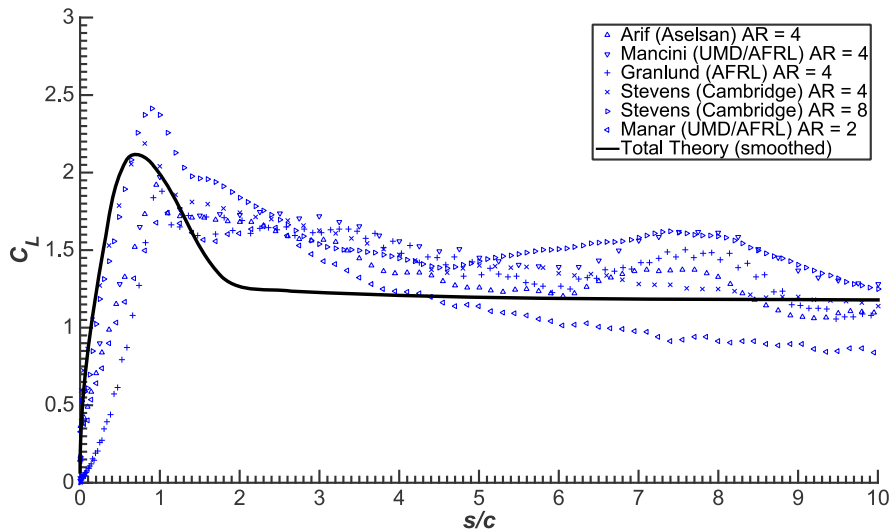
**Figure 3-22: Low-Order Model Prediction for the Fast Surging
Case, Compared with All Available Data Sets.**

Some of the force histories exhibit a small 'second peak' at around eight chords of travel. This is not predicted by the model, and a tentative explanation for its origins is given elsewhere in the Report.

3.4.2   Fast Pitch Case

Next, we turn to the pitch case. The following assumptions are employed:

1) The relative LEV-TEV velocity is set to 0.5 U_∞, in accordance with the recommendations made earlier.

2) The Wagner function is modified by the instantaneous angle of attack during the pitch-up motion.

3) "Eldridge" smoothing is applied in line with the kinematics of the relevant experiment performed by the same group.

4) The distance between any newly formed additional LEV circulation and its TEV counterpart is one chord length (to be used in the 'vortex chord term').

As before, the final model prediction is numerically smoothed to simulate a (small) amount of filtering.

Figure 3-23 shows the Maryland group's prediction for the fast pitch motion. It can be seen that all terms play a significant role during the unsteady part of the cycle and that the subtleties of the force curve are rather well reproduced. It is noteworthy that the model prediction does not display the gradual drop in lift seen later in the motion – this is most likely a result of the gradual drop in the relative TEV-LEV velocity which has not been implemented in the model (recall that at later times 0.3 U_∞ appeared to be a better fit).
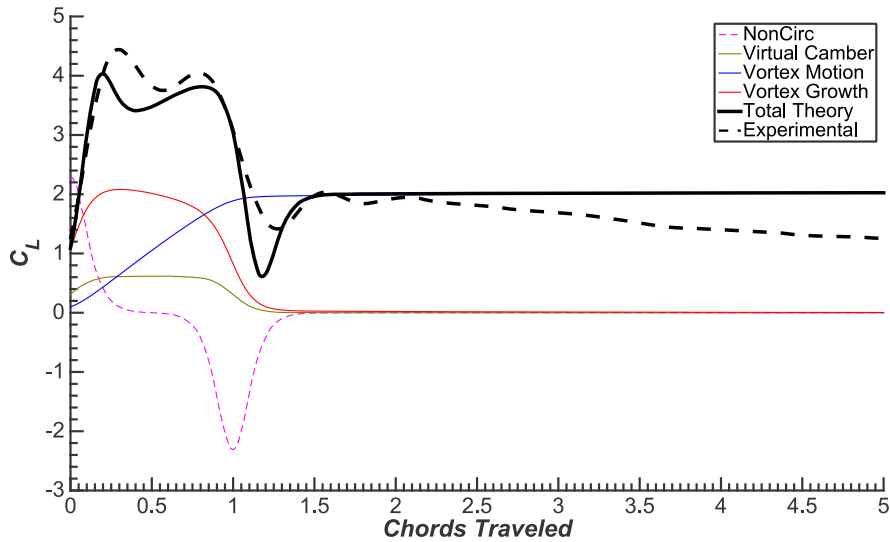
Figure 3-23: Low-Order Model Prediction for the Fast Pitch Case (Maryland Group).

Figure 3-24 shows the prediction for the same motion from Cambridge (albeit with slightly differing 'Eldredge' smoothing [7]). Unsurprisingly, this implementation better fits the Cambridge experimental data (shown in dashed). The large negative spike in the vortex growth term is a result of the apparent drop in effective angle of attack at the end of the motion (when the induced angle of attack vanishes). This has been incorporated in the modification to the Wagner function giving a drop in circulation at this point.
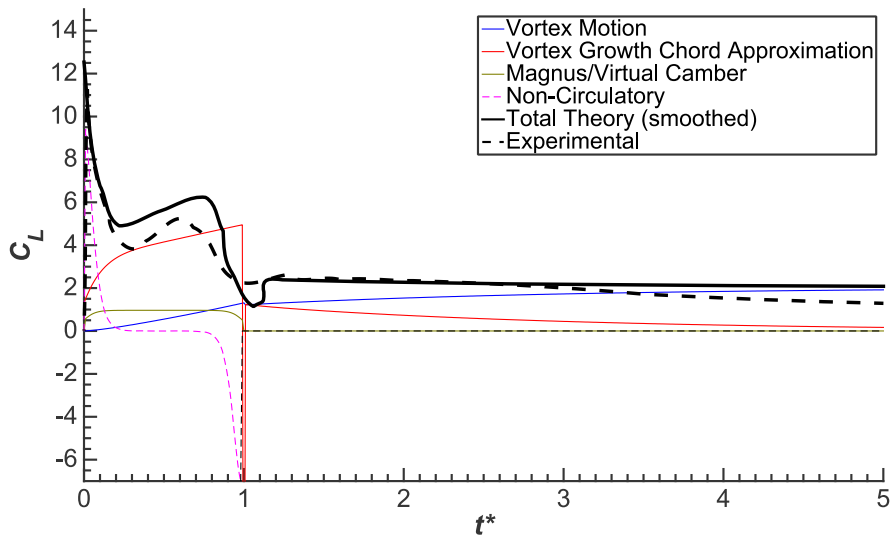
Figure 3-24: Low-Order Model Prediction for the Fast Pitch Case (Cambridge Data).

Finally, Figure 3-25 compares both predictions with all available datasets. It can be seen that both capture the shape of the force curve rather well. There is some over-prediction during the pitch phase, but this may be a result of not capturing the kinematics accurately.
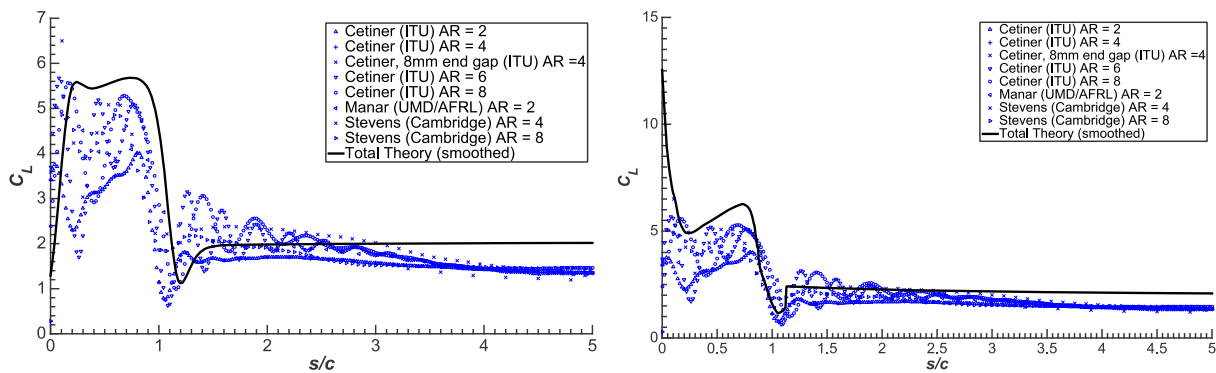
**Figure 3-25: Comparison of Low-Order Model's Prediction of Lift Coefficient
History vs. that of All Available Data Sets for the Fast Pitching Case.**

3.4.3   Slow Pitch and Surge Cases

The model has been found to give a relatively good fit with the data despite the fact that no information on actual vortex strength and motion was used directly (although it did inform the underlying assumptions). Thus, it is worthwhile to apply the same assumptions to the slow cases. It should be emphasized that it was not possible to accurately detect and measure the LEV and it is therefore unknown whether the assumptions of a 'Wagner-like' growth and a simple and constant relative LEV-TEV velocity hold for these cases.

Figure 3-26 shows the model predication for the slow surge case using exactly the same assumptions as for the fast case (modified Wagner vortex growth and 0.3 U_∞ relative LEV-TEV velocity).
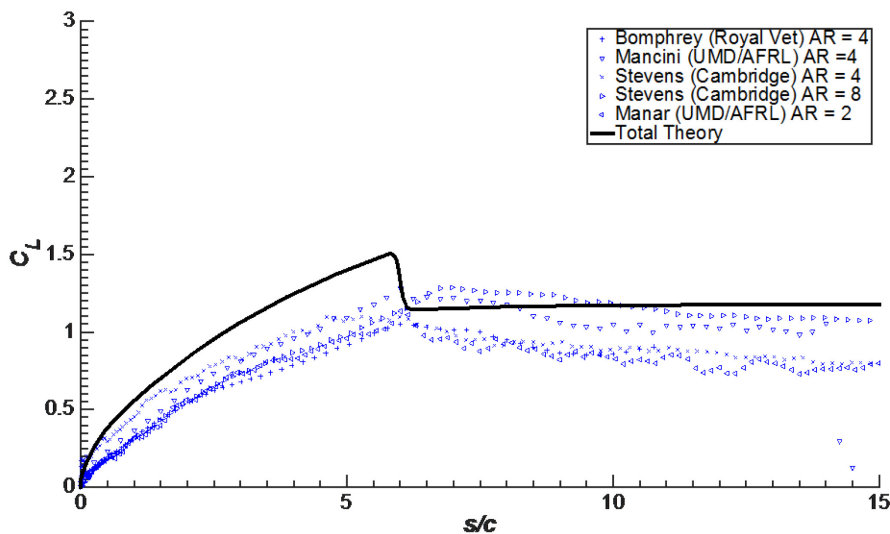
Figure 3-26: Low-Order Model Prediction for the Slow Surging Case.

Given the simplicity of the model, the agreement is satisfactory. Clearly, the vortex growth during the acceleration is over-predicted and this reflects with the experimental observation that no distinct LEV has formed. Nevertheless, the shape of the force distribution and several of its features are well captured.

Using the same model parameters, albeit with an increased LEV-TEV velocity of 0.5 U_∞ (in line with the assumptions made for the fast case), gives the prediction for the pitch case shown in Figure 3-27.
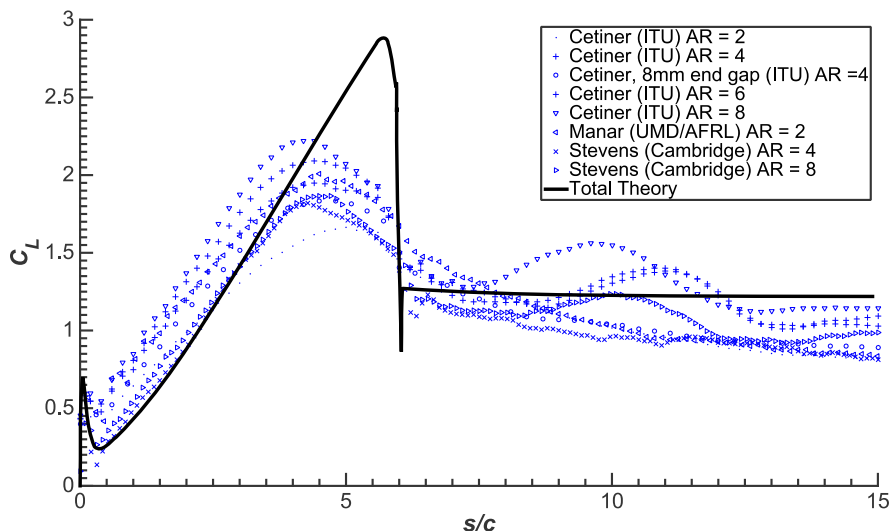
Figure 3-27: Low-Order Model Prediction for the Slow Pitch Case.

Once again, the subtle features of the force history are well captured (note, for example, the small spike at the start of the motion or the gradient of the force distribution during pitch) but the peak in force at the end of the pitch is significantly over-predicted. This is clearly a result of the real flow not being able to sustain a growth in circulation after approximately $3.5 - 4$ chords of travel. Close comparison with the flowfields show that this is approximately when the wing becomes stalled, and a large slowly re-circulating wake develops. This raises the question whether the prediction can be improved if this knowledge of 'flow breakdown' is implemented by imposing a maximum on the vortex circulation. This has been done by the Maryland group, and their prediction for the same case is shown in Figure 3-28.
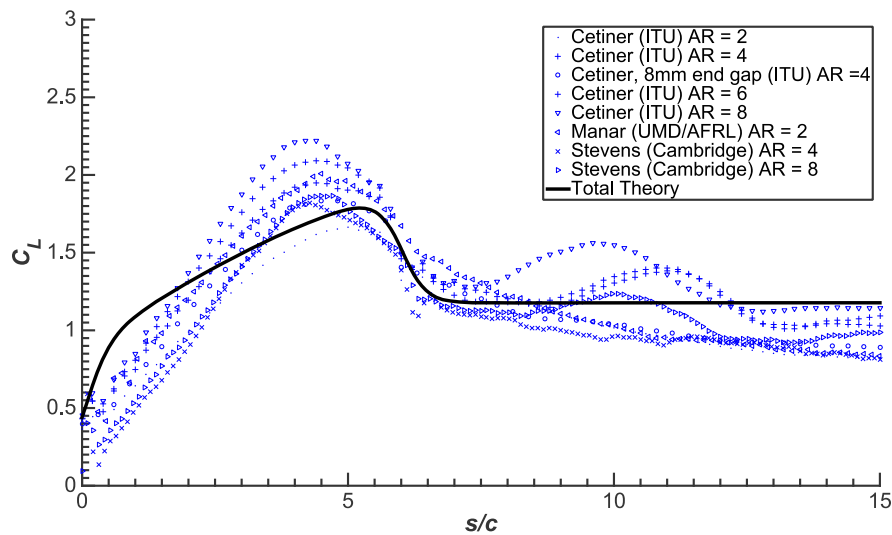
Figure 3-28: Low-Order Model Prediction for the Slow Pitch Case (Maryland Group).

Similar to before, the Maryland group employed a different treatment of the vortex growth which alters the shape of the force curve during the pitch but the behavior towards the end of the pitch and the maximum force are very well predicted.

These comparisons are not yet entirely satisfactory but it can be concluded the low-order force model is capable of capturing most of the relevant physics and that, after a bit of further research and fine-tuning of some of the underlying assumptions, it should be possible to predict the force history of pitching and surging wings with an engineering level of accuracy.

Chapter 4 – FURTHER PARAMETER STUDIES

Here we consider variations on the "canonical cases", whether in kinematics, geometry, testing conditions or other matters that hopefully inform the knowledge-base of the unsteady aerodynamics of pitching, and surging, rotation and translation. In some instances, contributions are ascribed to specific research groups; in others, they are amalgamated into a generic whole.

4.1 RECTILINEAR PITCH AND SURGE NOMINALLY IN TWO DIMENSIONS, AND ASPECT RATIO VARIATIONS IN RECTILINEAR AND ROTATIONAL MOTION

Here the canonical-case kinematics have been retained, but plate AR is varied; a slight exception is the 2B case (rotational surge). No AR study has been conducted for the 2A rotational pitch case. For translational cases, it is useful to distinguish between physical and effective AR. The physical AR is the full span wing of that AR, whereas the effective AR stems from an image (symmetry) plane; elaboration is given below.

4.1.1 Case 1B: Translational Surge

Figure 4-1 compares AR = 2, 4 and 8. The AR = 8 lift history (Stevens) does not vary from the AR = 4 canonical case, but the AR = 2 (Manar) does. The secondary peak in lift at around s/c = 8 is not visible in the AR = 2 case and is especially strong in the AR = 8 case. Evidently this peak is tied to formation and ejection of a secondary LEV – a phenomenon influenced by aspect ratio.
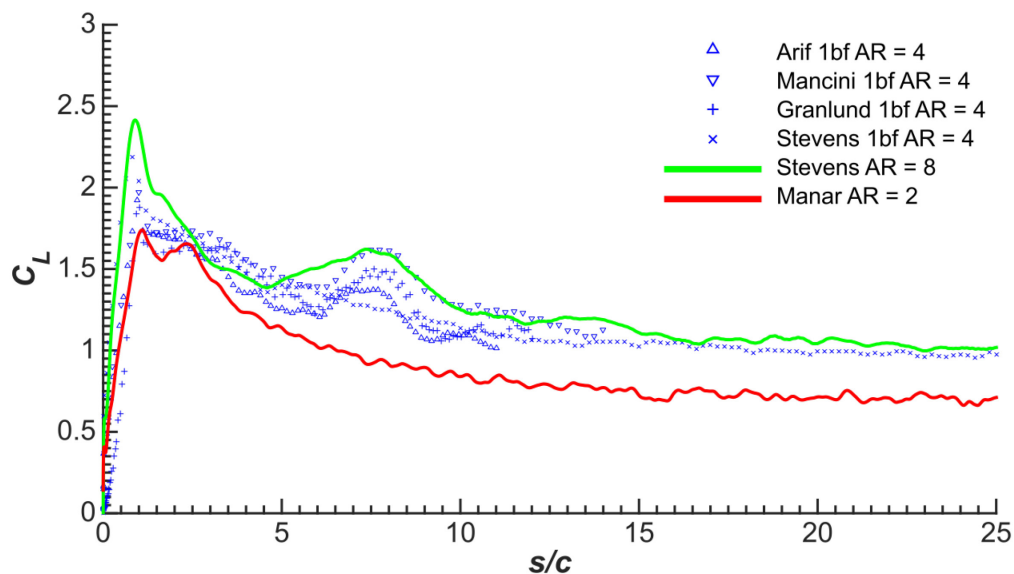
Figure 4-1: Case 1B, Fast Translational Surge AR-Variation.

The slow surge AR-variation lift history is shown in Figure 4-2. Again there is a clear AR effect, with the effective AR = 8 wing producing a higher lift than the corresponding effective AR = 4 data from the same

facility. The AR = 2 data is lower than the higher AR data, but interestingly it is very similar to the effective AR = 4 (physical AR = 2) data of Stevens. This hints that there is an effect of flow three-dimensionality on the lift history and that the use of a symmetry plane may affect the force history. This hypothesis will be discussed further in the following section.
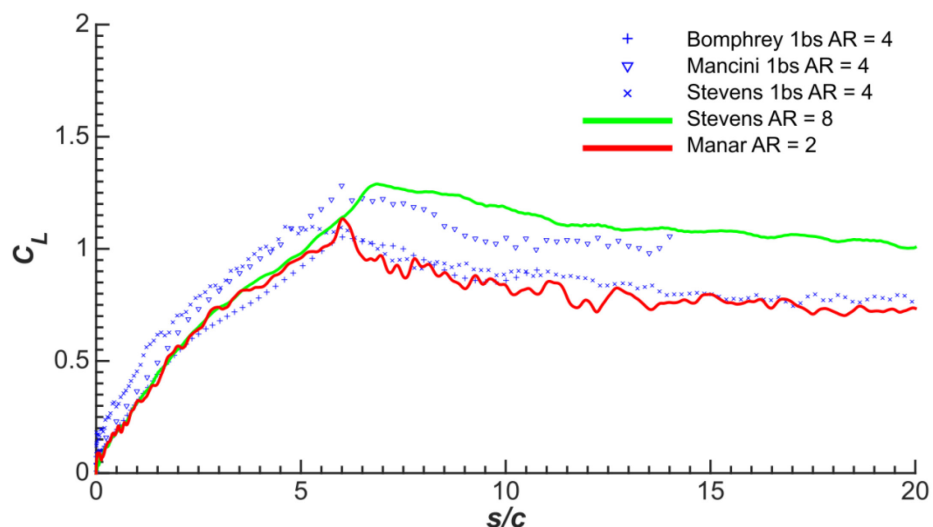
Figure 4-2: Case 1B, Slow Translational Surge AR-Variation.

4.1.2 Case 1A: Translational Pitch

In this section, the effect of force history on AR is complemented by flow visualization.

The fast pitch AR lift history comparison is given in Figure 4-3, and the corresponding slow case in Figure 4-4. The data sets are for plates vertically suspended in water tunnels or towing tanks, and AR-effects include the role of splitter plates. The curves within each figure are qualitatively similar to each other, but there is one key difference. In the region around s/c = 8 we see that the secondary rise in the lift is accentuated with increasing AR. When the aspect ratio is increased to 6 and above, a second and even a third bump is present in the force variations.
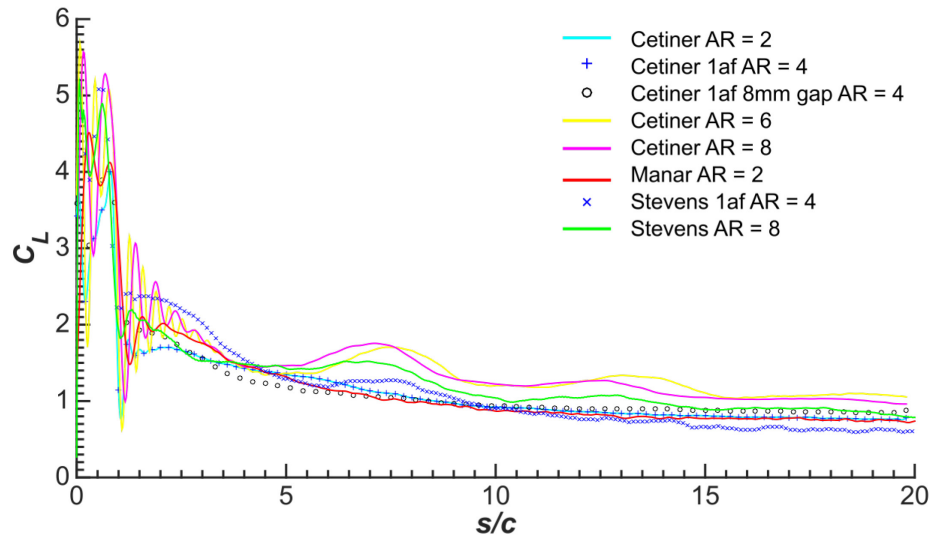
Figure 4-3: Case 1A, Fast Translational Pitch AR-Variation. All results are for plates vertically mounted in water tunnels or towing tanks.
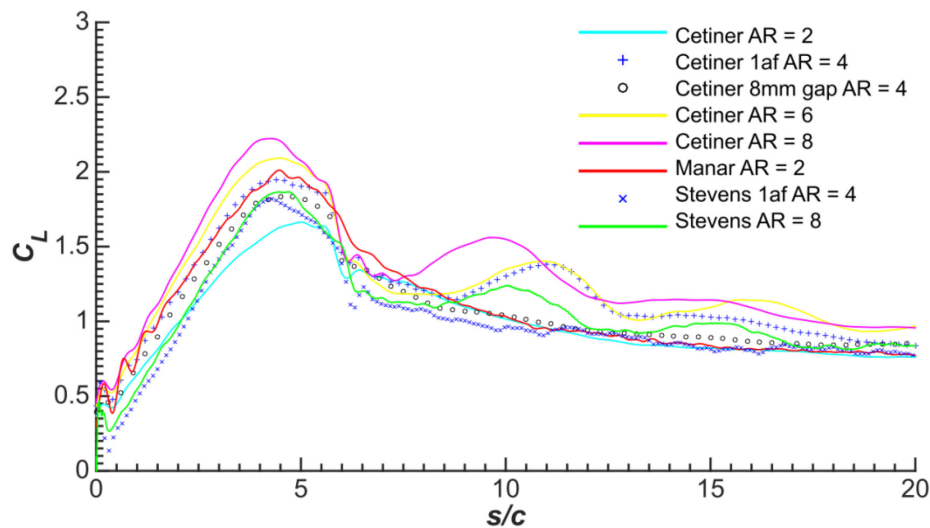
Figure 4-4: Case 1A, Slow Translational Pitch AR-Variation. All results are for plates vertically mounted in water tunnels or towing tanks.

In addition, Cetiner has conducted a series of aspect ratio variation experiments, either using an endplate to represent the symmetry plane or submerging the wing deep in water; this is elaborated in the section on variations of leading edge shape. This includes study of the effect of the gap between the wing and the symmetry plane endplate. When the gap between the root of the wing and the endplate increases to 8 mm, the endplate no longer represents a symmetry plane and the wing behaves as if its effective aspect ratio is equal to its geometric aspect ratio. Therefore a difference in tip vortex formation is incurred. Keeping in mind the difference in the physical span sizes of the wings, the use of a symmetry plane does not create a substantial difference in force

history during the pitching part of the motion, irrespective of the pitch rate. However, the bump in the lift traces differs for the cases where the geometric and effective aspect ratios are equivalent (no symmetry plane cases).

An alternative presentation for the slow translational pitching case, and the fast case, is given in Figure 4-5 and Figure 4-6, respectively. Here we compare three plates mounted horizontally in the test section, with no symmetry plane and no free-surface effects: wall-to-wall plate (nominal 2D case), the canonical AR = 4 (physical aspect ratio) and AR = 2 (also physical aspect ratio). In this presentation, AR-trends are somewhat more apparent than in the prior four figures, especially in lift coefficient; that is, AR-effects on drag are more benign. AR-effects also appear to matter more for the fast case, than for the slow. For the slow case, AR = 2 differs more from AR = 4, than AR = 4 from the nominal 2D case, especially in the sense of the AR = 2 case not evincing a secondary bump in lift at $t^* \sim 8$. Considering the drag variations, the higher-AR producing higher drag is in opposite direction from trends expected from lifting-line theory for induced drag variations with aspect ratio. Clearly, AR-trends are different for attached flow (at 45 degrees incidence) than for separated flow. It remains to ascertain the role of blockage, which is not corrected in any of these results.
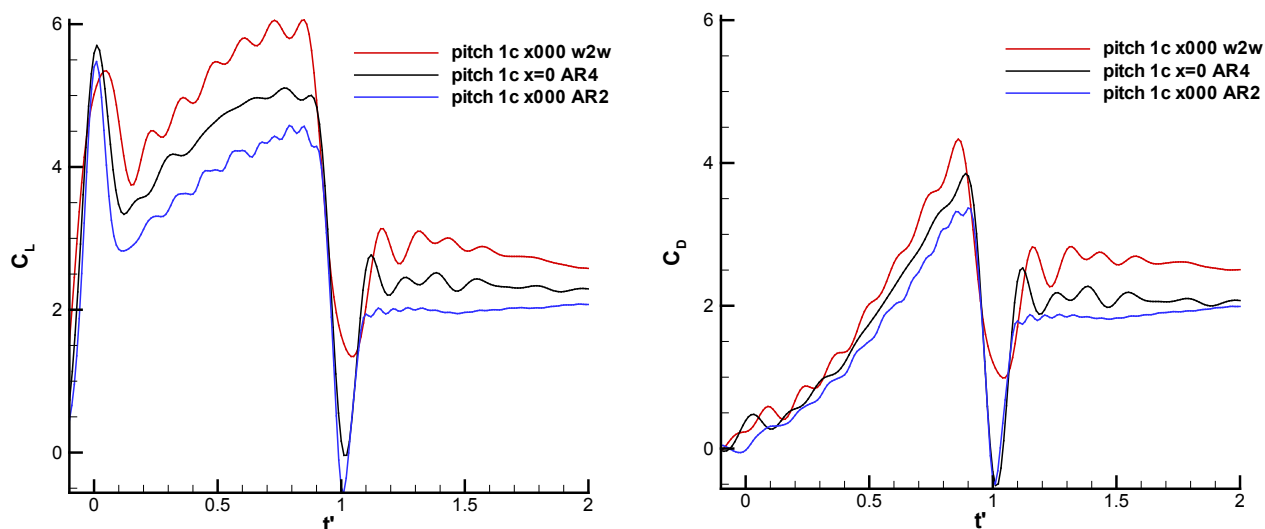
Figure 4-5: Aspect Ratio Effects on 1 *c* (Fast Case) Pitch; Lift (Left) and Drag (Right).
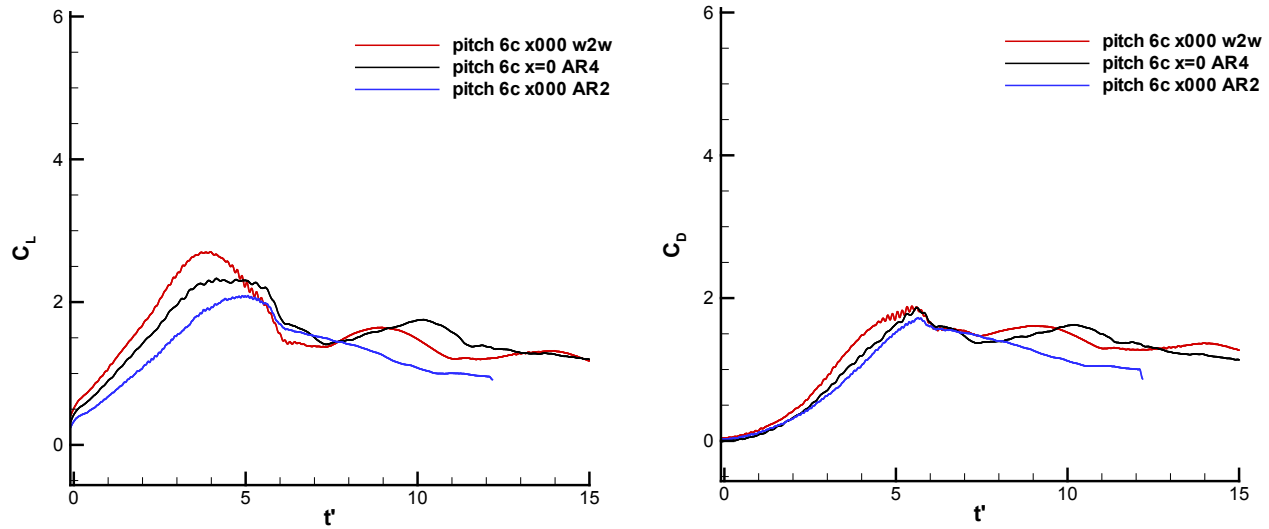
Figure 4-6: Aspect Ratio Effects on 6 *c* (Slow Case) Pitch; Lift (Left) and Drag (Right), 6 *c* Case.

We next turn to flowfield comparisons of aspect ratio effects, examining sectional-images of plates vertically suspended, comparing flow visualization with projected streamlines derived from ensemble-averaged 2D PIV snapshots.

Figure 4-7 covers the fast pitch case, and Figure 4-8 the slow. For both Figure 4-7 and Figure 4-8 the left half of the figure is for effective AR = 4, and the right half for effective AR = 8. Also for both figures, snapshots (a), (c), (e) and (g) show the flow evolution during the pitching part of the motion, while (b), (d), (f) and (h) cover conditions when pitch has completed.
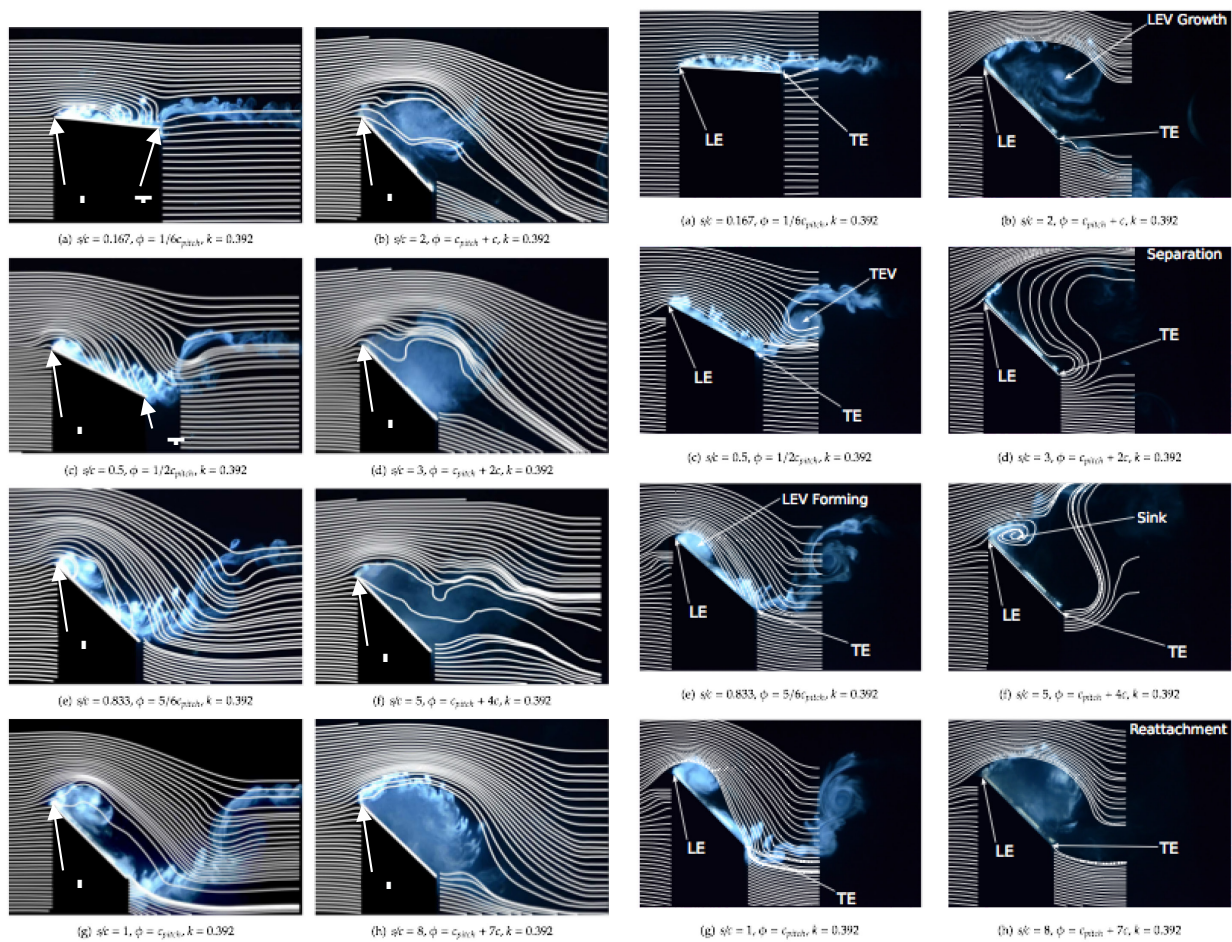
Figure 4-7: Case 1A Fast Pitch, with Pitching Motion Occurring Over One Chord. Flow visualization with PIV ensemble-averaged streamlines superimposed. Effective AR = 4 in left set of eight snapshots, and AR = 8 in right set of eight snapshots.
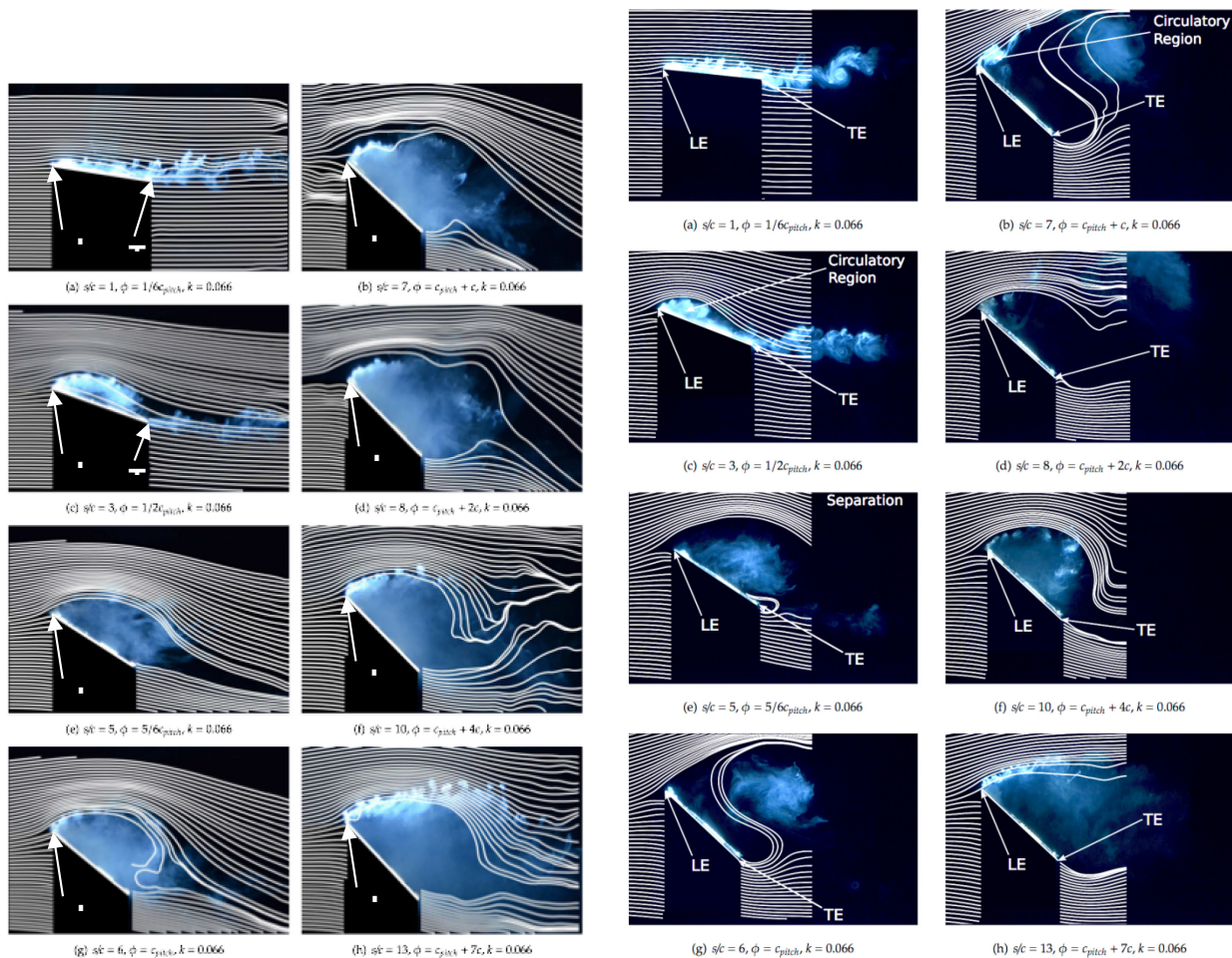
Figure 4-8: Case 1A Slow Pitch, with Pitching Motion Occurring Over Six Chords. Flow visualization with PIV ensemble-averaged streamlines superimposed. Effective AR = 4 in left set of eight snapshots, and AR = 8 in right set of eight snapshots.

Considering first the fast case in Figure 4-7, at $s/c = 0.167$, the dye appears attached to the plate, and there are no signs of flow separation yet. At $s/c = 0.5$, there is a noticeable recirculatory movement of dye in the LE region, suggesting a small LEV. The rest of the flow is attached. Downstream of the TE, a strong vortex (TEV) can be seen. At $s/c = 0.833$, the presence of the LEV is much clearer, and most of the dye is entrained into this flow structure. The TEV has advected aft. At $s/c = 1$, the dye is fully entrained, and a large, coherent LEV is visible, with a clear core region. Streamlines during pitch clearly show bounding of the LEV with highly curved streamlines 're-attaching' before the TE, with the re-attachment point moving aft with increasing incidence. In Figure 4-7(c), we can see that there is an effective camber on the flat-plate, created by the dividing streamline bounding the LEV. This effective camber effect is observed until the end of pitch (where the streamlines begin to lift off). Comparing the effective AR = 4 pitch streamlines with the effective AR = 8 streamlines we observe a very similar pattern, with the exception that the streamlines are more aggressively curved at $s/c = 1$ for AR = 8.

At $s/c = 2$ in Figure 4-7, the LEV continues to grow and the dye disperses, indicating a loss of vortex coherency. Streamline curvature attenuates, and there is no streamline 're-attachment'. At $s/c = 3$, the LEV becomes hard to identify. At $s/c = 5$, a shear layer normal to the plate is seen at the LE. At $s/c = 8$, a large re-circulatory body of

fluid is observed above the wing, lacking the coherency of a LEV, but nevertheless appearing to re-attach at the TE of the plate. Here the streamlines show greater curvature, and the implied pseudo-reattachment correlates directly with the small rise in lift coefficient previously mentioned. Differences between AR = 4 and AR = 8 are somewhat larger after completion of pitching motion, than during the pitch.

The slow-pitch flow visualization in Figure 4-8 again shows that the AR = 8 plate exhibits the secondary lift bump, but at a later convective time (~s/c = 10) than for AR = 4. The lower AR wings typically do not exhibit this feature, suggesting that tip effects are more evident at longer convective times. Unlike for the fast case, there is no indication of the formation of a coherent LEV. There is however a body of flow with a weak circulatory tendency, which is clearly seen at s/c = 3. There is evidence of streamline TE re-attachment up until this point. The flow is broadly separated by s/c = 5. This is in contrast to the fast pitch case, where a dividing streamline reattaches to the plate for the entirety of the pitching motion. Comparison with the pitch part of the cycle for the effective AR = 8 wing shows that for AR = 8, there is a more dramatic loss of streamline curvature than for AR = 4. As regards the secondary bump in lift, again there is a body of circulatory fluid and streamline TE reattachment at s/c = 10 for both the AR = 4 and AR = 8 plates; compare this with analogous reattachment at s/c = 8 for the fast pitch case.

The two-dimensional case is strictly speaking realizable only computationally, as in the wind tunnel or water tunnel there are inevitable endplate effects or wall effects. 2D vortex-particle computations (Figure 4-9; results from the Wroclaw University group) show similarity in LEV and TEV formation relative to the AR = 4 (and other finite-AR) cases during the pitching motion. But after 45-degree incidence has been established, bluff-body shedding in 2D is quite different from that evinced for finite AR, and presumably the absence of tip vortices has implications for both the shedding-history and the lift/drag history.
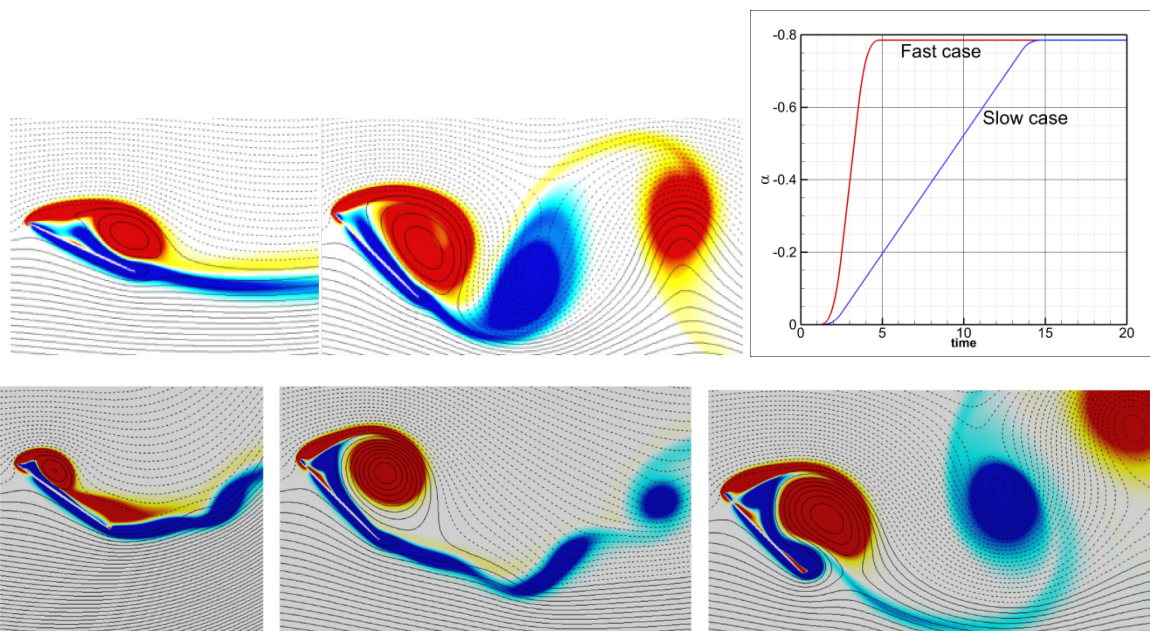
Figure 4-9: Vorticity Contours for Slow Pitch (Top Row) and Fast Pitch (Bottom Row) at the Following Snapshots of Time: for the Slow Case, 8.55, Corresponding to Halfway Up the Pitch Ramp, and 15.58, at the Conclusion of Pitch; for the Fast Case, Time 3.55, Corresponding to Slightly Before Halfway Up the Pitch Ramp, 5.05, at the Conclusion of Pitch, and 10.05, at a Subsequent Vortex Shedding Cycle Well After Motion is Completed. Top right-hand corner: Angle of attack history vs. physical time.

4.1.3   Case 2B: Rotational Surge

The discussion is based on Carr, DeVoria, and Ringuette [40], for plates of AR = 2 and 4. Conditions approximate the fast rotational surge case, 2B. The U_{tip} and span b are used for normalisation, and Re_{span} is matched to isolate AR effects [45].

Figure 4-10 shows a sequence of 3-D Q iso-surfaces versus the angle of rotation, φ, for AR = 2 and 4 plates, Re_{span} = 10,000. The flow structures for AR = 2 and 4 show similarities at $\varphi = 30°$, including outboard LEV lift-off into an arch-like structure, and a perpetually "stable" LEV inboard. These features are in good agreement with Garmann and Visbal [55], Jardin *et al.* [46] and Ozen and Rockwell [19]. As the first LEV lifts off, another forms ahead of it that connects to the TV for both ARs ($\varphi = 30°$). Note also the aft progression of the trailing vortex loop. However, substantial variations with AR exist. The AR = 4 LEV is farther aft at a given percent span than for the shorter AR = 2 wing. For AR = 4, by $\varphi = 60°$ the initial lifted-off outboard LEV is aft of the TE, and three smaller LEVs have formed ahead it. Concurrently, the initial, main TV travels aft of the TE. However, for AR = 2 by $\varphi = 60°$ the first outboard LEV has tilted aft and merged with the TV; both are close to the wing. The AR = 4 outboard LEV becomes larger ($\varphi = 60°$, red arrow), which is a sign of breakdown [47]; this was similarly found by Lu and Shen [48] and Garmann and Visbal [55]. By $\varphi = 90°$, this outboard breakdown has progressed substantially, qualitatively indicated by small, disorganised structures. Breakdown adversely affects the mean-flow convergence from phase averaging, leading to the reduced coherence observed in the iso-Q surfaces. For AR = 2, at $\varphi = 54°$ (inset) the aft-tilted LEV also increases in size. At $\varphi = 90°$, the outboard AR = 2 LEV/TV flow shows prominent breakdown with an LE shear layer ahead of it; the AR = 4 flow exhibits a similar shear layer. The breakdown behavior is similar to the dye flow visualizations of Carr and Ringuette [40]. Despite breakdown, the AR = 2 outboard vortical flow remains more coherent and nearer to the wing.
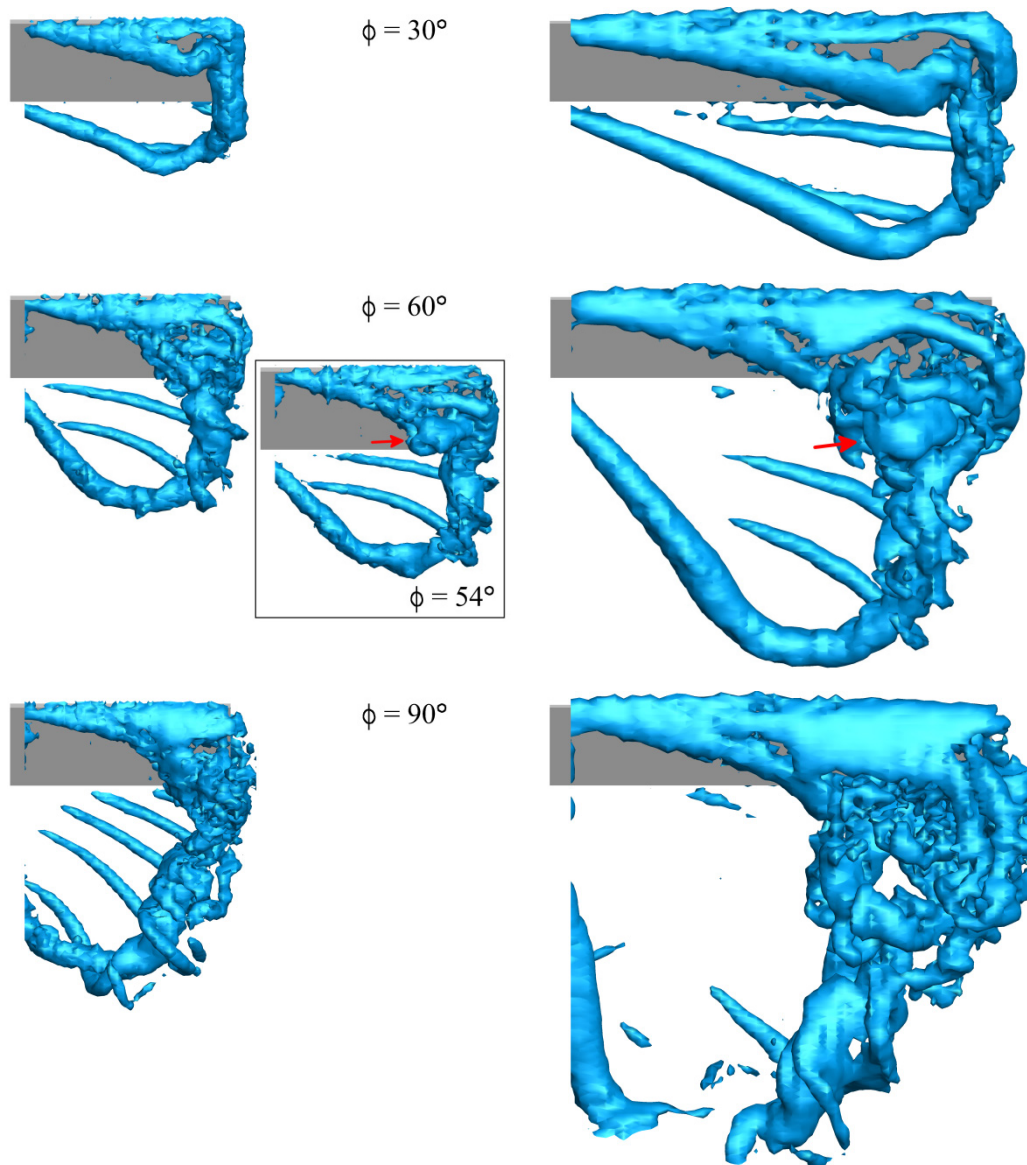
Figure 4-10: Top, or (x, z)-Plane View, of an Iso-Surface of Non-Dimensional $Q = 12$ at Various φ; AR = 2 (Left Column), AR = 4 (Right Column). Red arrow indicates LEV enlargement prior to breakdown.

Figure 4-11 gives span-averaged total and LEV circulations, Γ_{total} and Γ_{LEV}, versus the phase angle of rotation, φ. The Γ_{total} comes from an (x, y)-plane ω_z area integral for all grid points with $\omega_z > \omega_{z,th}$ (within a $1\ c \times 1\ c$ domain above the plate for AR = 2, and $1.5\ c \times 1.5\ c$ for AR = 4). It is normalized by the local azimuthal wing velocity, U_{local}, yielding more comparable magnitudes across the span, then averaged from 20% − 80% span. The Γ_{total} increases with φ, with an initially larger slope, and then with a more gradual rise from the continual formation of smaller outboard LEVs. The AR = 2 Γ_{total} is larger, due to its more coherent outboard flow, but the slopes for AR = 2 and 4 are very similar. The Γ_{LEV}, calculated only from identified LEV points, is span-averaged only over the "stable" LEV, from 20% − 60% and 20% − 40% span for AR = 2 and 4, respectively. The AR = 2 Γ_{LEV}

grows initially then saturates ($\varphi > 36°$). For AR = 4, after the larger initial slope, Γ_{LEV} increases gradually; fluctuations are from occasional LEV "splitting" at $\sim 40\%$ span.
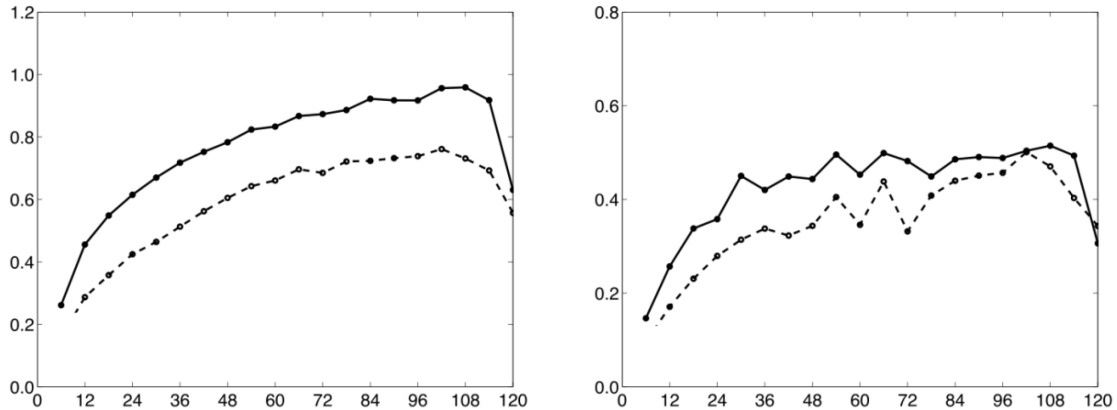
Figure 4-11: Circulation vs. Phase-Angle of Rotation; (a) Span-Averaged Γ_{total};
(b) Span-Averaged Γ_{LEV}, "Stable" LEV. Solid: AR = 2, dashed: AR = 4.

Figure 4-12 plots C_L (normalized using $U_{75\%}$ for comparison with others) for AR = 1–4 vs. (a) $t^*_{75\%} = tU_{75\%}/c$ and (b) the period for the $\varphi_{final} = 120°$ cases, $t/T_{120}°$. Solid lines indicate $\varphi_{final} = 120°$, while dashed signify 360°; deceleration portions are removed. The $Re_{75\%}$ for AR = 1 − 4 are similar: 4,870, 4,310, 4,120, and 4,030, respectively. Data for $Re_{75\%}$ down to $\sim 1,000$ show no significant Re effects. Recall that acceleration for all ARs occurs over $\varphi = 10°$, and therefore to achieve a similar $Re_{75\%}$ the lower AR wings require higher acceleration rates, leading to larger initial C_L peaks.
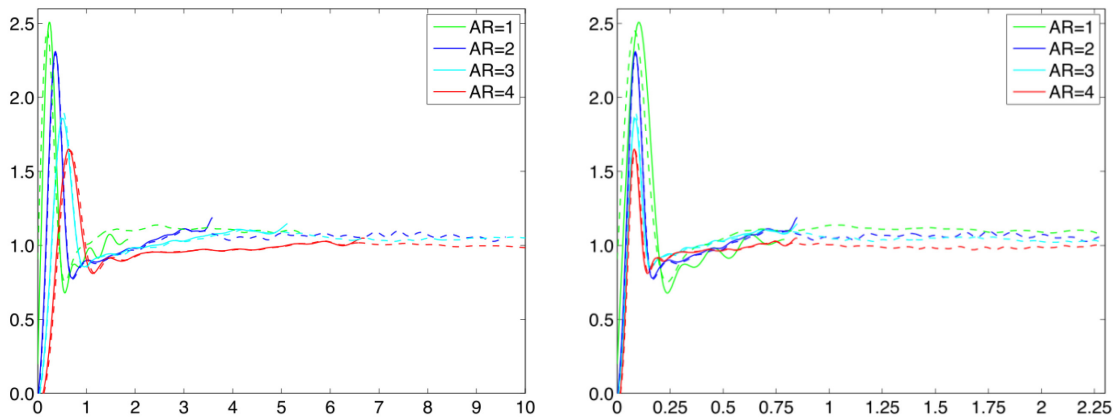
Figure 4-12: C_L for AR = 1 – 4, (a) vs. t^*, (b) vs. $t/T_{120}°$. Solid: φ_{final} = 120°, Dashed: φ_{final} = 360°.
Deceleration portions removed; for (b) not all AR = 4, φ_{final} = 360° data shown (see text for details).

Figure 4-12(a) and (b) show common features for all ARs: an initial C_L peak due primarily to non-circulatory force during acceleration, followed by a local minimum, a slow growth period, and finally a plateau; compare with Schlueter *et al*. [13] When plotted against $t^*_{75\%}$ (Figure 4-12 (a)), the initial peak locations vary with AR,

due to the common acceleration over $\varphi = 10°$. When plotted versus t/T_{120}, the C_L peaks essentially coincide. The slightly higher C_L long-time values for lower AR are likely due to the more coherent TV, which affects a relatively larger portion of the wing. It is a low-pressure region, which will enhance lift, as will its induced upwash near the tip edge [49].

In summary, PIV data indicate a "stable" LEV inboard of ~50% span for both AR = 2 and 4, with arch-like LEV lift-off and multiple LEVs outboard. Outboard LEV breakdown is found for both ARs, but the AR = 2 LEV merges with the TV and remains more coherent and near the wing. The slopes of the total spanwise circulation versus rotation angle for each AR are similar, indicating similar LEV force contributions, pointing again to the TV as a main cause for the C_L differences with AR.

4.2   VARIATIONS IN REYNOLDS NUMBER

In this parameter study, the kinematics of the canonical motion is retained, but we compare directly several different Reynolds numbers. Reynolds number was not specified to a "canonical" value, and therefore the experiments and computations mentioned thus far in this Report vary greatly in Re amongst each other. In the present section, the focus is on systematic Re-variations in one test-sequence, thus obviating exogenous effects of different test conditions such as blockage, force-data filtering and so forth.

One scheme for large variations in Reynolds number in the same nominal experimental rig is to mix glycerin and water. Mixtures between 100% glycerin and 100% water yield a kinematic viscosity range of $10^{-6} < \nu < 10^{-3}$ [50] This was the approach taken in the AFRL water tunnel, where a tank with glycerin/water mixture was inserted into the water tunnel test section and surging-type motions using the tunnel's existing linear-motors were run. Since it is impractical to pump glycerin-water mixtures with a conventional axial impeller pump, pitching motions – with a steady free-stream – were not possible. The glycerin/water mixture usage in tanks is not new. Other recent examples include the rotational experiments of Ringuette *et al.* [40].

Figure 4-13 compares lift coefficient history for the "fast" and "slow" translational surge cases at Re = 13 and 29 (pure glycerin), 330 (glycerin-water mix) and 10.000 (pure water).
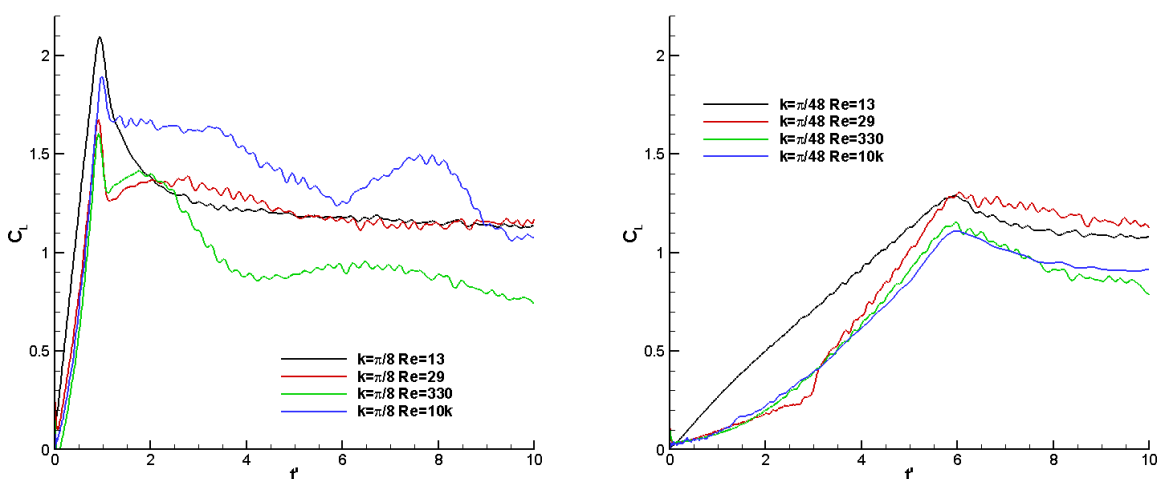
Figure 4-13: Lift Coefficient for an AR = 4 Plate at θ = 45° with Constant Acceleration from Rest, Over 1 Chord (Left) and 6 Chords (Right), to Constant Velocity at Four Different Reynolds Numbers.

In both the fast and slow acceleration motion, the lowest Reynolds number case produces the largest force during the acceleration phase, with all higher-Re cases essentially being the same. The lowest Reynolds number of 13 asymptotically approaches a steady-state value (which would occur after many more lengths than observed here), without any lift fluctuations. This is an indicator of no vortex activity, since there is presumably rapid dissipation of vorticity in the shear layer from the leading edge before it has time to roll up into an LEV. For Re = 29, lift during the constant velocity part is the same as for the lowest Reynolds number. For Re = 330, for the fast case here is a decline in lift after the accelerated-portion is over, relative to the lower-Re cases. For the slow case, this decline persists for Re = 10,000, which is almost identical to the Re = 330 result. For the fast case, the Re = 10,000 evinces higher lift than the very low-Re cases, suggesting that the intermediate value of Re = 330 has some special property. The oscillations in lift during the constant velocity portion of the motion is strongest in the higher-Re case, presumably due to more vigorous LEV and TEV re-formation after the initial starting LEV and TEV once motion first commences. However, in no cases is there a strong trend of lift with Reynolds number. We conclude that the effect of Reynolds number is quite weak, which is perhaps surprising because at the lowest Re there is no discernible LEV or TEV.

For convective problems with a steady free-stream, change in Re generally means changing the test article's size, or the free-stream speed. The former runs into blockage problems if the test article is large, and load-cell signal-to-noise ratio problems in the opposing case of a small test article. The same problem occurs if tunnel free-stream speed is reduced, as small dynamic pressure complicates tares and reduces the load-cell signal. Inversely, a large free-stream speed means a high physical acceleration-rate of the test article, to preserver reduced frequency, and that introduces mechanical vibration and a low (in dimensionless terms) system natural frequency.

Thus in pure water, the available range of Reynolds number is less than one order of magnitude. Figure 4-14 shows the result for the slow translational pitching case for Re from 15 K through 40 K. Over this range, the Re-effect is indeed very small, and perhaps cannot be disentangled from differences in flow quality and load-cell response.
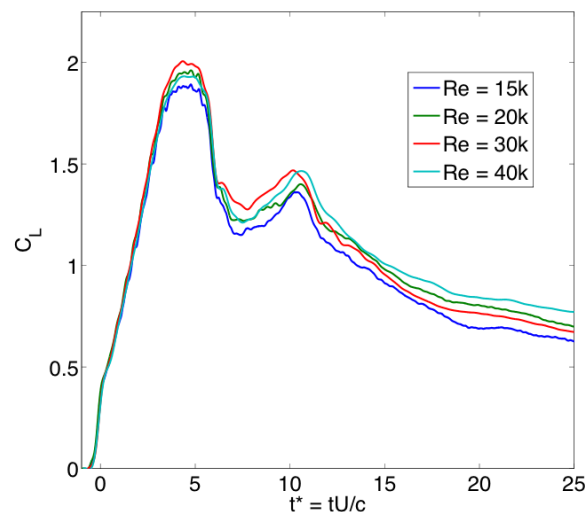
Figure 4-14: AR = 4 Plate Pitching from 0° to 45° in 6 c (Slow Case) for Reynolds Numbers 15 K through 40 K, All in Water (No Addition of Glycerin). Re-variation is obtained by changing test-section free stream speed.

The same trend is seen for the flowfield (Figure 4-15) for the fast translational pitching case, this time over nearly an order of magnitude. Flow visualization is possible at very low dynamic pressures, where direct force measurement becomes problematic, and thus the realizable Re-range is broader. In the false-color rendering, four images (all taken at the ¾-span location) of dye injection from the plate LE and TE are superimposed, with color as proxy for Re. One finds close overlap between the four respective LEVs and the four respective TEVs.
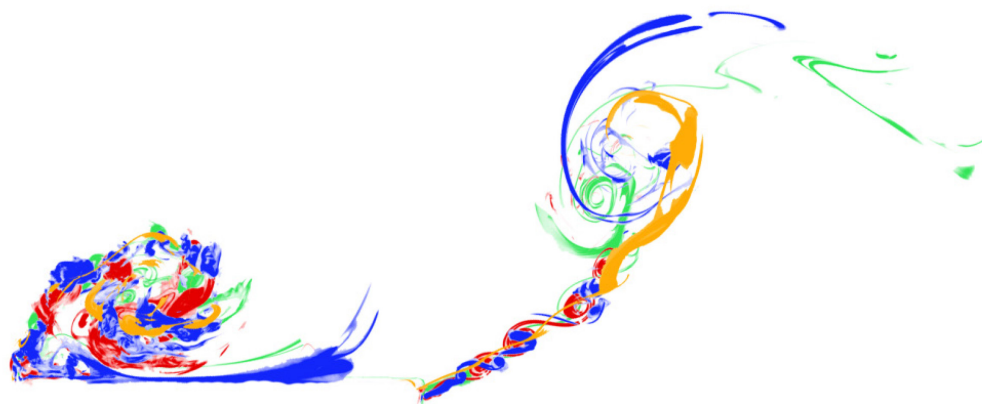
Figure 4-15: False-Coloring of Rhodamine-Dye Planar Laser Fluorescence (that is, Flow Visualization) of the Suction-Side Flowfield of an AR = 4 Plate Pitching from 0° to 45° at Various Re Values, for the "Fast" Case (Pitching Motion Occurs Over One Convective Time; Snapshot is at Completion of One Pitching Motion, by which Time the TEV has Convected ~ 0.7 c Downstream of the Plate's TE).

We now turn to rotation vs. translation. Figure 4-16 shows water tunnel measurements on rotational vs. translational fast surge, at a range of Reynolds numbers, for an AR = 2 plate. Except for very low Re (Re = 60 in Figure 4-16), the net aerodynamic force is normal to the plane of the plate, lift and drag histories follow each other closely (so L/D ~ 1 always) and translation appears to have larger aerodynamic force production than rotation, at least at early-time. Note that the non-zero-acceleration portion of the motion in Figure 4-16 occurs over the first convective time; that is, from $t^* = 0$ to $t^* = 1$. It appears to be the case that for the common choice of θ = 45° incidence angle, the peak L/D remains in the vicinity of 1, regardless of motion rate, for Re >1000 and above.
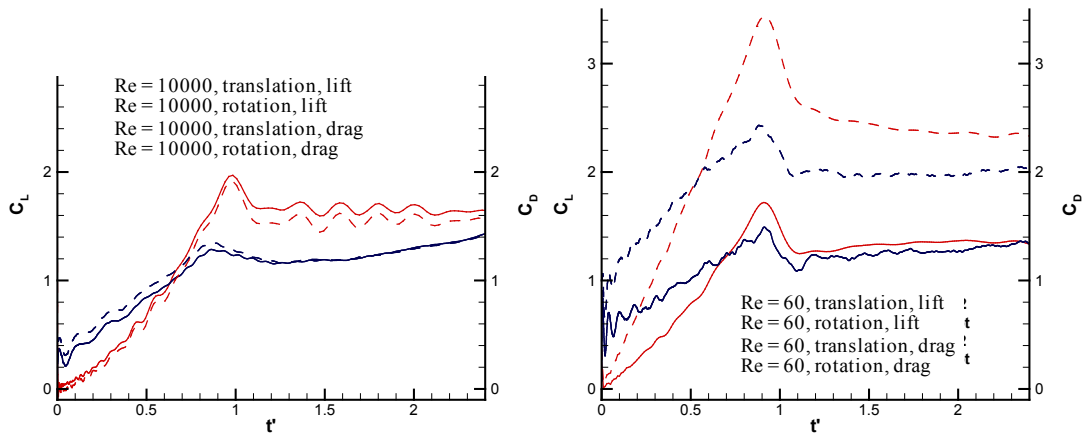
Figure 4-16: Lift Coefficient (Left Ordinate Axis) and Drag Coefficient (Right Ordinate Axis) vs. Convective Time; Lift Coefficient in Solid Lines, Drag Coefficient in Dashed Lines. Translational surge (red), is shown in comparison with rotational surge (black). Left-side plot: Re = 10,000 based on attained steady speed after acceleration concludes; Right-side plot: Re = 60, obtained in mixture of glycerin and water. Lift differs little between Re = 10,000 (left) and 60 (right), while drag at Re = 60 is considerably higher, because skin friction turns the net aerodynamic force aft of wall-normal.

A more comprehensive assessment of Re-effects for fast rotational surge, this time not limited to the early portion of the motion, is shown in Figure 4-17. Here the Re = 120 case (the lowest Reynolds number considered) is something of an outlier, with lower lift than higher values – but between Re = 500 and Re = 10,000 there is little variation.
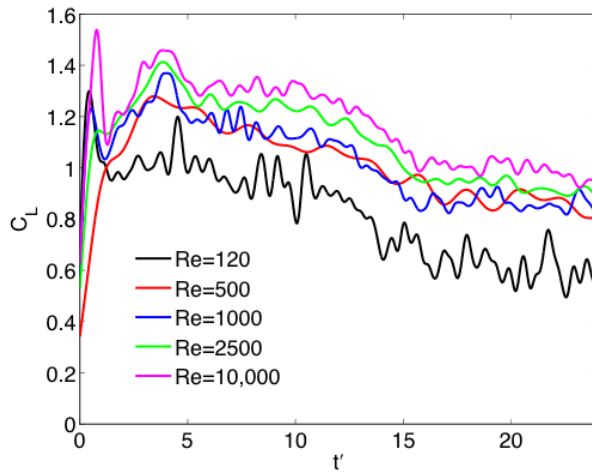
Figure 4-17: Lift Coefficient for a Rotating AR = 2 Plate for a Two Orders of Magnitude Change in Reynolds Number.

We therefore conclude that once Reynolds number reaches a threshold of several hundred, the lift coefficient becomes Re-independent. Drag is somewhat less Re-independent because of the role of skin friction and its

decline with increasing Re. Below this threshold there is some lift variation with Re, depending on the experiment, the style of data-filtering and so forth.

4.3 VARIATION OF REDUCED FREQUENCY

Here we consider the rectilinear (translational) cases, surge and pitch, with the AR = 4 plate. Rotational cases are omitted.

4.3.1 Translational Surge

Variations on the translational surge case, all with 45-degree incidence but with surge acceleration occurring over a duration from $0.25\ c$ through $6\ c$, are shown in Figure 4-18. Reynolds number is 20,000 in all cases, and all relative free-stream speed-profiles are smoothed linear ramps.
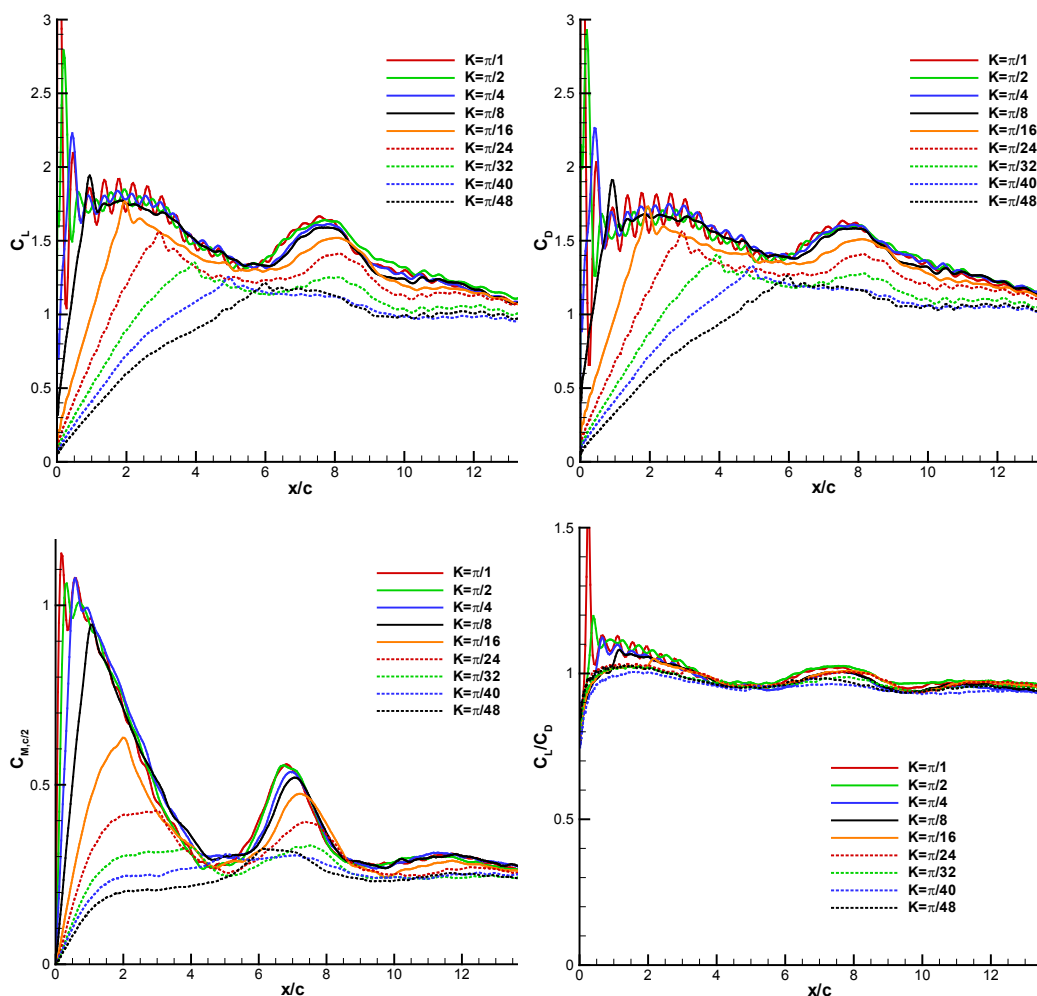
Figure 4-18: Lift Coefficient (Top Left), Drag Coefficient (Top Right), Pitching Moment Coefficient About the Mid-Chord Reference Point (Bottom Left) and Finally Lift to Drag Ratio (Bottom Right) as Functions of Chords Traveled, with Smoothed Linear Ramp of Acceleration from Rest to a Constant Velocity at Re = 20 K, Over Lengths from 0.25 *c* to 6 *c*. AR = 4 rectangular flat plate.

Aside from ramp corner non-circulatory load spikes, and greater apparent oscillations at the highest reduced frequency (where filtering of vibrations will remove the desired frequency content of the actual aerodynamic signal) there is no difference in lift progression when accelerating faster than 1 c (K = π/8); all curves of 1 c or faster collapse atop of each other. For all accelerations, the history of lift (or drag) with respect to chords-traveled is roughly linear while acceleration is non-zero, and once full surging speed is established there is a plateau or a slight decline in lift. This plateau is at CL = 1.75 for 1 c acceleration and above, and progressively smaller for slower surge acceleration. In later time, left declines to a local minimum at 6 c travel, where all curves smoothly increase again until a local maximum at ~ 8 c, and finally gradually diminish again. When accelerating slower than 1 c, a lower maximum lift is achieved, and the local second maximum is attenuated. For all cases, it takes at least 14 chords of travel (beyond the data availability in Figure 4-18) for the various surging acceleration cases to converge towards the same lift value, which is to say to relax to the "steady" (or bluff-body) state. Drag follows lift closely, except for the initial lift-spike at time ~ 0+, as indeed L/D ~ 1 for all other times. Pitching moment coefficient (taken about the mid-chord) follows an undulating history qualitatively resembling that of lift.

4.3.2   Translational Pitch

Here again the peak incidence is 45 degrees. As with all pitch-cases reported here, the starting angle of incidence is zero. Pivot point is the leading edge. Re = 20,000, as in the foregoing section. Besides the two canonical cases ("fast" and "slow"), which are plotted together, we introduce a third case, where the pitch-ramp occurs over two convective times (Figure 4-19). Peak lift declines monotonically with progressively lower pitch rate, as stands to reason, given the respective attenuation in pitch-rate-induced lift. Figure 4-19 also plots lift history vs. a time-base normalized by the pitch rate, so that all motions begin at zero and end at the same value of time. Such overlay shows that the increase in lift due to pitch-rate indeed goes to zero once the motion is completed. The intermediate value of pitch rate also evinces an intermediate value of non-circulatory "bump" associated with the pitch-acceleration start-up transient. This is quite prominent in the fast-case, and absent in the slow one. Looking at the longer-term lift or drag history, it is evident that all cases mutually converge by about 6 – 8 convective time, yet even then the lift (or drag) value is ~ 1.5, which is far above the steady-state or bluff body value.
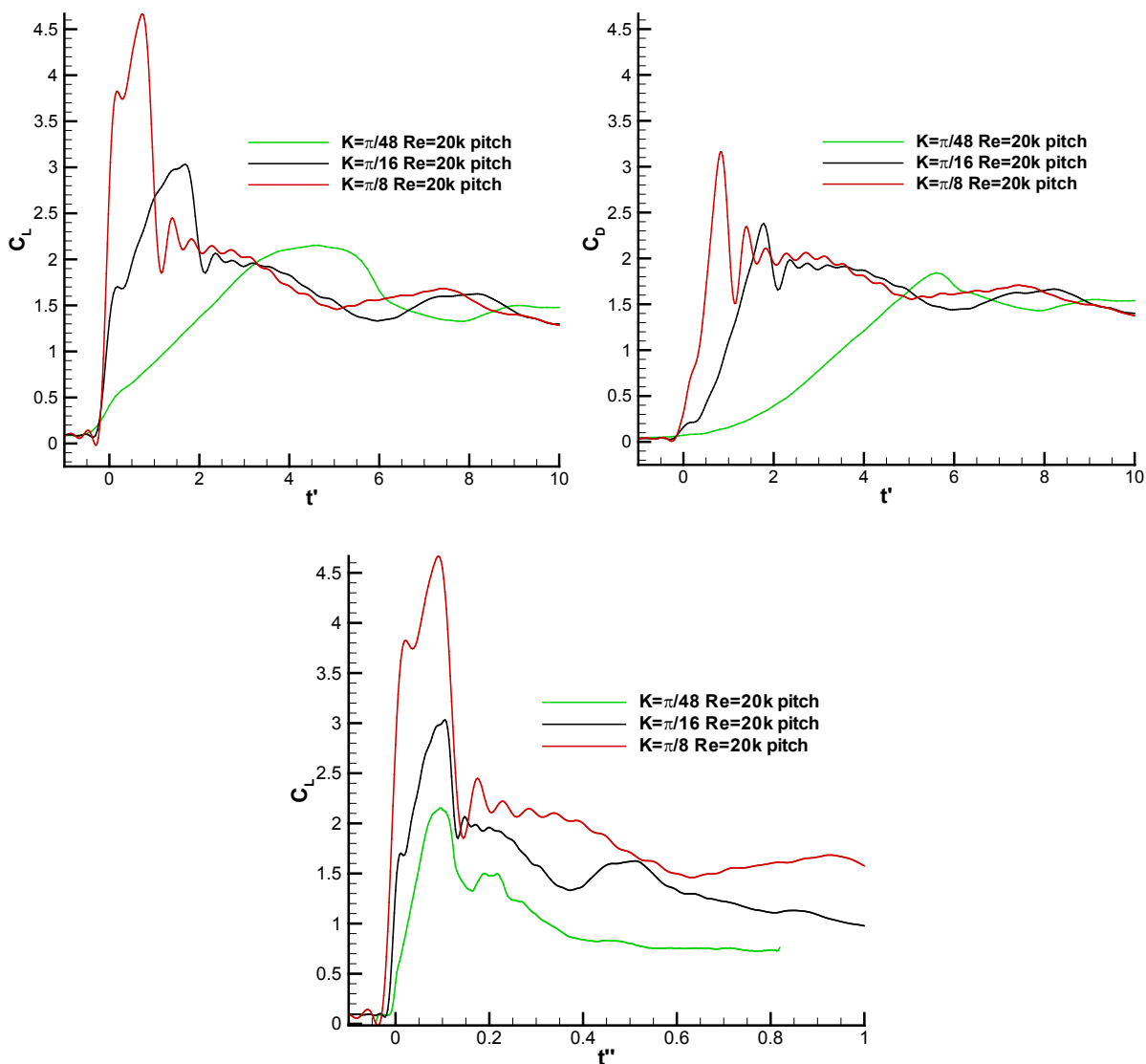
Figure 4-19: Lift and Drag Coefficient Histories for AR = 4 Rectangular Flat Plate at Fast, Intermediate and Slow Pitch Rates; Pivot at Leading Edge, Re = 20 K. Bottom row: Lift coefficient history rescaled by pitch rate.

4.4   VARIATION OF PITCH PIVOT POINT ALONG THE PLATE'S CHORD

In most of this Report, we limit the pitching cases to the leading edge pivot point. In the present section we take five different pivot point locations: x/c = 0, 0.25, 0.5, 0.75 and 1.0. Figure 4-20 presents the 1 c case, while Figure 4-21 presents the 6 c case. Clearly, pivot point effects are much stronger for the faster pitch rate. The differences in lift are more profound than in drag. Differences in circulatory lift are primarily a steady offset and not a slope change, and are ascribable to the "Magnus effect".
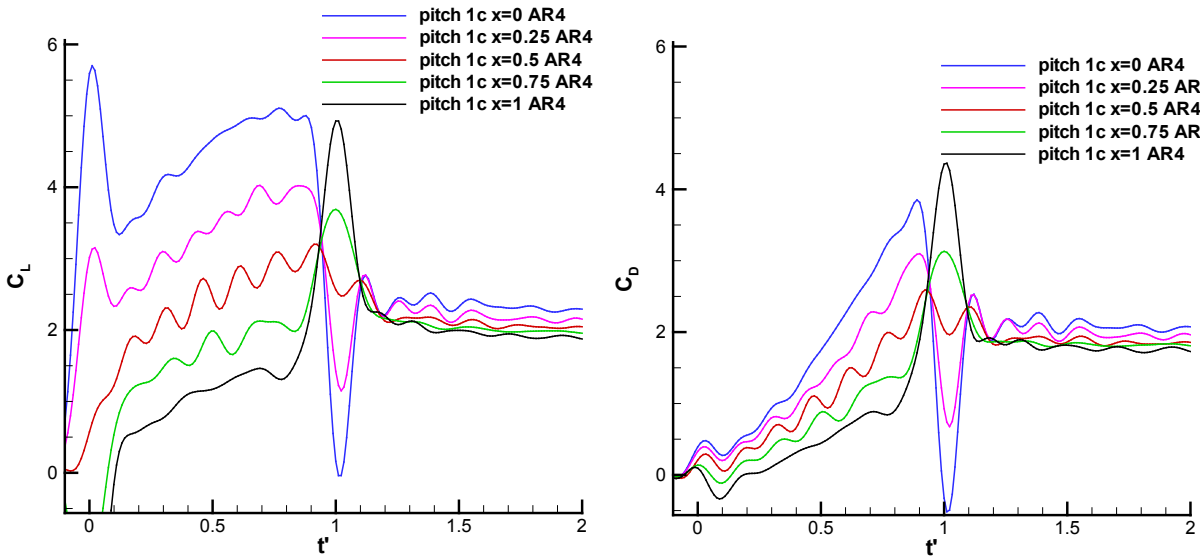
Figure 4-20: Pivot-Point Effects for Pure-Pitch Cases, 1 *c* Motion, AR = 2 (Top Row), AR = 4 (Middle Row) and Nominally 2D (Bottom Row); Lift (Left Column) and Drag (Right Column). Pivot point at leading edge (x/c = 0), x/c = 0.25, 0.5, 0.75 and 1.0 (trailing edge).
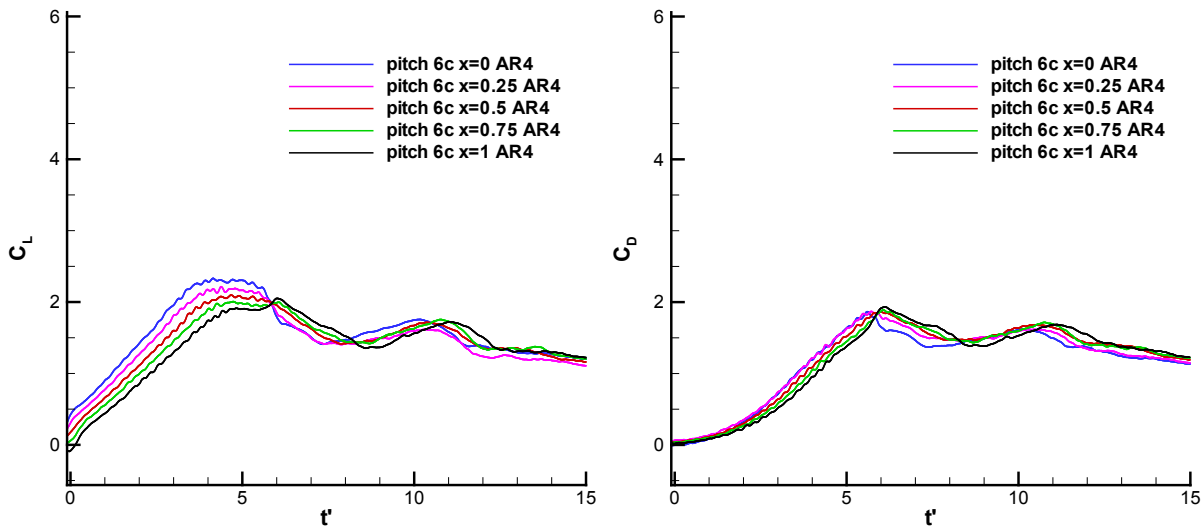
Figure 4-21: Pivot-Point Effects for Pure-Pitch Cases, 6 *c* Motion, AR = 4. Lift (left column) and Drag (right column). Pivot point at leading edge (x/c = 0), x/c = 0.25, 0.5, 0.75 and 1.0 (trailing edge).

For the fast case, differences in non-circulatory lift are quite obvious, and are qualitatively consistent with the implications of the low-order model proposed in this Report. With the pivot point maximally upstream, there is a positive non-circulatory lift spike when pitch-acceleration is positive (early in the motion history), and a negative spike in both lift and drag when pitch-acceleration is negative (t'~ 1). For pitch about the mid-chord, there is no non-circulatory contribution, arguing from symmetry. For pitch about a point downstream of the mid-chord, the sign of the force spike reverses: negative spike in lift when acceleration is positive, positive spike in lift and drag with acceleration is negative.

For the slow case, (Figure 4-21), a more upstream pivot point also produces higher peak lift due to a constant positive offset, but now the acceleration is too slow to produce a demonstrable non-circulatory force contribution in any of the motions. We mention in passing that peak lift for the $x/c = 0$ pivot-case appears to occur when t'~ 4; that is, at a time from motion onset during which the free-stream has traveled approximately 4 chords. The offset between the five lift curves in Figure 4-21 can be regarded as an offset in the abscissa alternatively as an offset in the ordinate. Considering the former, each curve differs from its neighbor by t'~ 0.25 – that is, by approximately the difference in pivot point location. It therefore appears that if the pivot point is taken as an origin, in all cases peak lift is achieved when the free-stream has convected downstream through a distance of 4 chords past the pivot point. One is tempted to wonder whether this is coincidental, or relatable to the oft-quoted conceptualization of a critical "formation number" of 4 [51].

4.5 VARIATIONS IN ACCELERATION PROFILES

Nearly all of the motions studied in this Report are smoothed linear ramps. Smoothing is at the ramp-corners, which is to say at motion initiation and cessation. Here instead we vary the acceleration profile according to an exponential equation. For an analog of the slow translational surge case (6 chords), we have:

$$u(t) = \begin{cases} kt^n & x/c < 6 \\ U_\infty & x/c \geq 6 \end{cases}, \quad k = \frac{U_\infty}{t_a^n}, \quad t_a = \frac{(n+1)6c}{U_\infty} \tag{Eq. 4-1}$$

These kinematics are shown in Figure 4-22. For the same acceleration distance, early higher acceleration (fuller velocity profile) produces a higher lift coefficient throughout the acceleration phase. The coefficient *n = 1* recovers the standard case. In Figure 4-23, we instead use a different normalization scheme, where the dimensional lift is normalized by instantaneous dynamic pressure, instead of the dynamic pressure comporting with the steady-state relative free stream. Lift coefficient is initially infinite, since initial velocity is zero. During the first chord of travel, for faster accelerations, lift reduces at a faster rate than for slower accelerations. At $s/c = 2$, all curves collapse, and lift is now independent of acceleration until s/c ~ 5.5, which nears the end of the acceleration phase. For $s/c > 6$, all five cases have the same constant velocity and are thus normalized the same way as in Figure 4-22. Initially in the motion, we have a formation of a leading edge vortex, and at some chordwise travel presumably the LEV is considered to be detached. This is where the curves collapse. At s/c ~ 6, a new LEV forms and the curves diverge based on the strength of the 2nd LEV, which in turn is dependent on the strength of the 1st-formed LEV.
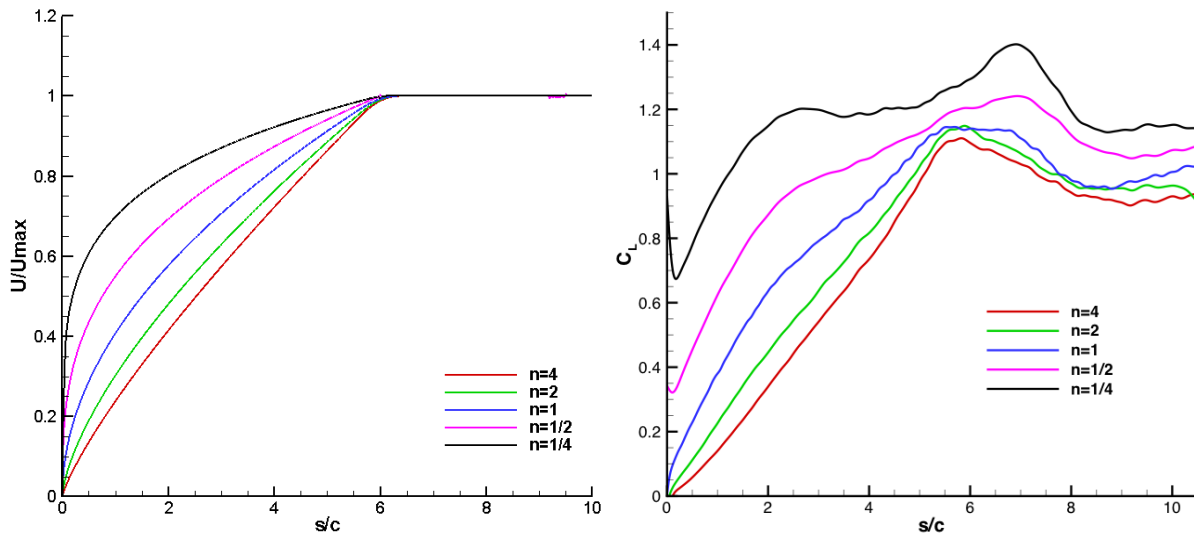
Figure 4-22: Velocity Profiles (Left) and Lift Coefficient (Right) for an AR = 4 Plate at θ = 45° Accelerating Over 6 Chords to Constant Velocity with Five Different Acceleration Profiles.
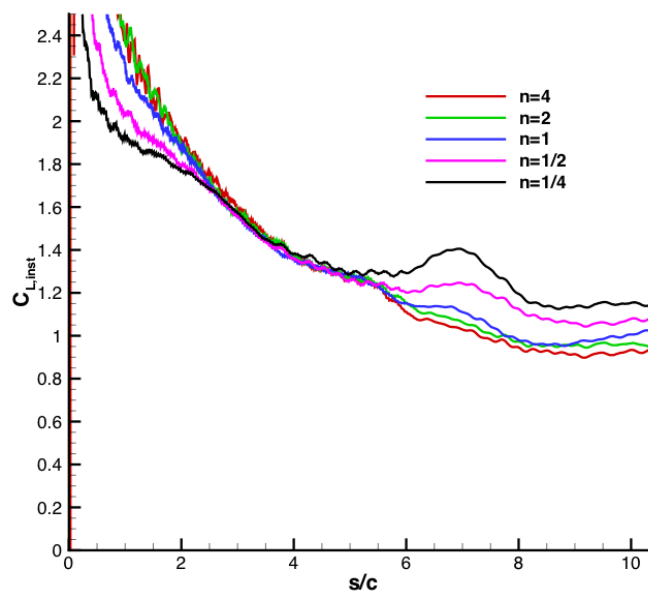
Figure 4-23: Lift Coefficient Normalized by Instantaneous Dynamic Pressure for AR = 4 Plate at θ = 45° Accelerating Over 6 Chords to Constant Velocity with Five Different Acceleration Profiles.

4.6   VARIATIONS IN TRANSLATIONAL KINEMATIC MODALITY: PLUNGE, SURGE, AND PITCH-SURGE

Here we consider two lines of investigation. The first is based on Kriegseis *et al*. [52], and is concerned with a plunging motion in a steady free-stream, yielding an angle of attack history following that of a pitch-ramp.

Emphasis is on vortex transport. The second topic is comparison of lift and drag history between pitch, surge, plunge, and the combined motion of pitch-surge. All cases are translational.

4.6.1   Vortex Dynamics for Surge vs. Plunge

For the first topic, the question is one of long-term significance of initial conditions. In a surge, the starting-case has zero flow, and obviously there are no boundary layers yet. Boundary layers and the associated vorticity production form after the motion starts. In an "equivalent" (in the quasi-steady sense) plunging motion, there is already an established free-stream, and therefore boundary layers. The motion alters the extant boundary layers and presumably affects the accumulation and ejection of vorticity.

To study the influence of initial conditions, we compare:

1) Surging (acceleration) of a plate from rest at a constant angle of attack to a final towing speed.

2) Perturbation of a developed boundary-layer flow on a flat plate with a sudden cross-stream plunging motion superimposed onto a constant free stream velocity.

These two cases will henceforth be referred to as surging and plunging, respectively, as shown in Figure 4-24. In order to contrast these two cases, the two main relevant characteristic velocities – free stream velocity and effective shear-layer velocity – must be considered in the development of vortex circulation.
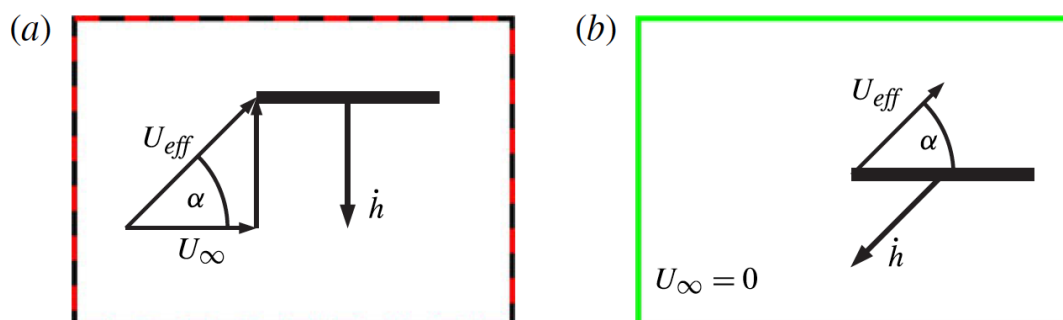
Figure 4-24: Kinematics Used in this Study. (a) Plunging case(s): Plunge with effective velocity of 0.1 m/s (P45 0.1, red) and with effective velocity of 0.07 m/s (P45 0.07, black); (b) Surging case: Surge to 0.1 m/s (T45 0.1, green).

When examining these characteristic velocities, on the one hand, it is known that the feeding shear layer controls the growth and thus strength of LEVs through the flux vorticity-containing mass into the LEV. Therefore, the advection of circulation into the LEV is a function of the shear layer, with the effective velocity as the only characterizing velocity measure. This suggests that one should define the kinematics of surge and plunge with identical effective shear-layer velocities for proper comparison. On the other hand, one could argue that the characteristic velocity to compare surging and plunging plates is the free stream velocity to ensure an identical bulk Reynolds number for all cases.

Consequently, both characteristic velocities will be considered in the present study in order to clarify this issue. Subsequently, the influence of initial conditions on vortex growth will then be studied for both near-mid-plane and near-tip regions.

LEV circulation histories in the near-mid-plane region for all three test cases are compared in Figure 4-25. In Figure 4-25(a) the non-dimensional circulation and convective time are normalized with the free stream velocity, which corresponds to the final tow speed for the towing case. Owing to the additional boundary-layer vorticity, one would expect a constant offset for the circulation histories between the plunging case P45_0.1 and the towing case T45_0.1, as sketched in Figure 4-25(a). However, the difference between both plunging cases and T45_0.1 shows a larger offset. In order to explore the cause of this larger offset, the free stream velocity is replaced with the effective shear-layer velocity U_{eff} to normalize circulation and time, in Figure 4-25(b). This is particularly sensible since the vortex growth rate is determined by both the generation of vorticity and advection of circulation at the leading edge, each of which is limited by U_{eff}. The non-dimensionalization used in Figure 4-25(b) reveals a collapse for the two plunging cases together (P45_0.1 and P45_0.07) with the towing case T45_0.1. Despite the varying initial conditions between plunging and towing, it must be concluded that the initial boundary-layer vorticity, at least in the near-mid-plane region, plays little role in the vortex formation process. In other words, the initial layer of vorticity must be rapidly annihilated with an opposite-signed layer on the plate surface once the motion begins. Therefore, it has to be concluded that rapid acceleration of fluid boundaries (e.g., moving or morphing obstacles) accelerates fluid with opposite-signed vorticity towards an existing boundary layer, which leads to the sudden cross-annihilation of the two vorticity layers.
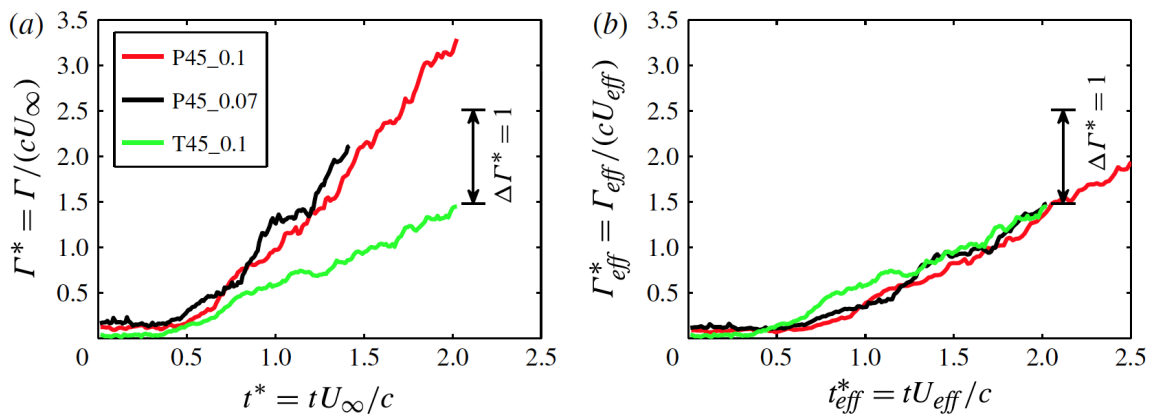
Figure 4-25: Near-Mid-Plane Circulation and Convective Time Normalized with Freestream Velocity (a) and with Effective Velocity from the Shear Layer (b). Note P45_0.1 and P45_0.07 represent two identical plunging cases with differing Reynolds numbers while T45_0.1 is the equivalent surging case.

Both findings – a collapse of circulation and loss of memory of initial conditions – are confirmed by LEV formation plots: Figure 4-26 shows the temporal evolution and corresponding spatial distribution of spanwise vorticity for the near-mid-plane region (**XY**-plane) of all three cases. The iso-lines reveal a similar growth of the LEV for all three cases, which reaffirms the insights obtained from the circulation plots of the near-mid-plane region as shown in Figure 4-26. However, after the acceleration of the plate stops, it can be observed that the tow case LEV starts to roll off the plate. Despite identical circulation, as demonstrated in Figure 4-26, this beginning roll-off might adversely affect the resulting magnitude of the lift force for the towing case. It is important to note that the plate-fixed frame of reference in fact is an accelerated reference frame. As such, the (attached) vortical structures are accelerated according to the orientation of the respective plate kinematics in an inertial system. It is therefore hypothesized that the remaining inertia of the accelerated fluid causes the roll-off of the tow case LEV once the plate acceleration stops.
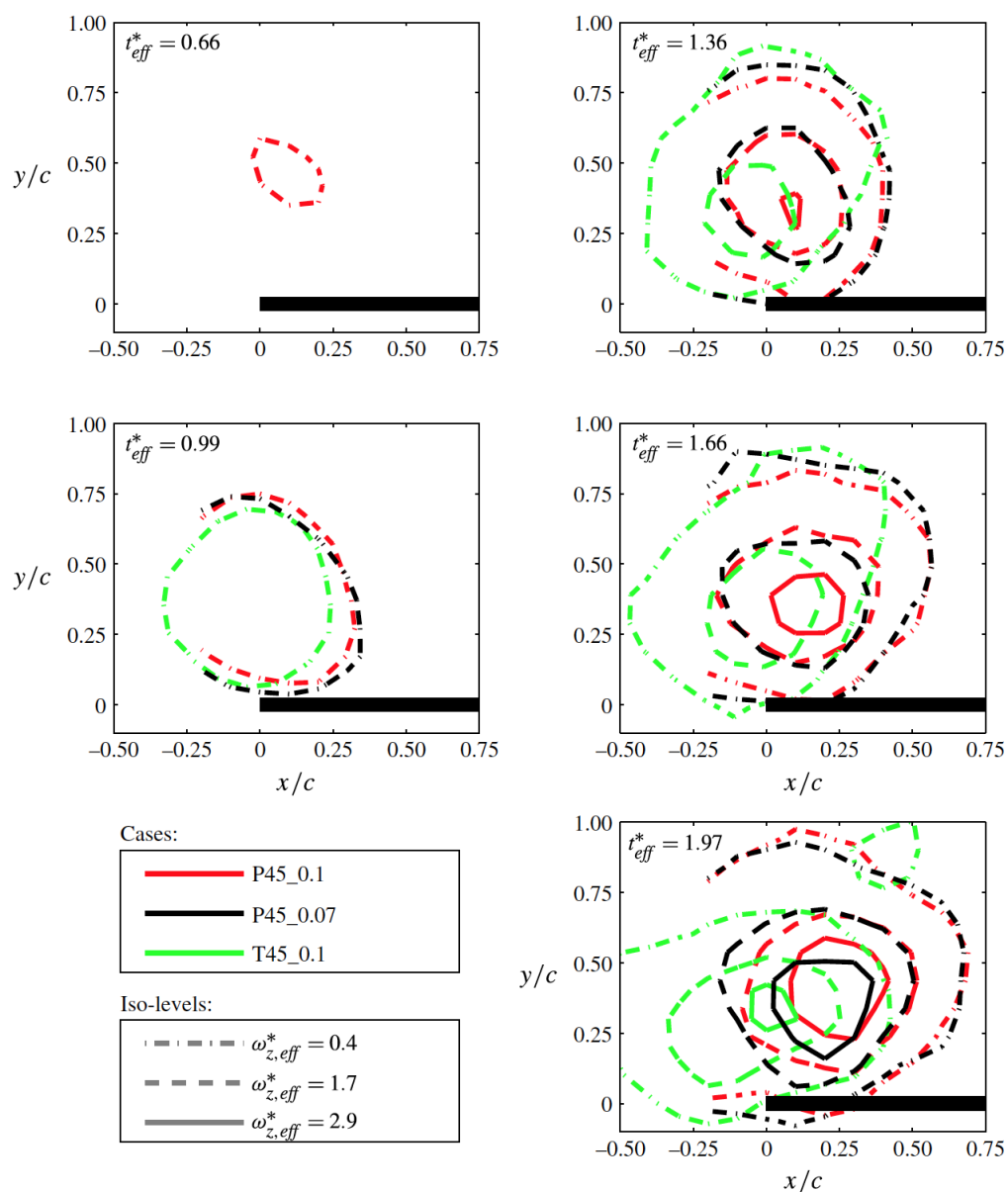
Figure 4-26: Vortex Positioning During Key Time Steps Between Plunge and Surge.

It has been demonstrated that the circulation history in the near-mid-plane region is identical for both plunging cases and T45_0.1. The corresponding total force results are shown in Figure 4-27. Here, lift and drag forces are defined to be perpendicular and parallel to the direction of the plate velocity, respectively (upper row). In addition, C_y and C_x representing the plate-normal and plate-parallel forces are plotted for comparison, respectively (lower row). All force data are non-dimensionalized based on the standard convention on the left but also using U_{eff} on the right.
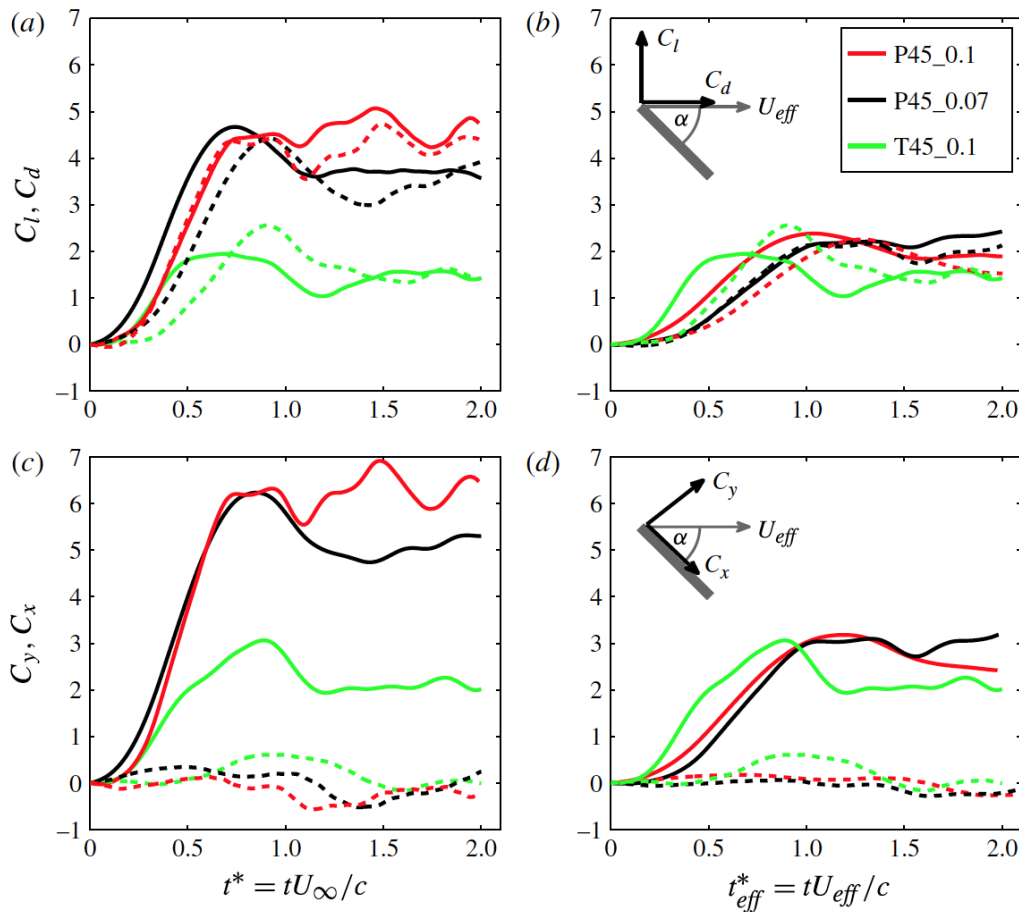
Figure 4-27: Force Coefficients Normalized on Freestream and Effective Velocities.

First, it is worth noting that the curves for the plunging motions show unexpectedly high values when normalized with the freestream velocity. In particular, the force magnitudes for T45_0.1 and P45_0.07 should be similar since the LEV is fed with the same shear-layer velocity at identical effective angles of attack. This discrepancy confirms the validity of U_{eff} as the characterizing velocity scale to describe vortex growth and thus resulting forces.

Furthermore, it is remarkable that the force histories of both plunging cases (P45_0.1 and P45_0.07) share identical curves during the plate acceleration despite the fact that they experience different magnitudes of acceleration during the respective plate motions. In contrast, the slow plunge and the tow case (P45_0.07 and T45_0.1) obviously yield significantly different force histories, even though in both cases the magnitude of plate acceleration was identical.

4.6.2   Lift and Drag for a Range of Kinematics

Here we compare four translational motions: pitch, surge, a combined "pitch-surge" and finally an "equivalent" plunge. The plunge follows rationale from the previous section, and is scaled purely by $\theta = \mathrm{atan}(\dot{h}/U_\infty)$, from which one obtains the plunge-history. This disregards the pitch pivot point effect – a crucial issue.

"Pitch-surge" begins at zero incidence with no relative free stream, and begins simultaneous increase in relative free-stream and incidence angle, both by smoothed linear ramps, until reaching the usual steady-state. The result for the 1 *c* motion is shown in Figure 4-28 with focus on early-time history, and in Figure 4-29 for the long-term history. Figure 4-30 covers the slow-case (6 *c* acceleration), where unfortunately plunge is not possible because at the low rate, the resulting vertical (plunge) displacement is not kinematically realizable in the facility where the experiment was conducted. The purely-pitching and the pitching-surging cases are again with respect to a pivot point at the leading edge (x/c = 0).
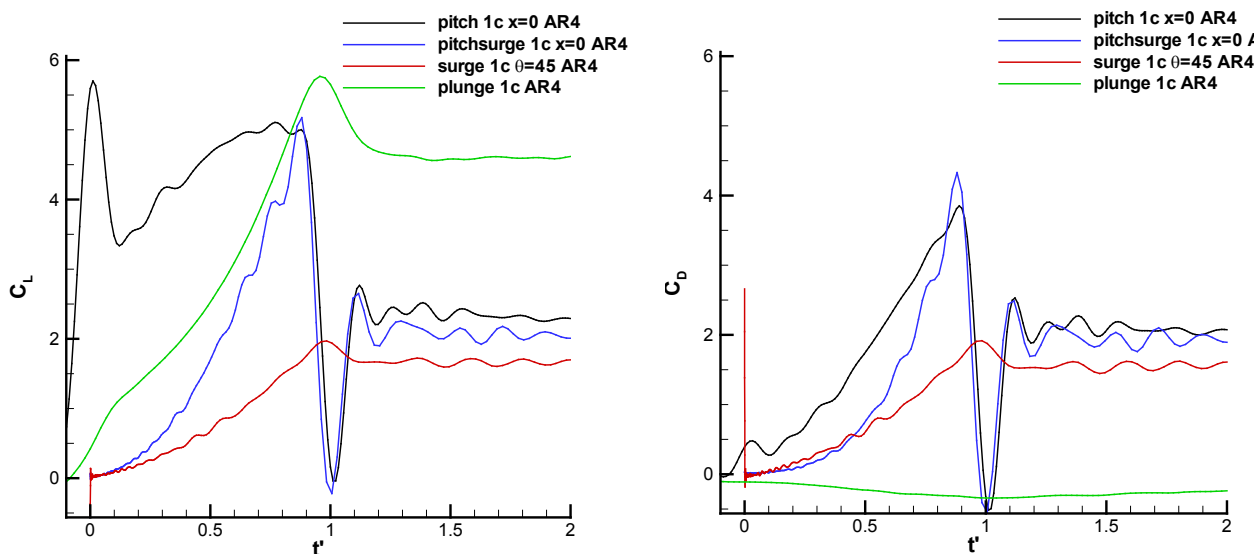
Figure 4-28: Comparison of Pitch Ramp, Pitch-Surge Ramp and Pure Surge-Ramp, 1 *c* Motion, AR = 4 Flat Plate; Lift (Left Column) and Drag (Right Column). Pivot point is at the leading edge (x/c = 0) for the pitch-ramp and pitch-surge ramp.
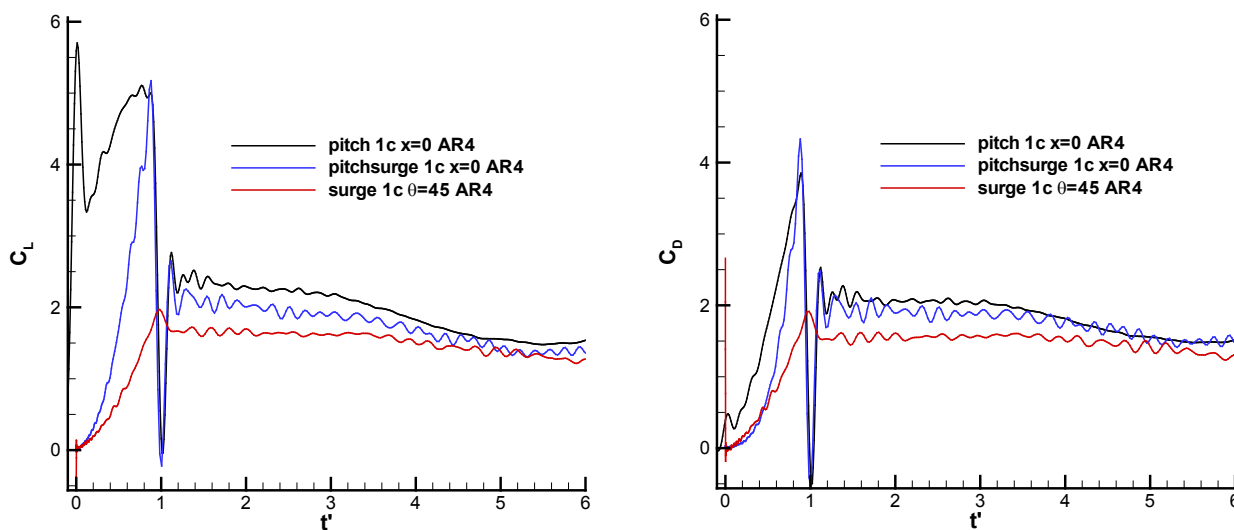
Figure 4-29: Long-Term History of Lift and Drag for AR = 4 1 *c* Motion Comparison.
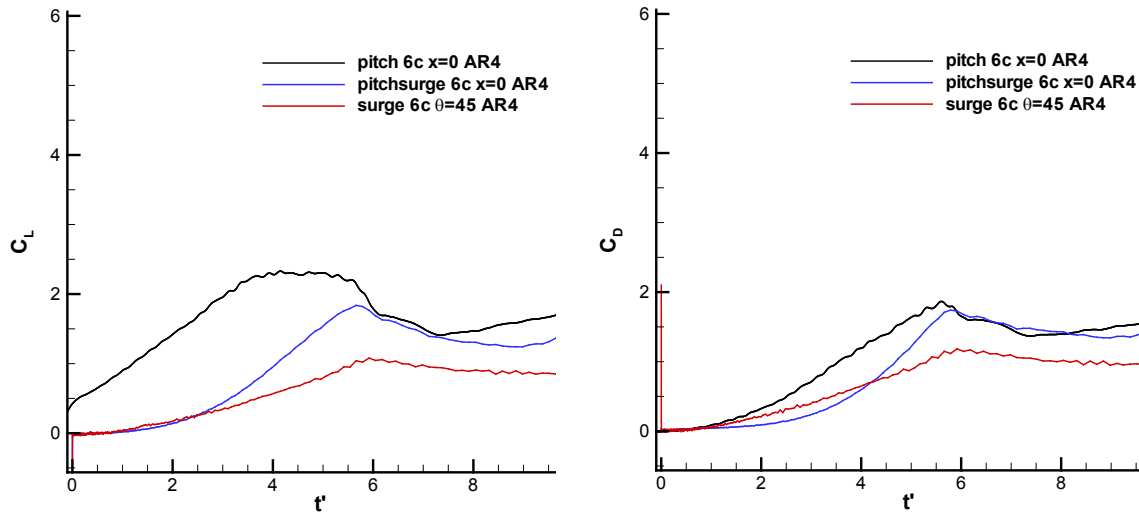
Figure 4-30: Comparison of Pitch Ramp, Pitch-Surge Ramp and Pure Surge-Ramp, 6 *c* Motion, AR = 4 Only; Lift (Left Column) and Drag (Right Column). Pivot point is at the leading edge (x/c = 0) for the pitch-ramp and pitch-surge ramp.

Pitch and plunge are mutually irreconcilable, owing to the aforementioned Magnus effect of pitch-rate. The pitching case has much higher lift and drag than does the respective surging case, for both motion rates. The combined pitch-surge ramp is an intermediate case, as is to have been intuitively expected. Early in the motion, (t' ~ 0), it behaves akin to the surging case, with aerodynamic force production attenuated due to low dynamic pressure. As time proceeds, the pitch-surge case comes to approximate the purely pitching case. The plunging case has a lift history somewhere in between that of the pitching and pitch-surge cases, but a drag history altogether different, with drag outright negative, evidently from strong leading edge suction. It, and the pure-surging case, completely lack a non-circulatory lift or drag spike.

4.7   VARIATIONS IN PLATE LEADING EDGE SHAPE

Here we consider the effect of using different leading and trailing edge geometries in fast and slow translational pitch, based on force measurements and PIV conducted at ITU. Because the plate is vertically suspended in a free-surface water tunnel, aerodynamically the plate is "mirrored" about the free-surface, depending on how the free-surface boundary condition is enforced: with or without an endplate, and with the plate submerged below the free-surface, or not. The following discussion, in addition to comparing the round leading edge with a squared-off or "sharp" leading edge, also considers this mirroring effect. Figure 4-31 presents lift coefficient history for the slow case, while vorticity contours, superimposed on planar projection of streamlines, are in Figure 4-32. Data in Figure 4-32 are for the AR = 4 plate, which is actually a physical aspect ratio of 2, with the mirroring effect included.
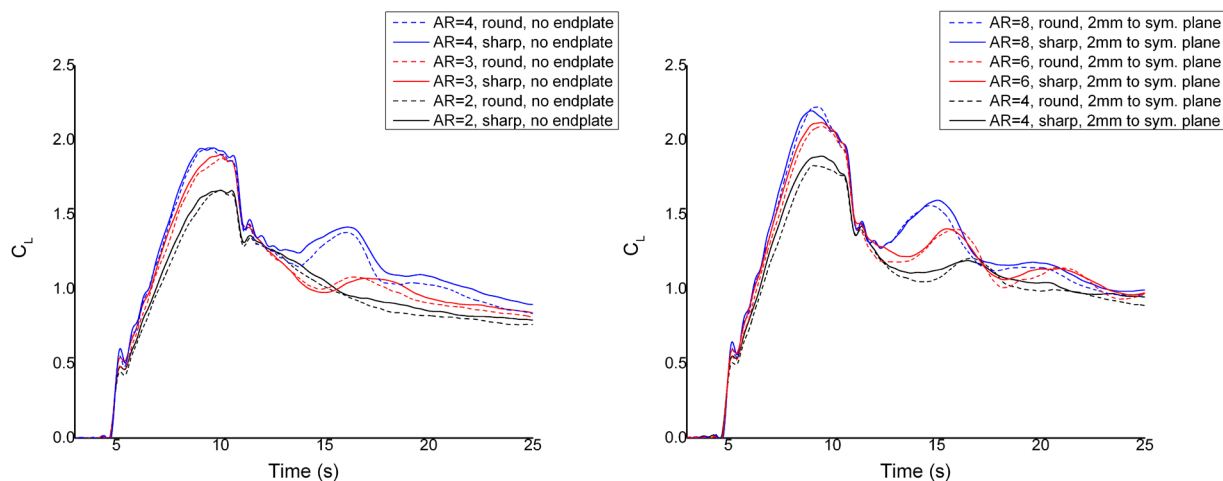
Figure 4-31: Lift Coefficient Histories for the Slow Translational Pitch Case, for Plates of Sharp and Round Leading Edge, Without (Left) and With (Right) Enforcement of a Symmetry-Plane Condition.
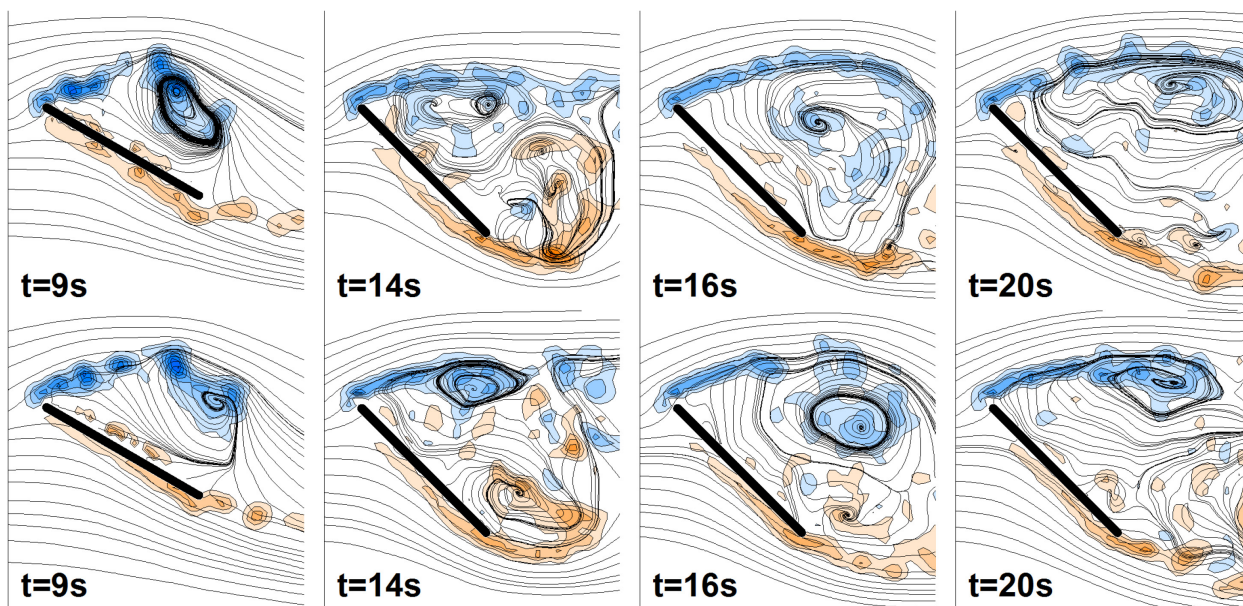
Figure 4-32: PIV Sectional Slices of Vorticity for the AR = 4 Plate: Sharp Edges (Top Row) and Round Edges (Bottom Row); Slow Translational Pitch.

Similarly, fast translational pitch lift coefficient histories are in Figure 4-33, and PIV vorticity contours and superimposed streamlines for the AR = 4 plate are in Figure 4-34. While the details of projected streamline placement are very sensitive to minor variations, overall flowfield feature evince little difference between the sharp-edge and round-edge variants of the same aspect ratio. Differences in lift coefficient history are even smaller. Evidently, leading edge shape, or edge shape in general, makes very little difference in these separated flows. Aspect ratio however does have a demonstrable effect, as already noted in a prior section.
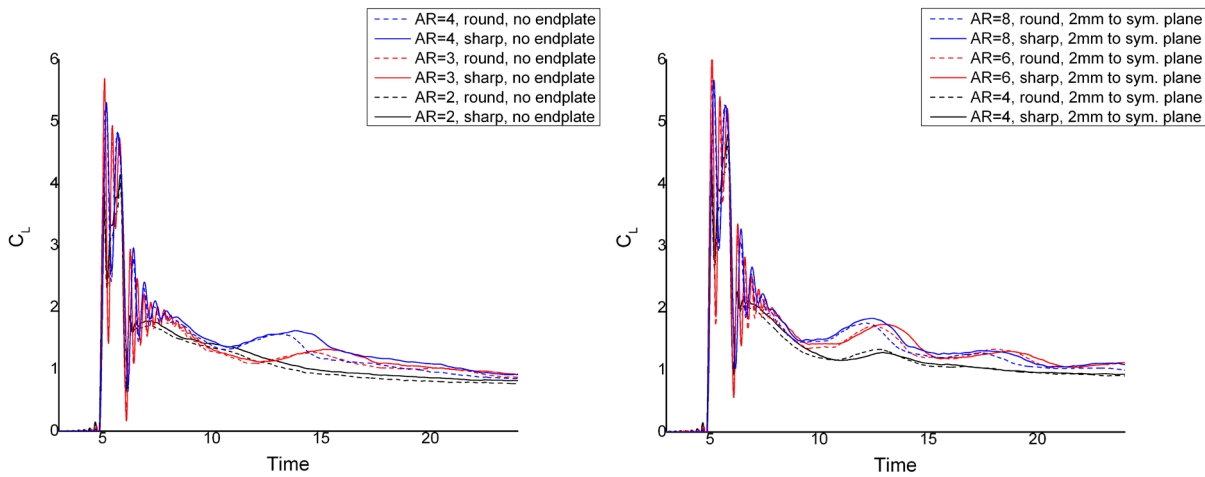
Figure 4-33: Lift Coefficient Histories for the Slow Translational Pitch Case, for Plates of Sharp and Round Leading Edge, Without (Left) and With (Right) Enforcement of a Symmetry-Plane Condition.
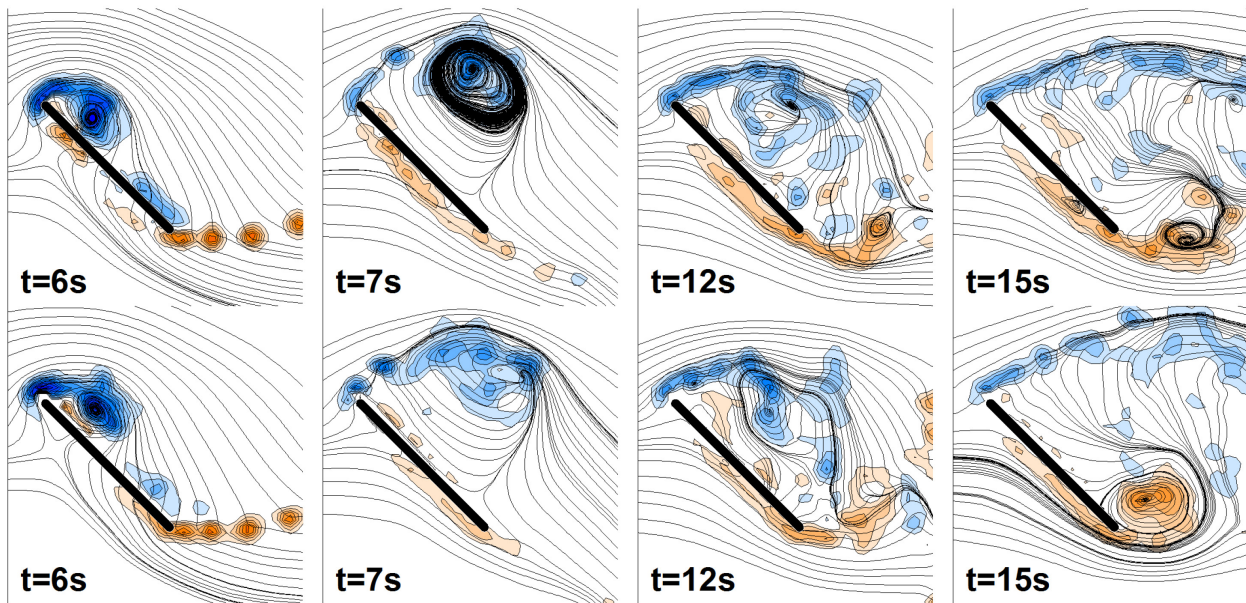
Figure 4-34: PIV Sectional Slices of Vorticity for the AR = 4 Plate: Sharp Edges (Top Row) and Round Edges (Bottom Row); Slow Translational Pitch.

4.8   VARIATIONS IN PEAK INCIDENCE ANGLE

Here we consider two parameter studies for the surging plate – translational and rotational, in both cases with the "fast" acceleration profile of a linear ramp over 1 c.

4.8.1   Translational Surge

Figure 4-35 covers a range of incidence angles from 5 to 90 degrees, in all cases with the same smoothed linear surge ramp over 1 c, and in all cases the respective incidence angle held constant. The low incidence case is expected to have lift coefficient follow Wagner's model [53], and for $\theta = 5\,\pi$ the agreement is quite good [54].
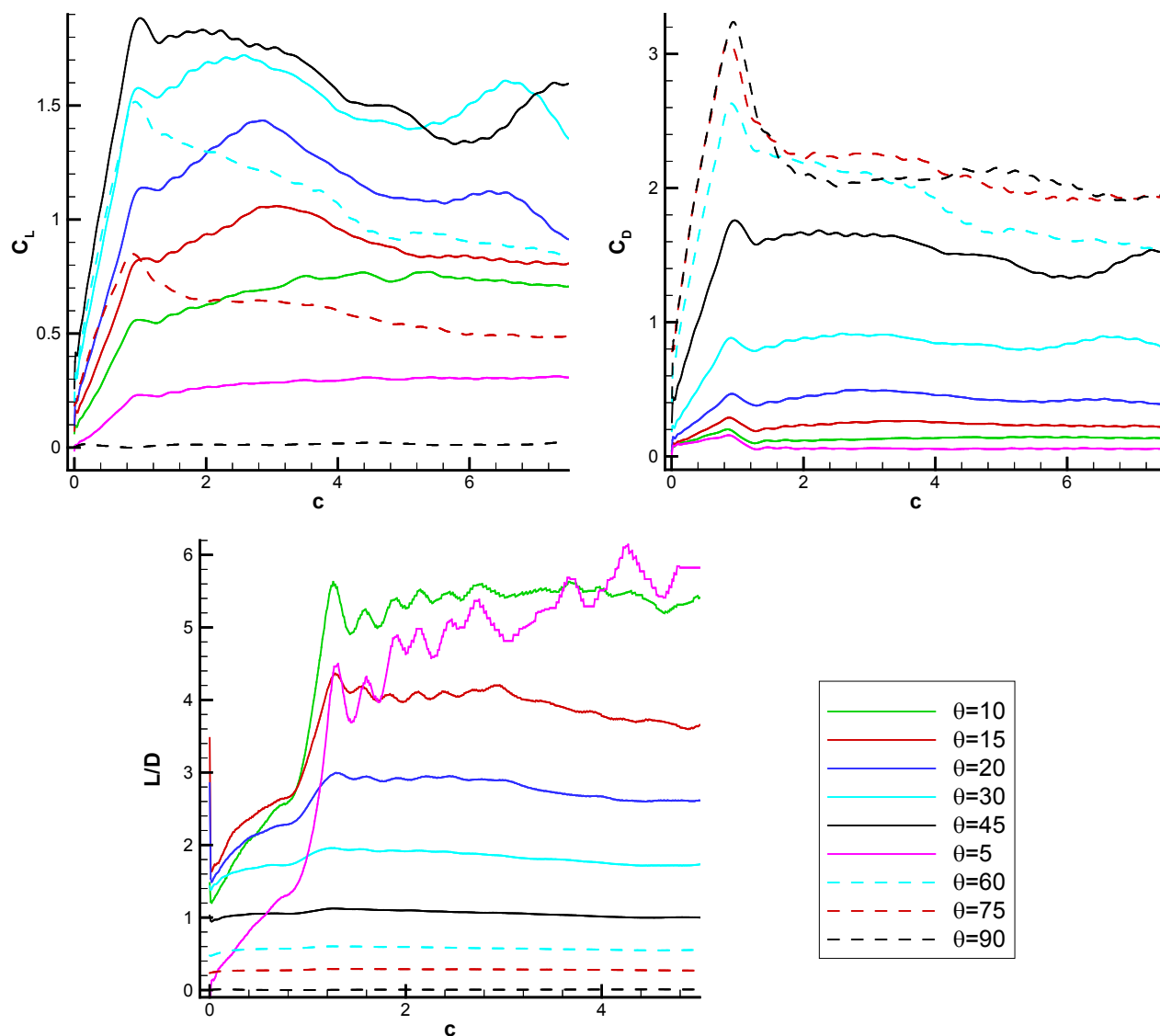
Figure 4-35: Incidence-Angle Sweep (5, 10, 15, 20, 30, 45, 60, 75 and 90 degrees) for the Fast Surging Case, Re = 20,000. Lift (top left), drag (top right), and lift-to-drag ratio (bottom). For θ = 45°, lift and drag histories essentially coincide, because the net aero force is plate-normal. For θ = 90° the lift is of course zero, and the plate acts like a piston. For all cases, peak loads are evident at the conclusion of the acceleration. The flow is separated in all cases, even (slightly) at θ = 5°; never is there any appreciable leading edge suction. However, for θ = 5°, L/D climbs after the acceleration is over, resembling a Wagner-like rise as bound circulation attains its steady-state value. For higher incidences, L/D peaks towards the conclusion of the motion. For θ = 45°, L/D ~ 1 perpetually.

4.8.2 Rotational Surge

This section covers PIV measurements for the fast rotational surging case by the TU Delft group for the AR = 2 plate, comparing incidence angles of 30 π and 60 π with the canonical case, 45 π. Flowfield data are presented as evolution vs. chords-traveled, at the radius of reference from the point of rotation. 3D iso-surfaces of Q2-criterion are shown in Figure 4-36 and Figure 4-38, while 2D contours of vorticity are shown in Figure 4-37 and Figure 4-39. Most notable is the striking qualitative similarity in flowfield between the three incidence-angle cases, and the persistence of the LEV-tip vortex pair throughout the motion history. These results are consistent with those of Wolfinger and Rockwell [16], and Garmann and Visbal [55].
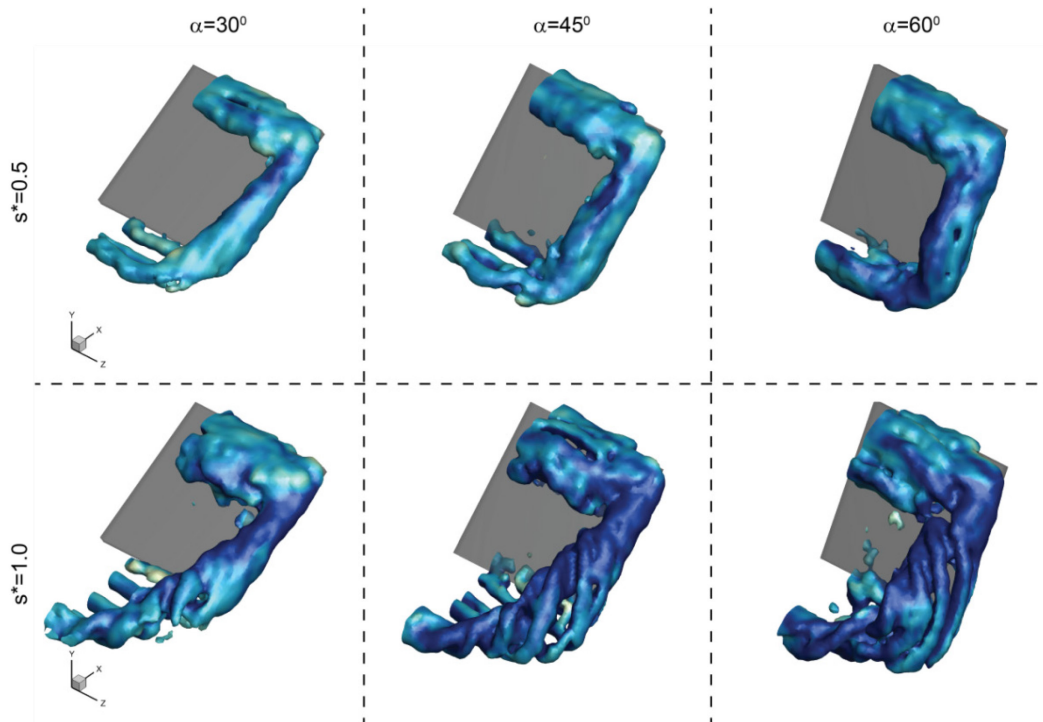
Figure 4-36: Iso-Surfaces of Normalized Q₂-Criterion, $Q/(V_t/c)^2 = 3.125$ Colored by Vorticity Magnitude; Early Time After Onset of Rotational Surge, Fast Case, Incidence Angles as Marked. Data from TU Delft Group.
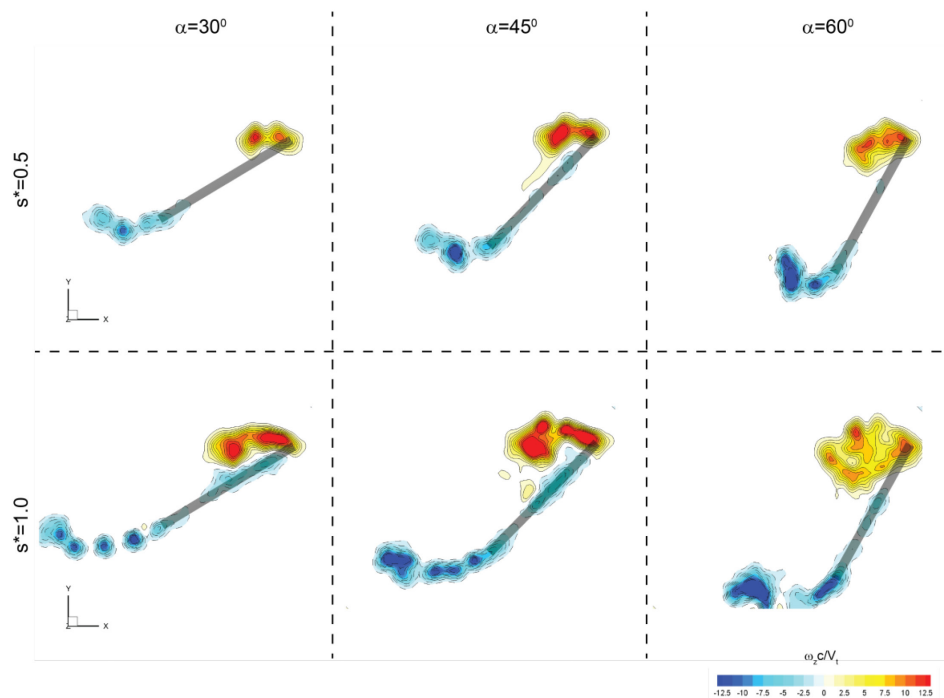
Figure 4-37: 2D Analog of Figure 4-36; Contours of Non-Dimensional Out-Of-Plane Vorticity ($\omega_z c/V_t$) in the Reference Plane, Fast Rotational Surge Case, Incidence Angles and Chords-Traveled as Marked.
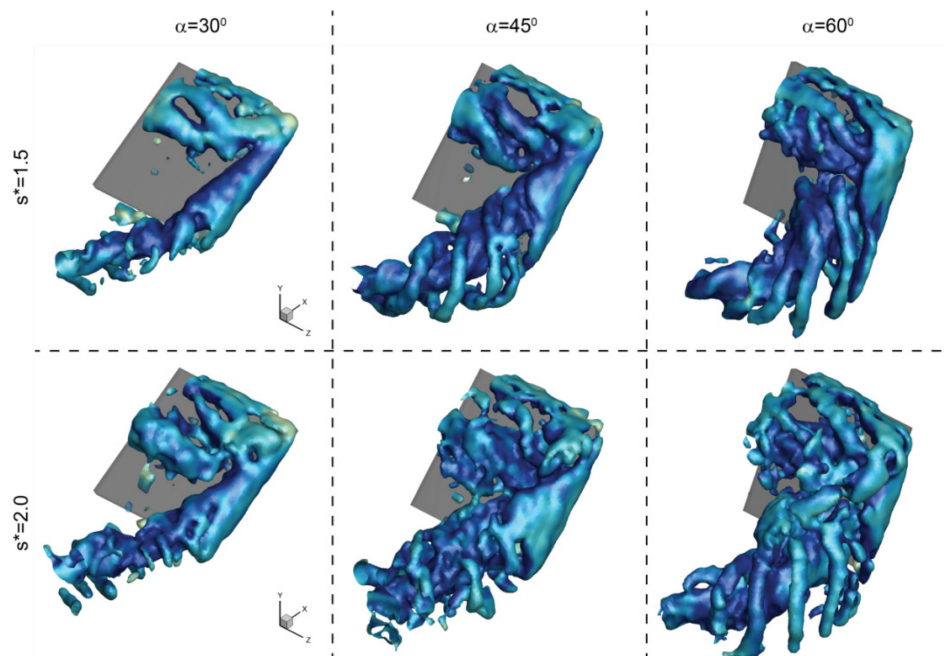
Figure 4-38: Continuation of Figure 4-36 to Later Time (that is, Later Number of Chords-Traveled at the Reference Plane); Iso-Surfaces of $Q/(V_t/c)^2 = 4.68$, Colored by Vorticity Magnitude.
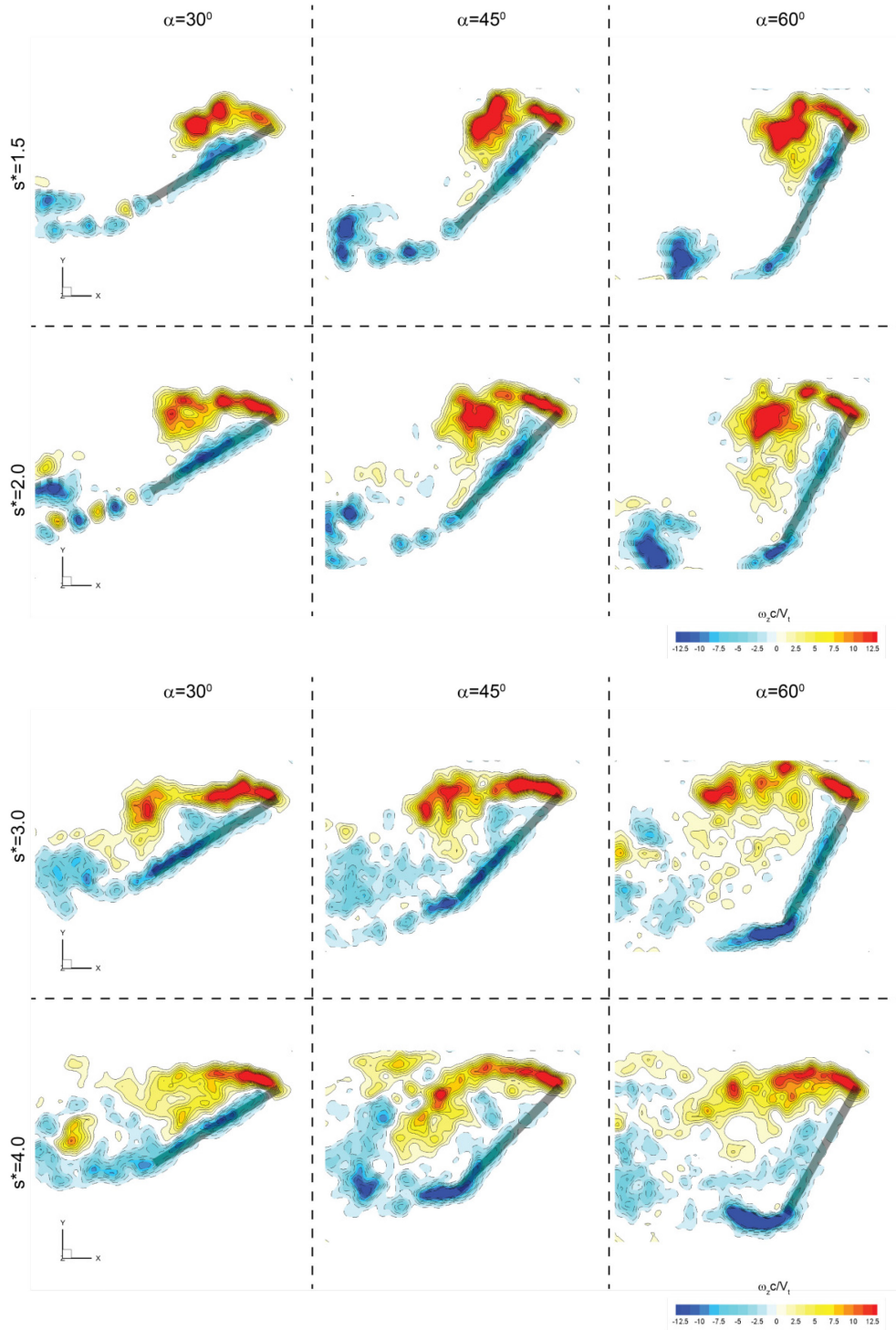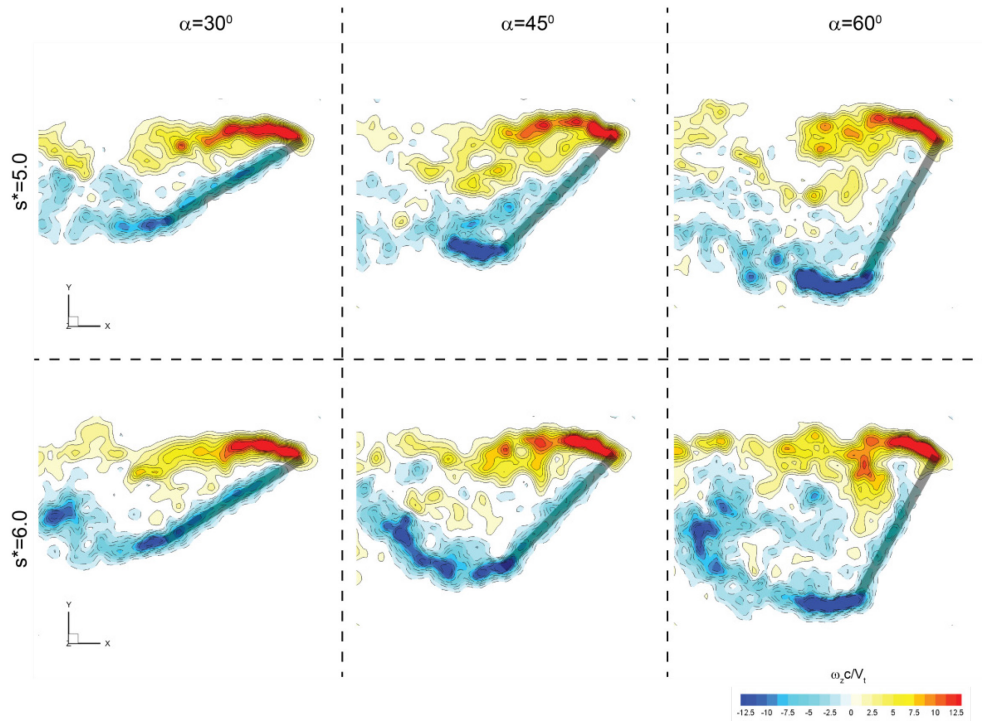
Figure 4-39: Continuation of Figure 4-37 to Later Time, Showing Essential Constancy of Flowfield Evolution Through Six Chords of Travel; Contours of Non-Dimensional Out-Of-Plane Vorticity ($\omega_z c/V_t$) in the Reference Plane.

History of lift coefficient and lift to drag ratio for fixed incidence angles of 15, 30, 45, 60 and 75 degrees is given in Figure 4-40. Peak lift to drag ratio is for the lowest incidence angle, as stands to reason given the plate-normal direction of the total aerodynamic force. This is confirmed by LD ~ 1 for the 45-degree canonical case. For all incidences there is a non-circulatory spike at motion onset, and a smoother spike towards conclusion of acceleration, followed by a gentle rise in lift to about s/c ~ 4. Thereafter aero forces settle to a more or less permanent value indicative of a stable LEV for all incidences. There is no special value of incidence angle associable with stall; all incidence angles yield more or less similar force histories and similar flowfields.
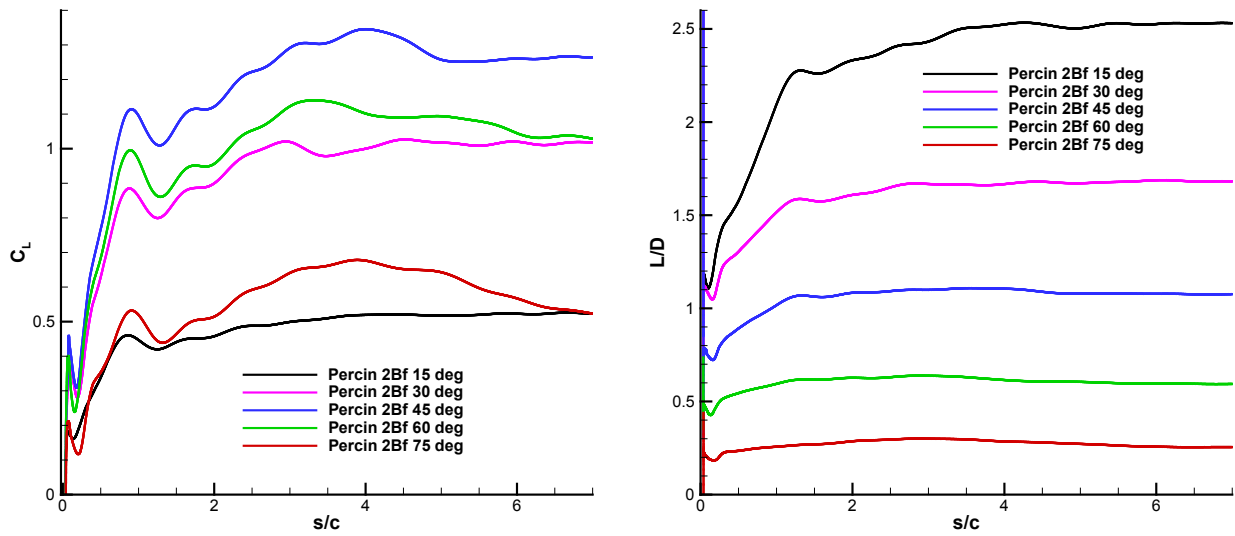
Figure 4-40: Survey of Lift Coefficient (Left) and Lift-to-Drag-Ratio (Right) Histories for "Fast" Rotational Surge, with Acceleration Occurring Over One Chord at the Reference-Plane, and Fixed Incidence Angles of 15, 30, 45, 60 and 75 Degrees. Data from TU Delft Group.

Chapter 5 – CONCLUSIONS

5.1 GENERAL OBSERVATIONS

1) Whether rotational or translational, the pitching cases produce a much larger lift than the fast surging cases. This is the pitch-rate effect. After the pitching motion has concluded, there is a large and fast drop in lift, followed by slow relaxation to the "steady-state" (rotation) or bluff-body response (translation). The two fast pitching cases are very similar in lift history, as are the two fast surging cases.

2) Depending on choice of normalization, one may find the long-term value of lift for the rotational motion to be larger than for the translational motion, or smaller – but it does appear that for the rotational motion the lift asymptotes to a constant value, presumably because of a spatially and temporally more organized flow (by some reckonings a more stable LEV, especially near the wing root) on the plate's suction side, that differs from the bluff-body solution, which Karman-sheds or just has a dead-water region.

3) For fast motions, the peak lift occurs at approximately the point where acceleration concludes. For the slow cases, lift peaks at some earlier time, before the surging motion or the pitching motion is complete, in a stall-like process where the LEV grows, reaches saturation and sheds, all while acceleration of the plate proceeds. The shedding effect is mediated by rotation. One supposes that the slower motions are governed by a vortex formation-time phenomenon, presumably captured in vortex dipole ideas, while for the faster motions, LEVs are still growing and accumulating vorticity at motion's end.

4) For accelerations faster than some threshold, lift history becomes acceleration-independent after acceleration has ceased: if a wing is surging over say $0.25\,c$ instead of $1\,c$, after $1\,c$, the two lift histories coincide – but for slower accelerations, post-acceleration lift history remains influenced by what happened while acceleration was non-zero, because of ensuing vortex development.

5) Secondary peaks in lift, several convective times after acceleration is over, are observed in some cases. These are presumably due to formation of new LEVs, and appear to depend on plate aspect ratio (and installation-effects in experiments).

6) For surging motions, the lift coefficient during acceleration is uncannily proportional to the instantaneous speed of the plate. For quasi-steady response, lift would be proportional to the dynamic pressure (since place incidence is constant), so that the lift coefficient would be quadratic in time.

7) For all motions (fast or slow, pitch or surge, rotational or translational) it takes many convective times (15 or more for translation, perhaps 5 for rotation) to reach the steady-state lift value.

8) For translational fast pitch and translational fast surge, the LEV initially convects away from the LE at approximately one third to half of the reference free-stream speed, while the TEV convects at close to the full free-stream speed. This gives a vortex-force resembling $\rho U\Gamma$. Exact speeds DO vary from case to case, and accuracy is important if we're going to properly capture the total lift force.

9) Vortices are more coherent with increasing reduced-frequency. Individual vortices are harder to identify for the $6\,c$ cases. The flow is also more 3D for slower cases. 3D effects take time to develop – but even massively 3D cases evince possibility of description by 2D reduced-order model in a strip-theory sense. In any case, pitch is kinematically dominated (apparent-mass and Magnus effect), while surge is more vortex-dominated (time rate of change of LEV-TEV dipole impulse).

10) Lift history is a very weak function of Reynolds number, except for possibly at very low Reynolds number (< 100) where LEV formation itself does not occur.

11) A low-order force model developed from the observations of this Task Group has been found capable of making reasonably predictions of force histories and magnitudes (albeit with sometime considerable over-prediction). More significantly it has allowed us to attribute physical mechanisms to the various force contributions, which can inform future research and vehicle development.

5.2 RESUME OF TASK GROUP'S ACCOMPLISHMENTS, AND REMAINING QUESTIONS

We believe that the following can credibly be listed as accomplishments over the past 3 – 4 years:

1) Obtained some quite impressive agreement across many different experiments (and some computations), across our 8 cases (especially translational cases).

2) A promising reduced-order model, not for flapping-wing aircraft design, but for making sense of basic force-trends vs. kinematics morphology.

3) Parameter studies give indication of what force-contributions matter where.

4) Basic understanding of flow features vs. lift-coefficient trends.

However, numerous subjects have been left incomplete, or require an improved conceptual approach. Thus we offer, to motivate further work:

1) No detailed 3D LES computations were compared to detailed 3D PIV.

2) Pitching-moment data has been unreliable, and was not much discussed.

3) Reduced-order models have not yet been extended to parameter studies.

4) Rotational-case role of LEV breakdown: juxtaposition with force-model?

5) Rossby number and passage of rotational case towards translational remains only notionally delineated.

6) Formation-number ideas and demarcation between "fast" and "slow" motions, in terms of when post-acceleration flow no longer "remembers" acceleration history.

7) Why do our reduced-order models "work" with final circulation fitted to $2\pi\alpha$? Just because the vortex fits the growth of circulation, does not mean that the lift has to, because the vortex is not attached to the wing!

Chapter 6 – REFERENCES

[1]   Lentink, D. and Dickinson, M., "Biofluiddynamic Scaling of Flapping, Spinning and Translating: Fins and Wings". *Journal of Experimental Biology*, Vol. 212, pp. 2691-2704, 2009.

[2]   NATO Research and Technology Organization. (2010). "Unsteady Aerodynamics for Micro Air Vehicles". Technical Report RTO-TR-AVT-149. Neuilly-sur-Seine, France: RTO. Available from: http://www.cso.nato.int.

[3]   Bisplinghoff, R.L., Ashley, H. and Halfman, H., *Aeroelasticity*. Dover Science, 1996.

[4]   McGowan, G., Granlund, K., Gopalarathnam, A., Edwards, J. and Ol, M., "Lift cancellation of Pitch-Plunge Airfoil Motions at Low Reynolds Numbers". *AIAA Journal* 49(7) 1511-1541, 2011.

[5]   Brunton, S.L., Rowley, C.W. and Williams, D.R., "Reduced-order unsteady aerodynamic models at low Reynolds numbers". *Journal of Fluid Mechanics*, Vol. 724, pp. 203-233, 2013.

[6]   Shyy, W., Aono, H., Kang, C.-K. and Liu, H., "An Introduction to Flapping Wing Aerodynamics", Cambridge Aerospace Series, 2013.

[7]   Eldredge, J., Wang, C. and Ol, M.V., "A Computational Study of a Canonical Pitch-Up, Pitch-Down Wing Maneuver". AIAA-2009-3687.

[8]   Noca, F., Shiels, D. and Jeon, D., "A Comparison of Methods for Evaluating Time-Dependent Fluid Dynamic Forces on Bodies, Using only Velocity Fields and Their Derivatives". *JFS*, Vol. 13, Issue 5, pp. 551-578, July 1999.

[9]   Graftieaux, L., Michard, M. and Grosjean, N., "Combining PIV, POD and vortex identification algorithms for the study of unsteady turbulent swirling flows". *Meas. Sci. Technol.*, Vol. 12, No. 9, August 2001.

[10]   Lamb, H., (1932). *Hydrodynamics*. Cambridge University Press, 6th edn. 135.

[11]   Pitt Ford, C.W. and Babinsky, H., "Lift and the leading edge vortex". *Journal of Fluid Mechanics*, Vol. 720, pp. 280-313, April 2013.

[12]   Leishman, J.G., "Principles of Helicopter Aerodynamics". Cambridge University Press, 2006.

[13]   Schlueter, K.L., Jones, A.R., Granlund, K.O. and Ol, M.V., "Effect of Root Cutout on Force Coefficients of Rotating Wings". *AIAA Journal*, Vol. 52, pp. 1322-1325, 2014.

[14]   Visbal, M.R., "Three-Dimensional Flow Structure on a Heaving Low-Aspect-Ratio Wing". AIAA 2011-0219.

[15]   Bross, M. and Rockwell, D., "Flow Structure on a simultaneously pitching and rotating wing". *Journal of Fluid Mechanics*, 2014.

[16]   Wolfinger, M. and Rockwell, D., 2014. "Flow structure on a rotating wing: effect of radius of gyration". *Journal of Fluid Mechanics*, Volume 755, pp. 83-110.

[17] Visbal, M., Yilmaz, T.O. and Rockwell, D., 2013. "Three-dimensional vortex formation on a heaving low aspect ratio wing: computations and experiments". *Journal of Fluids and Structures*, Vol. 38, pp. 58-76.

[18] Yilmaz, T.O. and Rockwell, D., 2012. "Flow structure on finite-span wings due to pitch-up motion". *Journal of Fluid Mechanics*, Vol. 691, pp. 518-545.

[19] Ozen, C.A. and Rockwell, D., 2012. "Three-dimensional vortex structure on a rotating wing". *Journal of Fluid Mechanics*, Vol. 707, pp. 541-550.

[20] Ozen, C.A. and Rockwell, D., 2011. "Flow Structure on a Rotating Plate". *Experiments in Fluids*, Volume 52, Number 1, pp. 207-223.

[21] Ol, M.V., Parker, G., Abate, G. and Evers, J., "Flight Controls and Performance Challenges for MAVs in Complex Environments". AIAA 2008-6508.

[22] Raffel, M., Willert, C.E., Wereley, S.T. and Kompenhans, J., "*Particle Image Velocimetry: A Practical Guide*". Springer, 2007.

[23] http://www.ati-ia.com/products/ft/sensors.aspx., accessed 30 September 2014.

[24] Granlund, K., Ol, M.V. and Bernal, L., "Unsteady Pitching Flat Plates". *Journal of Fluid Mechanics*, Vol. 733 R5, 2013.

[25] Coleman, H.W. and Steele, W.G., *Experimentation and Uncertainty Analysis for Engineers*, 2nd Edition, John Wiley & Sons, Inc., New York, NY, USA, 1999, p. 23.

[26] ANSYS® Fluent, Release 15.0, Theory Guide, Ansys Inc., 30 September 2014.

[27] Shih, H., Liou, W.W., Shabbir, A., Yang, Z. and Zhu, J., "A New k-ε Eddy Viscosity Model for High Reynolds Number Turbulent Flows-Model Development and Validation". NASA Technical Memorandum 106721, ICOMP-94-21, CMOTT-94-6, 1994.

[28] Jones, A., "Unsteady Low Reynolds Number Aerodynamics of a Waving Wing"*,* Ph.D. thesis, University of Cambridge, 2010.

[29] Clayton, B.R. and Massey, B.S., "Flow Visualisation in Water: a Review of Techniques". *J. Sci. Instrum,* Vol. 44, 1967.

[30] Schanz, D., Gesemann, S., Schröder, A., Wieneke, B. and Novara, M., "Non-uniform optical transfer functions in particle imaging: calibration and application to tomographic reconstruction". *Measurement Science and Technology*, Vol. 24, pp. 1-16, 2013.

[31] Atkinson, C. and Soria, J., "An efficient simultaneous reconstruction technique for tomographic particle image Velocimetry". *Experiments in Fluids*, Vol. 47, 2009, pp. 563-578.

[32] Taira, K. and Colonius, T., "The immersed boundary method: a projection approach". *Journal of Computational Physics*, 225, 2118-2137, 2007.

[33] Taira, K. and Colonius, T., "Three-dimensional flows around low-aspect-ratio flat-plate wings at low Reynolds numbers". *Journal of Fluid Mechanics*, 623, 187-207, 2009.

[34] Jantzen, R.T., Taira, K., Granlund, K.O. and Ol, M.V., "Vortex dynamics around pitching plates". *Physics of Fluids*, 26, 053606, 2014.

[35] de Baar, J.H.S., Percin, M., Dwight, R.P., van Oudheusden, B.W. and Bijl, H.G., "Kriging regression of PIV data using a local error estimate". *Experiments in Fluids*, Vol. 55, Issue 1, January 2014.

[36] Cottet, G.H. and Koumoutsakos, P.D., "Vortex Methods: Theory and Practice", Cambridge University Press, 2008.

[37] Kudela, H. and Kozlowski, T., "Vortex in cell method for exterior problem". *J. Theor. Appl.Mech.*, Vol. 47, No. 4, 2009.

[38] Kozłowski, T. and Kudela, H., "Transitions in the vortex wake behind the plunging profile". *Fluid Dyn. Res.* 46 (2014) 061406.

[39] Carr, Z.R., Chen, C. and Ringuette, M.J., "Finite-Span Rotating Wings: Three-Dimensional Vortex Formation and Variations with Aspect Ratio". *Exp. Fluids*, Vol. 54:1444, 2013.

[40] Carr, Z.R. and Ringuette, M.J., "Flow Structure of Low-Aspect-Ratio Rotating Wings from Dye Visualization". *AIAA Journal*, Vol. 52, No. 5, pp. 1081-1086, 2014.

[41] Yu, H.-T., "Unsteady Aerodynamics of Pitching Flat Plate Wings". PhD Thesis, University of Michigan, May 2014.

[42] Yu, H.-T., Bernal, L.P. and Morrison, C., "Experimental Investigation of Pitch Ramp-Hold-Return Motion of Flat Plates at Low Reynolds Number". AIAA 2012-0051.

[43] Yu, H.-T. and Bernal, L.P., "Effect of Pivot Point on Aerodynamic Force and Vortical Structure of Pitching Flat Plate Wings". AIAA 2013-0792.

[44] Manar, F. and Jones, A.R., "The Effect of Tip Clearance on Low Reynolds Number Rotating Wings". AIAA 2014-1452.

[45] Harbig, R.R., Sheridan, J. and Thompson, M.C., "Reynolds number and aspect ratio effects on the leading-edge vortex for rotating insect wing planforms". *Journal of Fluid Mechanics*, 717, pp. 166-192, 2013.

[46] Jardin, T., Farcy, A. and David, L., "Three-dimensional effects in hovering flapping flight". *Journal of Fluid Mechanics*, Vol. 702, pp. 102-125, 2012.

[47] Delery, J., "Aspects of Vortex Breakdown". *Progress in Aerospace Sci*ences, Vol. 30, pp. 1-59, 1994.

[48] Lu, Y. and Shen, G.X., "Three-dimensional flow structures and evolution of the leading-edge vortices on a flapping wing". *Journal of Experimental Biology*, Vol. 211, pp. 1221-1230, April 2008.

[49] Shields, M. and Mohseni, K., "Roll Stall for Low-Aspect-Ratio Wings". *Journal of Aircraft*, Vol. 50, No. 4, pp. 1060-1069, July 2013.

[50] Minier, C.S. and Dalton, N.N., "*Physical Properties of Glycerin and its Solutions*". American Chemical Society Monograph 117, Reinhold Publishing Corp., 1953.

[51] Ringuette, M.J., Milano, M. and Gharib, M., "Role of the Tip Vortex in the Force Generation of Low-Aspect-Ratio Normal Flat Plates". *JFM*, Vol. 581, 2007, pp. 453-468.

[52] Kriegseis, J., Kinzel, M. and Rival, D., 2013. "On the Persistence of Memory: Do Initial Conditions Impact Vortex Formation?" *Journal of Fluid Mechanics*, Vol. 736, pp. 91-106.

[53] Wagner, H., "Über die Entstehung des dynamischen Auftriebes von Tragflügeln". *Zeitschrift für angewandte Mathematik und Mechanik* 5(1925) pp. 17-35.

[54] Mancini, P., Jones, A.R., Ol, M.V. and Granlund, K.O., "Parameter Studies on Translating Rigid and Flexible Wings". AIAA 2014-0073.

[55] Garmann, D.J. and Visbal, M.R., "Dynamics of revolving wings for various aspect ratios". *Journal of Fluid Mechanics,* 748, pp. 932-956, 2014.

REPORT DOCUMENTATION PAGE

1. Recipient's Reference	2. Originator's References	3. Further Reference	4. Security Classification of Document
	STO-TR-AVT-202 AC/323(AVT-202)TP/670	ISBN 978-92-837-2030-0	PUBLIC RELEASE

5. Originator	Science and Technology Organization North Atlantic Treaty Organization BP 25, F-92201 Neuilly-sur-Seine Cedex, France

6. Title	Extensions of Fundamental Flow Physics to Practical MAV Aerodynamics

7. Presented at/Sponsored by

AVT-202 Final Report.

8. Author(s)/Editor(s)	9. Date
Multiple	May 2016

10. Author's/Editor's Address	11. Pages
Multiple	124

12. Distribution Statement	There are no restrictions on the distribution of this document. Information about the availability of this and other STO unclassified publications is given on the back cover.

13. Keywords/Descriptors

Apparent mass	Revolving wing
Dynamic stall	Unsteady aerodynamics
Flapping wing	Unsteady aerofoil theory
Leading edge vortex	Vortex shedding
Micro air vehicle	

14. Abstract

In massively unsteady wing-flows, organized flow-separation may increase lift well above steady-state. We explore imposed rotations and rectilinear translations of rigid flat plates in incompressible flow, comparing a linear-ramp angle of attack change with streamwise acceleration (surge). In rotation, the plate revolves about an axis inboard of its inboard tip, notionally representative of a flapping-wing. Experiment, computation and analysis culminated in a two-dimensional lumped-vortex model for physics-based accounting of lift history. Rotation was found to stabilize the leading edge vortex, at least for inboard spanwise locations; the vortex sheds after saturation for the translational case. However, no advantage in peak lift or lift to drag ratio was found in rotation during the manoeuvre itself. Pitching causes a large force transient, both for rotation and translation, relative to surging; this is due to pitch-rate effects, predicted by unsteady aerofoil theory, which also accurately handles apparent-mass effects. For translation, > 10 convective times are needed for the post-manoeuvre lift transient to relax; the rotational case reaches a steady lift value in ~ 5 convective times, and this steady value is higher than for translation. Thus rotation offers a steady-state advantage in lift, but not a transient one, owing to leading-edge vortex behaviour.

CENTRES DE DIFFUSION NATIONAUX

ALLEMAGNE
Streitkräfteamt / Abteilung III
Fachinformationszentrum der Bundeswehr (FIZBw)
Gorch-Fock-Straße 7, D-53229 Bonn

BELGIQUE
Royal High Institute for Defence – KHID/IRSD/RHID
Management of Scientific & Technological Research
for Defence, National STO Coordinator
Royal Military Academy – Campus Renaissance
Renaissancelaan 30, 1000 Bruxelles

BULGARIE
Ministry of Defence
Defence Institute "Prof. Tsvetan Lazarov"
"Tsvetan Lazarov" bul no.2
1592 Sofia

CANADA
DGSlST
Recherche et développement pour la défense Canada
101 Colonel By Drive, 6 CBS
Ottawa, Ontario K1A 0K2

DANEMARK
Danish Acquisition and Logistics Organization
(DALO)
Lautrupbjerg 1-5
2750 Ballerup

ESPAGNE
Área de Cooperación Internacional en I+D
SDGPLATIN (DGAM)
C/ Arturo Soria 289
28033 Madrid

ESTONIE
Estonian National Defence College
Centre for Applied Research
Riia str 12
Tartu 51013

ETATS-UNIS
Defense Technical Information Center
8725 John J. Kingman Road
Fort Belvoir, VA 22060-6218

FRANCE
O.N.E.R.A. (ISP)
29, Avenue de la Division Leclerc
BP 72
92322 Châtillon Cedex

GRECE (Correspondant)
Defence Industry & Research General
Directorate, Research Directorate
Fakinos Base Camp, S.T.G. 1020
Holargos, Athens

HONGRIE
Hungarian Ministry of Defence
Development and Logistics Agency
P.O.B. 25
H-1885 Budapest

ITALIE
Centro Gestione Conoscenza
Secretariat General of Defence
National Armaments Directorate
Via XX Settembre 123/A
00187 Roma

LUXEMBOURG
Voir Belgique

NORVEGE
Norwegian Defence Research
Establishment
Attn: Biblioteket
P.O. Box 25
NO-2007 Kjeller

PAYS-BAS
Royal Netherlands Military
Academy Library
P.O. Box 90.002
4800 PA Breda

POLOGNE
Centralna Biblioteka Wojskowa
ul. Ostrobramska 109
04-041 Warszawa

PORTUGAL
Estado Maior da Força Aérea
SDFA – Centro de Documentação
Alfragide
P-2720 Amadora

REPUBLIQUE TCHEQUE
Vojenský technický ústav s.p.
CZ Distribution Information Centre
Mladoboleslavská 944
PO Box 18
197 06 Praha 9

ROUMANIE
Romanian National Distribution
Centre
Armaments Department
9-11, Drumul Taberei Street
Sector 6
061353 Bucharest

ROYAUME-UNI
Dstl Records Centre
Rm G02, ISAT F, Building 5
Dstl Porton Down
Salisbury SP4 0JQ

SLOVAQUIE
Akadémia ozbrojených síl gen.
M.R. Štefánika, Distribučné a
informačné stredisko STO
Demänová 393
031 06 Liptovský Mikuláš 6

SLOVENIE
Ministry of Defence
Central Registry for EU & NATO
Vojkova 55
1000 Ljubljana

TURQUIE
Milli Savunma Bakanlığı (MSB)
ARGE ve Teknoloji Dairesi
Başkanlığı
06650 Bakanliklar – Ankara

AGENCES DE VENTE

**The British Library Document
Supply Centre**
Boston Spa, Wetherby
West Yorkshire LS23 7BQ
ROYAUME-UNI

**Canada Institute for Scientific and
Technical Information (CISTI)**
National Research Council Acquisitions
Montreal Road, Building M-55
Ottawa, Ontario K1A 0S2
CANADA

NORTH ATLANTIC TREATY ORGANIZATION

**NATO
OTAN**

BP 25
F-92201 NEUILLY-SUR-SEINE CEDEX • FRANCE
Télécopie 0(1)55.61.22.99 • E-mail mailbox@cso.nato.int

SCIENCE AND TECHNOLOGY ORGANIZATION

S&T
organization

**DISTRIBUTION OF UNCLASSIFIED
STO PUBLICATIONS**

AGARD, RTO & STO publications are sometimes available from the National Distribution Centres listed below. If you wish to receive all STO reports, or just those relating to one or more specific STO Panels, they may be willing to include you (or your Organisation) in their distribution.
STO, RTO and AGARD reports may also be purchased from the Sales Agencies listed below.

Requests for STO, RTO or AGARD documents should include the word 'STO', 'RTO' or 'AGARD', as appropriate, followed by the serial number. Collateral information such as title and publication date is desirable.

If you wish to receive electronic notification of STO reports as they are published, please visit our website (http://www.sto.nato.int/) from where you can register for this service.

NATIONAL DISTRIBUTION CENTRES

BELGIUM
Royal High Institute for Defence – KHID/IRSD/
RHID
Management of Scientific & Technological
Research for Defence, National STO Coordinator
Royal Military Academy – Campus Renaissance
Renaissancelaan 30
1000 Brussels

BULGARIA
Ministry of Defence
Defence Institute "Prof. Tsvetan Lazarov"
"Tsvetan Lazarov" bul no.2
1592 Sofia

CANADA
DSTKIM
Defence Research and Development Canada
101 Colonel By Drive, 6 CBS
Ottawa, Ontario K1A 0K2

CZECH REPUBLIC
Vojenský technický ústav s.p.
CZ Distribution Information Centre
Mladoboleslavská 944
PO Box 18
197 06 Praha 9

DENMARK
Danish Acquisition and Logistics Organization
(DALO)
Lautrupbjerg 1-5
2750 Ballerup

ESTONIA
Estonian National Defence College
Centre for Applied Research
Riia str 12
Tartu 51013

FRANCE
O.N.E.R.A. (ISP)
29, Avenue de la Division Leclerc – BP 72
92322 Châtillon Cedex

GERMANY
Streitkräfteamt / Abteilung III
Fachinformationszentrum der
Bundeswehr (FIZBw)
Gorch-Fock-Straße 7
D-53229 Bonn

GREECE (Point of Contact)
Defence Industry & Research General
Directorate, Research Directorate
Fakinos Base Camp, S.T.G. 1020
Holargos, Athens

HUNGARY
Hungarian Ministry of Defence
Development and Logistics Agency
P.O.B. 25
H-1885 Budapest

ITALY
Centro Gestione Conoscenza
Secretariat General of Defence
National Armaments Directorate
Via XX Settembre 123/A
00187 Roma

LUXEMBOURG
See Belgium

NETHERLANDS
Royal Netherlands Military
Academy Library
P.O. Box 90.002
4800 PA Breda

NORWAY
Norwegian Defence Research
Establishment, Attn: Biblioteket
P.O. Box 25
NO-2007 Kjeller

POLAND
Centralna Biblioteka Wojskowa
ul. Ostrobramska 109
04-041 Warszawa

PORTUGAL
Estado Maior da Força Aérea
SDFA – Centro de Documentação
Alfragide
P-2720 Amadora

ROMANIA
Romanian National Distribution Centre
Armaments Department
9-11, Drumul Taberei Street
Sector 6
061353 Bucharest

SLOVAKIA
Akadémia ozbrojených síl gen
M.R. Štefánika, Distribučné a
informačné stredisko STO
Demänová 393
031 06 Liptovský Mikuláš 6

SLOVENIA
Ministry of Defence
Central Registry for EU & NATO
Vojkova 55
1000 Ljubljana

SPAIN
Área de Cooperación Internacional en I+D
SDGPLATIN (DGAM)
C/ Arturo Soria 289
28033 Madrid

TURKEY
Milli Savunma Bakanlığı (MSB)
ARGE ve Teknoloji Dairesi Başkanlığı
06650 Bakanliklar – Ankara

UNITED KINGDOM
Dstl Records Centre
Rm G02, ISAT F, Building 5
Dstl Porton Down, Salisbury SP4 0JQ

UNITED STATES
Defense Technical Information Center
8725 John J. Kingman Road
Fort Belvoir, VA 22060-6218

SALES AGENCIES

**The British Library Document
Supply Centre**
Boston Spa, Wetherby
West Yorkshire LS23 7BQ
UNITED KINGDOM

**Canada Institute for Scientific and
Technical Information (CISTI)**
National Research Council Acquisitions
Montreal Road, Building M-55
Ottawa, Ontario K1A 0S2
CANADA

Requests for STO, RTO or AGARD documents should include the word 'STO', 'RTO' or 'AGARD', as appropriate, followed by the serial number (for example AGARD-AG-315). Collateral information such as title and publication date is desirable. Full bibliographical references and abstracts of STO, RTO and AGARD publications are given in "NTIS Publications Database" (http://www.ntis.gov).

ISBN 978-92-837-2030-0